Surface and Buildup Dose Effects in a Linac-MR

by

Andrei Dorin Ghila

A thesis submitted in partial fulfillment of the requirements for the degree of

Doctor of Philosophy

in
Medical Physics

Department of Oncology
University of Alberta

Abstract

Magnetic resonance imaging (MRI) can visualize solid tumours in real time and its integration with a linear accelerator offers the possibility to track tumours during irradiation. However, irradiating a patient inside a linac-MR poses several challenges. MRI uses radiofrequency (RF) coils to acquire images, and with existing RF coil designs, the patient will have to be irradiated through the RF coil. Also a linac-MR in which the main magnetic field is parallel to the radiation beam central axis is expected to cause surface and buildup dose modifications. The purpose of the current work is to experimentally investigate and quantify the surface and buildup dose modifications caused by irradiating through typical RF coil materials and by irradiating in the presence of a strong parallel magnetic field. The surface and buildup dose measurements in a parallel magnetic field are used to verify the ability of the EGSnrc Monte Carlo system to accurately calculate magnetic field dose effects.

An imitation RF coil (layers of polycarbonate, copper tape, and Teflon) was placed at various distances from the surface of a polystyrene phantom and irradiated using a 6 MV photon beam. The depth dose in polystyrene was measured in three cases: no magnetic field, a 0.22 T magnetic field perpendicular to the radiation beam central axis, and a 0.21 T magnetic field parallel to the radiation beam. With the imitation RF coil in direct contact with the surface of the polystyrene phantom the surface and buildup dose increased considerably irrespective of a magnetic field's presence or orientation. With no magnetic field, moving the coil away from the surface of the phantom gradually decreased the surface dose. When the measurements were repeated in a transverse magnetic field, the surface dose decreased even faster with increasing coil to phantom separation. In a parallel magnetic field, increasing the separation between the

coil and the phantom had a minimal effect on decreasing the surface and buildup dose. The influence of other RF coil materials (RF coil casing, RF coil plastic sheet, RF coil foam padding, thin copper sheet, thin copper pipe) on the surface dose was also investigated, and displayed the same trends. Thus, in order to use surface coils in a linac-MR, the current coil design has to be modified.

An electromagnet (two coils) provided a magnetic field parallel to the radiation beam central axis of a clinical linac, and offered a central bore for phantom placement. A polystyrene, and subsequently a Gammex lung phantom, were placed inside the bore at two locations: top of the phantom coinciding with the top of the bore and top of the phantom coinciding with the centre of the bore. COMSOL Multi-physics created a 3D magnetic field map that was validated against magnetic field measurements taken along three orthogonal axes. A benchmarked (against commissioning measurements) BEAMnrc model of the clinical linac was used to simulate the phase space of particle fluence. A parallel plate ion chamber measured the doses in the phantoms. The dimensions of the ion chambers' air cavity and entrance window had to be included in the simulations. The 3D magnetic field map was implemented in DOSXYZnrc and the charge particle deflection per step, due to the magnetic field, was restricted compared to default values. With these modifications, EGSnrc was able to accurately calculate the surface and buildup dose increases caused by the parallel magnetic field at both locations within the bore, for polystyrene and lung.

Preface

This thesis is the original work of Andrei Ghila. A version of Chapter 3 detailing the effects of RF coil materials on surface and buildup dose has previously been published as: A. Ghila, B.G. Fallone, S. Rathee "Influence of Standard RF Coil Materials on Surface and Buildup Dose from a 6MV Photon Beam in Magnetic Field", Med. Phys. 43(11) 5808-5816, (2016). Also, a version of Chapter 4 investigating the accuracy of EGSnrc Monte Carlo in calculating surface and buildup dose effects in polystyrene with a parallel magnetic field has been published as: Andrei Ghila, Stephen Steciw, B.Gino Fallone, Satyapal Rathee "Experimental verification of EGSnrc Monte Carlo calculated depth doses within a realistic parallel magnetic field in a polystyrene phantom", Med. Phys. 44(9) 4804-4815, (2017). A version of Chapter 5 is to be published as: Andrei Ghila, B Gino Fallone, Satyapal Rathee "Technical Note: Experimental verification of EGSnrc calculated depth dose within a parallel magnetic field in a lung phantom", Med. Phys. (2018).

For all the publications, I was responsible for collecting, producing, and analysing the data, as well as for the composition and writing of the manuscript. Dr. S. Steciw helped with the calculation of the 3D magnetic field map needed for the Monte Carlo simulations from Chapter 4 and Chapter 5. Dr. S. Rathee, and Dr. B. G. Fallone were supervisory authors, involved with the formulation of the research project, and with the review and editing of the manuscripts.

Acknowledgements

First and foremost I would like to thank my parents for putting up with me throughout my never-ending graduate career. Without your support, encouragement, love and, let's not forget, food and shelter, I would definitely not be where I am today. So thank you from the bottom of my heart, for allowing me to do what I needed to do, and for not kicking me out of the house... yet.

Next I would like to thank my supervisor, Dr. Satyapal Rathee. Thank you for being my supervisor, for talking me through the sticky points in my research, and for always reminding me to use scientific language. This project would not have been possible without your input, support (financial and otherwise), and guidance. Thank you for our discussions, and for sticking by me for all these years.

Many thanks to my co-supervisor Dr. Gino Fallone. Thank you for being the driving force behind our department wide linac-MR project, and for allowing me to be a part of it. Thank you for keeping us all on track with our weekly project meetings while also giving us a better understanding of where our individual projects fall in.

To the other member of my supervisory committee, Dr. Don Robinson I would like to say thank you for designing the electromagnet stand for me, and for reminding me to always act professionally.

Next I would like to thank my peers, who have been many over the years. My graduate school experience would not have been the same without each and every one of you. From long discussions on various controversial topics in the back offices, to gym trips during lunch, to

teaching each other various things about research, and the world. I have grown tremendously as a person since starting this program, and I can attribute a lot of that to all the interactions I have had with you all. So thank you for being my friends, thank you for being good people, and thank you for enriching my life. I know I will not name all of you, but some of you did stick out over the years, so here it goes. Thank you to Jean David (JD) for annoying me enough (by getting really buff really fast) to keep in shape all these years with our 8.5 years of gym together. You are an excellent spotter and motivator, my friend. Thank you Eugene for all our discussions over the years. You seemed to always find THE controversial topic of the day to bring up, and then we would all watch our late afternoon productivity go down in flames, as we were trying to set things right in the universe once again by discussing it to death. Thank you Dan Michael, for your excellent advice when it comes to anything computer related, and for generally being a good friend. I have learned many things from our conversations on the train, bus, car rides on our way home, most of them geeky, but all of them cool. Thank you Danielle for setting a shining example of quiet conscientiousness for me. It may have taken us a few years before we got you to join in our conversations, but I am very glad you finally did, and managed to elevate their level somewhat. Thank you Amr, for setting an example for me. Yes, I was about to make a joke about being in this department forever and ever, but the example you set was of perseverance. You stuck through it all, you endured, and you came out victorious on the other end. I know I should have listened to your sage advice more often, but I had some growing up to do before I saw just how wise you were. Thank you Jay for all your jaded marital life advices. Thank you Mike for all the scientific, and gym related conversations. Thank you Devin for demonstrating to me that first impressions can be very wrong. Thank you Hali for showing us all how a PhD should be done in this department. Thank you Radim, for joining me at the gym, just as JD was

leaving, and for sticking with it all this time. You can argue with the best of them, and you may be one of the few people I can disagree with in a very civilized conversation. Thank you for giving me an outside perspective when I could only see my own little dark corner of the world, and for generally being a smart, fun to hang out with kind of guy. Chin up, my Eastern European brother, things are bound to look up eventually. Thank you Teresa for making the last few months of my PhD unexpectedly fun. I`ve never met someone so similar to myself in so many ways, yet so different (definitely more optimistic, and far less jaded). The only girl I know that can be one of the guys, and make the guys feel like her best girlfriends all at the same time. You are a special human being, and I am thankful that I got a chance to know you. Thank you Brennen for all the beers, the fun, and the gaming/computer talks over the years. You may have looked like a quiet one at first, but once I got to know you, you definitely proved to be a fun guy and good friend. Thank you Amir for your help with this project, and for all the laughs. Thank you Joel for the linac commissioning help. Thank you Moti for showing me it is possible to do a PhD and take care of a family at the same time. And to all the others: Katie, Lori, Ben, Mike, Danny, Hongwei, Cameron, Amanda, Ayhan, Shima, Brie, Clara, Bryson, Aaron, Niri, Nick, Preet and all the ones that don`t come to mind right now, I thank you all for all the little things. It`s these little things that when put together make up life.

Last, but certainly not least I would like to thank my high school physics teacher, Mr. Ionica Mircea. Thank you sir, for instilling in me a love of the exact sciences, and especially of physics. The two years that you were my teacher, have set me on the path culminating with this thesis. Thank you for giving me the basic tools I needed to succeed in this field. I may have polished and sharpened them over the years, but they are pretty much the same old tools that I received from you all those years ago.

Table of Contents

List of Figures

List of Acronyms

2D	Two Dimensional
3D	Three Dimensional
3D-CRT	Three Dimensional Conformal Radiation Therapy
4DCT	Four Dimensional Computed Tomography
ART	Adaptive Radiation Therapy
bSSFP	Balanced Steady State Free Precession
CAX	Central Axis
CBCT	Cone Beam Computed Tomography
CCD	Charged Coupled Device
CDF	Cumulative Distribution Function
CPE	Charged Particle Equilibrium
CSDA	Continuous Slowing Down Approximation
CT	Computed Tomography
CTV	Clinical Target Volume
DNA	Deoxyribonucleic Acid
EBRT	External Beam Radiation Therapy
EGS	Electron Gamma Shower
EM	Electro-Magnetic/ Electro-Magnetism
EPID	Electronic Portal Imaging Device
ERE	Electron Return Effect

FEM	Finite Element Method
FWHM	Full Width Half Maximum
GTV	Gross Tumour Volume
ICRU	International Commission on Radiation Units and Measurements
IGRT	Image Guided Radiation Therapy
IMRT	Intensity Modulated Radiation Therapy
kerma	Kinetic Energy Released per unit Mass of Medium
kV	Kilo-Voltage
LED	Light Emitting Diode
MC	Monte Carlo
MLC	Multi Leaf Collimator
MRI	Magnetic Resonance Imaging
MV	Mega-Voltage
MV-CBCT	Mega-Voltage Cone Beam Computed Tomography
MVCT	Mega-Voltage Computed Tomography
NIST	National Institute of Standards and Technology
NRC	National Research Council Canada
NTCP	Normal Tissue Complication Probability
OAR	Organ(s) At Risk
PDD	Percent Depth Dose
PDF	Probability Density Function
PET	Positron Emission Tomography
ppic	Parallel Plate Ion Chamber

PTV	Planning Target Volume
RF	Radio Frequency
SNR	Signal to Noise Ratio
SSD	Source to Surface Distance
TCP	Tumour Control Probability
TCPE	Transient Charged Particle Equilibrium

Chapter 1: Introduction

1.1 What is cancer?

Despite popular belief, cancer is not one single, all encompassing disease. Depending on the classification, a set of roughly 100 to more than 200 types of diseases can be called cancer. Cancer emerges when our own cells start "misbehaving". Each one of our cells contains genes that tell the cell when to grow, how to work, when to divide and when to die. However, sometimes the cellular DNA can undergo a change, or sustain damage. This can lead to mutated genes that no longer function properly. Sometimes, these mutated genes cause the cells to either divide out of control or to not die when they are supposed to. This can eventually lead to the formation of growths, in various parts of the body, called tumours. Most types of cancer result in the formation of solid tumours with the notable exception of leukemias. Solid tumours can grow to such an extent that they start impeding normal organ function, leading to serious health problems, and ultimately, to death[1].

Non-cancerous or benign tumours do not spread to different parts of the body, although they can grow quite large. Benign tumours also tend to not reappear once they have been surgically removed. On the other hand, *cancerous* or *malignant* tumours have the potential to spread, invading nearby tissue. Cancer cells can also enter the blood stream or the lymphatic system and form secondary tumours in different parts of the body called *metastases*. Even after surgical removal of cancerous tumours, the cancer may still reappear, as malignant cells could still exist in various parts of the body, if the cancer has already started to metastasize[1].

1.2 Cancer Prevalence

Cancer is the leading cause of death in Canada followed by cardiovascular diseases, accidents, and chronic lower respiratory diseases[2]. Roughly half of the people in Canada will develop cancer within their lifetime, while about a quarter of Canadians are expected to die of cancer. Half of all new diagnosed cancers appear in lung, breast, colon, and prostate. Lung cancer kills more Canadians than the other three major cancers combined. Over the past 30 years the mortality rate due to cancer has dropped, mainly due to a drop in the mortality caused by lung cancers[3].

Although cancer can affect people of all ages, close to 90% of Canadians who are diagnosed with cancer are over the age of 50, and around 45% of cancer is diagnosed in people over the age of 70. Cancer at a younger age can, however, have a devastating impact as it is a leading cause of disease-related deaths for children younger than 15 in Canada[3], and the second leading cause of death in the United States[4].

1.3 Cancer Treatments

There are three main treatment options for cancer in Canada: surgery, radiation therapy, and chemotherapy. Surgery is used to remove a tumour in part or in full, and it is the most effective treatment when a cancerous tumour is detected early while it is small and localized. Radiation therapy is used to shrink or eradicate tumours using radiation to kill cancerous cells while trying to spare healthy cells. The most common type of radiation therapy is *external beam radiation therapy* (EBRT). In EBRT, radiation beams are directed at deep-seated tumours from various angles. For certain types of cancers *internal radiation therapy,* (*i.e. brachytherapy*) is

recommended. During internal radiation therapy, various radioactive substances are placed inside the body, directly in and around the tumour. Radiation therapy kills fast dividing cells most effectively since the fast growing cancer cells are generally more radiosensitive than the healthy cells. Chemotherapy uses drugs to stop the growth and proliferation of the fast dividing cancer cells. Chemotherapy and most drug therapies are systemic, meaning they can kill or hinder growth of cancer cells wherever they are in the body[1].

Depending on the anatomical site of the cancer, the biological make-up of the cancer cells, the disease-stage, as well as the patients' personal wishes, an oncologist may recommend a patient undergo just one of these three treatment modalities, or a combination of all three. Other, less common, but useful, types of cancer treatments include hormonal therapy, biological therapy, and stem cell transplant usually delivered in combination with one or more of the main types of treatment[1].

In the following sections we shall take a closer look at radiation therapy, more specifically, at EBRT.

1.4 Introduction to Radiation Therapy

Less than two months after Wilhelm Conrad Rontgen discovered x-rays at the end of 1895, this "new kind of rays" were already being used to treat cancer[5]. A few months after Rontgen published his "Preliminary Communication" Henry Becquerel discovers natural radioactivity[6] in 1896, and two years later in 1898 the Curies discover radium[7]. A whole new era in both science and medicine was spearheaded by these three discoveries. As time went on, higher energy radiation (x and γ-rays) started being produced; from the 140 kV x-ray "hot cathode tube" developed by Coolidge, to the cobalt-60 γ-ray teletherapy units developed by

Johns in Saskatoon, and on to the mega-voltage (MV) x-rays from the linear accelerators (linacs) of today. The higher energies allowed for the treatment of deep-seated tumours while sparing the radio-sensitive skin which receives the highest dose[6] at the lower x-ray energies. Skin erythema, desquamation, and necrosis, are still limiting factors for external radiation beam delivery[8], and care must be taken to properly take into account immobilisation devices and couch tops that can increase the skin dose when present in between the patient and the radiation source[9].

Sparing healthy tissues, like the skin, and organs at risk (OAR) from a high radiation dose reduces the normal tissue complication probability (NTCP). At the same time, delivering a higher radiation dose to the tumour increases the tumour control probability (TCP)[10]. All radiation treatments are optimally planned with this premise, thus for a successful radiation treatment, the importance of accurate localization of the tumour and OARs was recognized early on[11]. As such, various imaging technologies were being developed alongside the improved sources of radiation. Computers started being used in the 1960's, initially for universal isodose calculations, then with the advent of computed tomography (CT) and magnetic resonance imaging (MRI) in the 1970's for individual personalized treatment plans[10]. The tremendous increase in computing power over the past couple of decades has facilitated the implementation of increasingly advanced radiation treatment techniques in the clinic. From three dimensional conformal radiation therapy (3D-CRT), to the addition of multileaf collimators (MLCs) to linacs, intensity modulated radiotherapy (IMRT), tomotherapy, adaptive radiation therapy (ART), and many other treatment modalities have been implemented as a consequence. All these treatment techniques have contributed to the radiation dose being delivered more accurately and precisely to the tumour while maximizing healthy tissue sparing[10].

1.5 Image-Guided Radiation Therapy

The accurate and precise delineation of the tumour and the OARs becomes critical with the increasing complexity of the radiation delivery. Recognizing this, the International Commission on Radiation Units and Measurements (ICRU) Report Number 50 has standardized the nomenclature of three regions around the tumour to facilitate radiation treatment planning and delivery.

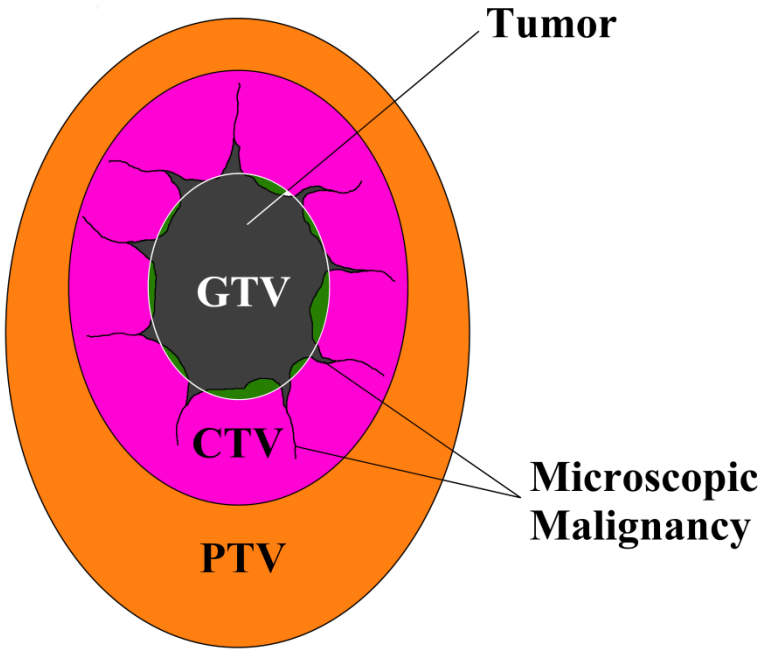

Figure 1.1 Schematic illustration of the ICRU 50 defined volumes: Gross Tumour Volume (GTV), Clinical Target Volume (CTV), and Planning Target Volume (PTV).

The GTV or Gross Tumour Volume is defined as "*the gross palpable or visible/demonstrable extent and location of the malignant growth"*. The Clinical Target Volume or CTV is "*a tissue volume that contains a GTV and/or subclinical microscopic malignant disease, which has to be eliminated*". The CTV is referred to as an *anatomical-clinical concept* that the ICRU recommends should be defined before a treatment modality is chosen. In contrast,

the Planning Target Volume or PTV is defined as a "*geometrical concept [...] taking into consideration the net effect of all the possible geometrical variations and inaccuracies in order to ensure that the prescribed dose is actually absorbed in the CTV*"[12]. The PTV encompasses the CTV and accounts for the organ motion, the day-to-day patient setup errors in fractionated treatments, and the inaccuracies in beam setup. The PTV is the practical volume used to specify the prescription dose. These three volumes are schematically represented in Figure 1.1.

As stated previously, the goal of a radiotherapy treatment is to deliver the highest possible dose to the tumour (namely the PTV), while at the same time delivering the lowest possible dose to the surrounding healthy tissue (maximize TCP while minimizing NTCP). But the PTV, by definition, includes some healthy tissue which can only be reduced by minimizing various geometric sources of uncertainty by using imaging techniques. Image-guided radiation therapy (IGRT) refers to frequent patient imaging to correct for the day-to-day variations in aligning patients' treatment volume to the radiation beam. Consequently the PTV margin around the CTV is smaller which reduces the amount of healthy tissue being irradiated[10,13]. The more prevalent, clinically implemented imaging methods used for IGRT include: ultrasound, radiographic megavoltage (MV) imaging, radiographic kilovoltage (kV) imaging, kilovoltage cone beam computed tomography (CBCT), megavoltage computed tomography (MVCT), as well as optical tracking[13,14]. In the next few sections each one of these imaging methods will be briefly introduced.

1.5.1 Ultrasound

Ultrasound is a three dimensional imaging modality which is most commonly used for guiding the implantation of radioactive sources (brachytherapy) for treating prostate cancer. Ultrasound can also be used for external beam radiotherapy (EBRT) to visualize soft tissue

before treatment, but requires accurate spatial registration of the transducer and the imaging plane. Systems using an articulated arm, infrared cameras, and reflective markers, or optical cameras mounted on the transducer, are commercially available[14]. One of the drawbacks of using ultrasound for EBRT is that the imaging is limited to superficial, pelvic or upper abdominal locations since an acoustic window is necessary. Another drawback is that real time ultrasound during EBRT is not feasible, as an operator is usually required in the room, plus some studies argue that the pressure of the imaging probe can introduce organ displacements[13,15].

1.5.2 Megavoltage (MV) Radiographs

One of the first imaging methods used the MV x-ray treatment beam itself and a 2D radiation detector to acquire a beam's eye view, 2D radiographic projections of the patient. These detectors are customarily known as electronic portal imaging devices (EPIDs). However, the patient's 3D anatomy is collapsed into 2D MV radiographs with relatively poorer tissue contrast compared to kV radiographs. Nevertheless, airways and the bony anatomy can be used to align the patient with the beam. Unfortunately, even when the bony anatomy is aligned, most tumours and healthy tissues can move considerably with respect to the bones. One solution to this is to implant radiopaque markers in or near the treated volume[13,15], which is an invasive procedure. Since, in addition to the poor contrast, MV radiographs will typically increase the patient's dose on average by 4 cGy per image pair[16,17], other methods using linac gantry mounted or room mounted kV x-ray tubes along with an active matrix flat panel imager have been developed[18].

1.5.3 Kilovoltage (kV) Radiographs

Radiographs using kV X-ray tubes yield better contrast images while delivering only a small fraction of the dose of MV radiographs; thus more frequent imaging can be performed. Although for localizing soft tissues there is still a need for implanted fiducial markers, these markers can be substantially smaller than those used for MV imaging. But, even when mounted on the same gantry as the MV radiation source, the kV beam does not image in an exact beam's eye view plane, which may add extra localization errors[15,18.] KV x-ray fluoroscopic imaging has been used to track implanted markers in real time during MV treatment[19], with a linac programmed to only deliver radiation when the marker is located within a predetermined region. This however, is not true real time tumour tracking as it still relies on tracking the implanted fiducial markers as tumour surrogates.

1.5.4 Cone Beam Computed Tomography (CBCT)

Similar to kV radiographic system, the CBCT system consists of a kV x-ray source and flat panel detector mounted on a linac with the same axis of rotation as the MV source, with the kV beam perpendicular to the MV beam[13,14]. Three dimensional tomographic images can be reconstructed from hundreds of 2D projections acquired in one rotation around the patient. The CBCT images offer better soft tissue contrast at radiation doses ranging from 0.5 cGy to 4 cGy. MV-CBCT can also be acquired using the MV source and the linac's EPID. The average dose delivered to the patient during the acquisition of MV-CBCTs can be between 5 to 15 cGy[20]. In a particular MV-CBCT phantom study[21] however, a radiation dose of 65 cGy was needed to obtain images with a similar signal to noise ratio (SNR) to a kV CBCT when imaging the same contrast phantom. Thus, due to the relatively high dose, MV-CBCT is advantageous only for patients with orthopedic metal implants[22] that cause severe artifacts in kV CBCT and diagnostic multi-

detector CT. The general drawbacks of CBCTs are: the C-arm gantry is slow, resulting in motion artifacts in thoracic and abdominal imaging; the cone beam irradiation and 2D detector geometry corrupts the projections with scatter that degrades image contrast compared to multi-detector diagnostic CT. Additionally, CT imaging requires more than half a gantry rotation to form an image and it cannot be used to image in real-time during MV treatment beam ON[18].

1.5.5 Optical Tracking

Optical tracking of markers that either emit or reflect light is being used for real time tracking of moving tumours. The advantages of optical tracking systems are their superior spatial and temporal resolution. A tracked marker can be spatially localized with sub-millimetre accuracy at a rate ≥10 Hz. A charged couple device (CCD) camera images the markers, which can be either infrared LEDs (active markers) or reflecting spheres (passive markers). These markers, when placed on the chest and/or abdomen of the patient, provide signals surrogate to breathing-induced motion of the internal tumours. The treatment beam can then be turned ON during a pre-determined portion of the motion track (called a gating window) that assures the tumour motion remains below a pre-determined threshold. Four dimensional CT (4DCT) of the patient can also be acquired where the optical marker signals allow binning of CT images into separate breathing phases. The disadvantage of optically tracked markers is that the markers can only be placed on the surface of the patient[14]. Thus the underlying assumption is that the body surface movement is an accurate surrogate for tumour and internal organ motion, which is not always the case[14,18,23].

1.5.6 Magnetic Resonance Imaging (MRI)

Magnetic resonance imaging (MRI) is a 3D, non-invasive imaging technique that does not use ionizing radiation and provides high resolution images with exquisite soft tissue contrast. MRI is sensitive to a broad range of tissue properties (proton density, T1, T2 and their combination) to provide soft tissue contrast in anatomical images. Additionally, MRI sequences can provide image signals used to visualize and/or quantify tumour perfusion, vascular permeability, and degree of hypoxia[24,25]. The current clinical standard uses MRI in conjunction with CT and PET (Positron Emission Tomography) for target delineation in radiotherapy treatment planning brain, and head and neck cancers[25]. Although MRI is inherently slower at acquiring images than CT, fast imaging sequences such as balanced Steady State Free Precession (bSSFP) have been used to image a plane in the patient at 4 images per second. Thus, in more recent years, several research groups[26-28] around the world have been independently working on integrating a teletherapy unit with an MRI. Such an integrated unit will use the MRI's real time capabilities and the superior soft tissue contrast to further reduce the PTV by tracking moving tumours and adapting the treatment to daily variations on the fly.

1.6 The Linac-MR project at the Cross Cancer Institute

Two integrated linac-MR units have been designed, developed, and built at the Cross Cancer Institute (Edmonton, AB, Canada) to date. Both of them consist of a bi-planar MRI mechanically coupled to a 6 MV linear accelerator able to rotate on the same gantry and deliver radiation to the patient from any angle[26].

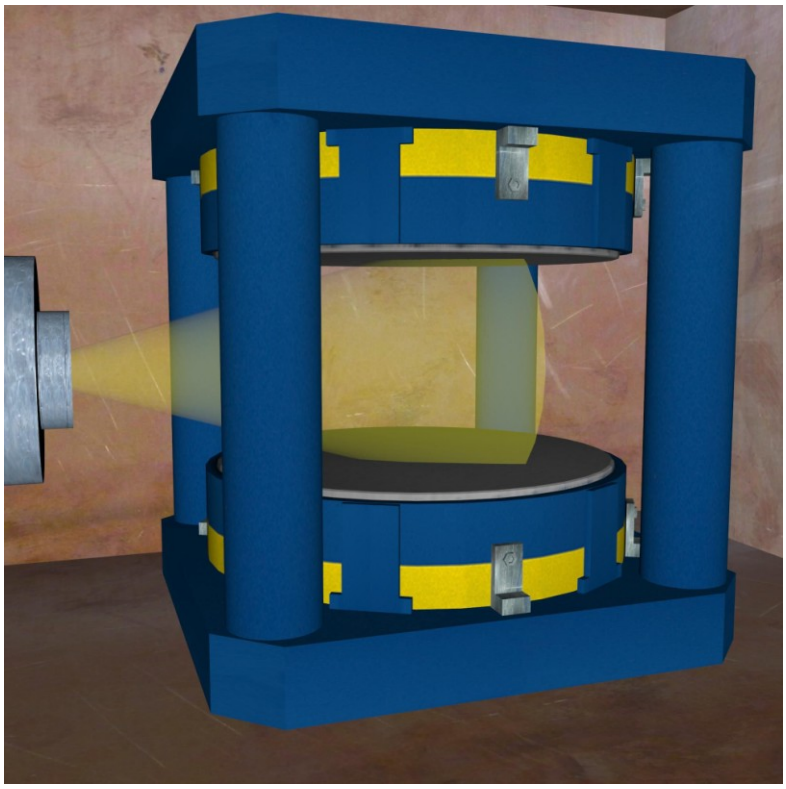

Figure 1.2 Computer rendering of the CCI head scale Prototype I linac-MR. The beam irradiates in between the permanent magnet poles, and is perpendicular to the main magnetic field.

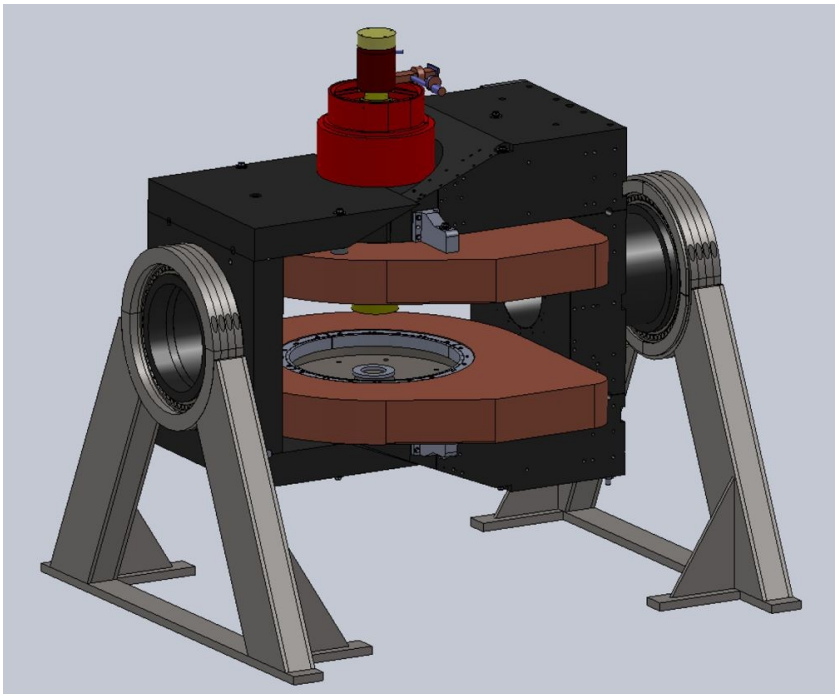

Figure 1.3 Computer rendering of the CCI full scale Prototype II linac-MR. The beam irradiates through an opening in one of the pole plates, and is parallel to the main magnetic field.

Prototype I (Figure 1.2) consists of a head scale bi-planar, 0.22 T, permanent magnet MRI, with the radiation provided by a Varian 600C (Varian Medical Systems, Palo Alto, CA) linac. The linac irradiates through the open space between the MRI's pole plates, reaching the patient unobstructed, and the main magnetic field is perpendicular to the radiation beam central axis. Thus, Prototype I is said to be a perpendicular or transverse configuration linac-MR.

Prototype II, shown in Figure 1.3, is a full scale 0.56 T, bi-planar, superconducting MRI coupled to another Varian linac. For this unit, the linac is irradiating through a port in one of the MRI's pole plates, with the main magnetic field parallel to the radiation beam central axis, making Prototype II a parallel configuration linac-MR.

Over the past decade, our group has investigated and solved many issues which arise from integrating a linac with an MRI, from the mutual interference between the two units[29,30] to reducing or completely removing the effects of the radiation induced currents that arise in the MRI's RF coils[31,32]. Various fast imaging techniques as well as auto-contouring algorithms that are critical for real time tumour tracking have also been investigated and developed in house[33-35].

1.7 Motivation and Thesis Outline

Delivering high, accurate radiation doses to a patient inside an MRI presents several dosimetric challenges. Firstly when irradiating the patient in a linac-MR unit, the off-the-shelf radiofrequency (RF) coils that the MRI uses to acquire images will be in the beam path. Any materials present in the treatment beam will modify the dose delivered to the patient[36] but the actual increase in surface and buildup dose due to typical RF coil materials has not been previously quantified. Secondly the patient is irradiated in the presence of a strong magnetic field. This has been shown to cause dose deposition modifications that appear to be more severe

in a transverse configuration linac-MR[37] compared to the modifications that arise in a parallel configuration system[38].

It was found that irradiating in the presence of a strong transverse magnetic field can greatly increase the dose at tissue/air or tissue/lung interfaces[37]. This dose increase is apparent at the distal side of the patient, as well as at the lateral sides that are in the treatment beam. Irradiated air cavities (like the patient's airways) are also affected[39]. In addition, a transverse magnetic field will also cause decreased buildup distances (by ~5 mm for 1.5 T), and shifted lateral beam profiles in the direction perpendicular to the magnetic field[40]. All these effects generally become more pronounced for stronger transverse magnetic fields[39]. Various solutions have been proposed for solving the increased exit dose problem. Using parallel opposed beams[37], the use of inverse treatment planning for calculating optimized IMRT that accounts for the presence of the transverse magnetic field[41], or simply using bolus[42] have all been shown to reduce this unwanted dose increase.

Irradiating in the presence of a strong parallel magnetic field significantly decreases the interface dose effects apparent in a transverse field[43]. Also, due to the focusing of secondary electrons, the parallel field can increase the PTV dose and sharpen the beam penumbra[43]. However, the parallel magnetic field can also impede the lateral scatter of contaminant electrons that accompany the photon beam causing entrance surface dose increases for parallel field systems[44]. The exact magnitude of the surface dose increase will depend on the fringe magnetic field configuration and magnitude[42,45].

All these dose deposition modifications have been previously investigated using Monte Carlo simulation packages like Geant4[37,44,46,47] , EGSnrc[38,43,45,48] and PENELOPE[49,50]. While

Geant4 dose calculations in the presence of strong magnetic fields have been validated against measurements[47], EGSnrc has only had limited experimental validation with magnetic fields[51] prior to the current work. A precise understanding of the dose modifications that arise when irradiating a patient inside an MRI is paramount to the clinical implementation of integrated linac MR units. The work presented herein investigates the surface and buildup dose increases caused by various typical, off-the-shelf RF coil materials, as well as extends the EGSnrc Monte Carlo experimental verification in the presence of a parallel magnetic field.

Chapter 2 contains the background theory pertaining to the work presented in this thesis. The basic types of interactions of high energy photons with matter are introduced, and the relative probabilities of each type of interaction as a function of energy are discussed. The concepts of kerma, dose and charged particle equilibrium are then briefly explained, including their inter-relationships. Since throughout the work presented herein, ion chambers have been used to measure dose, an overview of Bragg-Gray and Spencer-Attix cavity theories is presented. This reveals some of the assumptions behind relating charge measured using an ion chamber to the dose absorbed in the medium. The following theory section presents a brief overview of electromagnetism, introducing Maxwell's equations, and the force that charged particles moving in a magnetic field will experience. After a general introduction to Monte Carlo, including some basic probability theory, the EGSnrc Monte Carlo system is introduced. The electromagnetic field implementation of EGSnrc is presented in some detail. The chapter ends detailing the assumptions needed in order to decouple all the forces acting on a charged particle which will allow for a complete Monte Carlo simulation of charged particle transport in an external magnetic field.

Chapter 3 presents the investigation of the surface and buildup dose increase caused by several standard off-the-shelf RF coil materials[52]. A surface coil is approximated using layered sheets of polycarbonate, copper tape, and Teflon, emulating the base, conductor, and cover, respectively. This imitation surface coil, as well as other typical RF coil materials were placed in the path of a 6 MV photon beam at various distances from the surface of polystyrene phantoms. The surface and buildup dose was measured with each of these materials in the high energy beam in the presence of a transverse magnetic field, a parallel magnetic field and with no magnetic field present and the results compared.

In Chapter 4 the accuracy of EGSnrc Monte Carlo calculated depth doses in polystyrene in the presence of a realistic magnetic field was investigated[53]. A parallel plate ion chamber was used to take measurements in a polystyrene phantom inserted in a bore created by placing two electromagnets on top of each other. Depth doses were measured with and without the parallel magnetic field turned on with the phantom placed at two separate locations within the electromagnet bore. A three dimensional magnetic field map of the electromagnet was simulated and validated using measurements. The linac that provided the irradiation was modeled using the specialized EGSnrc package BEAMnrc, and validated against the commissioning measurements for that particular unit. The experimental setup was simulated using the phase space thus obtained, both with and without the 3D magnetic field map implemented in EGSnrc. The resulting percent depth doses were compared to measurements.

Chapter 5 experimentally verifies the accuracy of EGSnrc calculated depth doses in lung in the presence of a parallel magnetic field. The previously validated magnetic field map and phase space[53] were used to simulate the depth dose in lung and compare the results with measurements done in Gammex lung equivalent material.

Chapter 6 presents the general summary and conclusion of all the work presented in the current thesis.

1.8 References

1. Canadian Cancer Society, "Cancer Information," http://www.cancer.ca (2018).

2. *Vital statistics: Death database, CANSIM Table 102-0561*, http://www5.statcan.gc.ca/cansim/a05?lang=eng&id=1020561#F11 (n.d.).

3. *Canadian Cancer Society's Advisory Committee on Cancer Statistics. Canadian Cancer Statistics 2017* (Toronto, ON: Canadian Cancer Society, 2017).

4. R. Siegel, C. Desantis, K. Virgo, K. Stein, A. Mariotto, T. Smith, D. Cooper, T. Gansler, C. Lerro, S. Fedewa, C. Lin, C. Leach, R.S. Cannady, H. Cho, S. Scoppa, M. Hachey, R. Kirch, A. Jemal, and E. Ward, "Cancer Treatment and Survivorship Statistics , 2012," CA. Cancer J. Clin. **62**, 220–241 (2012).

5. O. Glasser, *Wilhelm Conrad Rontgen and the early history of Roentgen Rays* (Charles C Thomas, Springfield, Illinois, 1934).

6. J. Bernier, E.J. Hall, and A. Giaccia, "Radiation oncology: A century of achievements," Nat. Rev. Cancer **4**(9), 737–747 (2004).

7. C.A. Perez, L.W. Brady, and J.L. Roti, *Principles and Practice of Radiation Oncology*, 3rd ed. (Lippincott-Raven, Philadelphia, PA, 1998).

8. S.F. Kry, S. a. Smith, R. Weathers, and M. Stovall, "Skin dose during radiotherapy: A summary and general estimation technique," J. Appl. Clin. Med. Phys. 13(3), 20–34 (2012).

9. A.J. Olch, L. Gerig, H. Li, I. Mihaylov, and A. Morgan, "Dosimetric effects caused by

couch tops and immobilization devices: Report of AAPM Task Group 176," Med. Phys. 41(6), 1–30 (2014).

10. J. Van Dyk, *The Modern Technology of Radiation Oncology* (Medical Physics Publishing, Madison, Wisconsin, 1999).

11. G. Failla, "An Objective Method for the Administration of X-Rays," Acta radiol. **4**, 85–128 (1925).

12. International Commission on Radiation Units and Measurements, *ICRU Report 50: Prescribing, Recording, and Reporting Photon Beam Therapy* (Bethesda, Maryland, 1993).

13. L.A. Dawson and D.A. Jaffray, "Advances in image-guided radiation therapy," J. Clin. Oncol. **25**(8), 938–946 (2007).

14. J.D. Bourland (ed.), *Image-Guided Radiation Therapy* (Taylor & Francis Group, Boca Raton, FL, 2012).

15. D. Verellen, M. De Ridder, N. Linthout, K. Tournel, G. Soete, and G. Storme, "Innovations in image-guided radiotherapy," Nat. Rev. Cancer **7**(12), 949–960 (2007).

16. G.X. Ding and P. Munro, "Radiation exposure to patients from image guidance procedures and techniques to reduce the imaging dose," Radiother. Oncol. **108**(1), 91–98 (2013).

17. Y. Li, T. Netherton, P.L. Nitsch, P.A. Balter, S. Gao, A.H. Klopp, and L.E. Court, "Normal tissue doses from MV image-guided radiation therapy (IGRT) using orthogonal MV and MV-CBCT," J. Appl. Clin. Med. Phys. **19**(3), 52–57 (2018).

18. L.A. Dawson and M.B. Sharpe, "Image-guided radiotherapy: rationale, benefits, and limitations," Lancet Oncol. **7**(10), 848–858 (2006).

19. H. Shirato, S. Shimizu, K. Kitamura, T. Nishioka, K. Kagei, S. Hashimoto, H. Aoyama, T. Kunieda, N. Shinohara, H. Dosaka-Akita, and K. Miyasaka, "Four-dimensional treatment planning and fluoroscopic real-time tumor tracking radiotherapy for moving tumor," Int. J. Radiat. Oncol. Biol. Phys. **48**(2), 435–442 (2000).

20. J. Pouliot, A. Bani-Hashemi, Josephine Chen, M. Svatos, F. Ghelmansarai, M. Mitschke, M. Aubin, P. Xia, O. Morin, K. Bucci, M. Roach, P. Hernandez, Z. Zheng, D. Hristov, and L. Verhey, "Low-dose megavoltage cone-beam CT for radiation therapy," Int. J. Radiat. Oncol. Biol. Phys. **61**(2), 552–560 (2005).

21. B.A. Groh, J.H. Siewerdsen, D.G. Drake, J.W. Wong, and D.A. Jaffray, "A performance comparison of flat-panel imager-based MV and kV cone-beam CT," Med. Phys. **29**(6), 967–975 (2002).

22. E.K. Hansen, D.A. Larson, M. Aubin, J. Chen, M. Descovich, A.M. Gillis, O. Morin, P. Xia, and J. Pouliot, "Image-guided radiotherapy using megavoltage cone-beam computed tomography for treatment of paraspinous tumors in the presence of orthopedic hardware," Int. J. Radiat. Oncol. Biol. Phys. **66**(2), 323–326 (2006).

23. D. Ionascu, S.B. Jiang, S. Nishioka, H. Shirato, and R.I. Berbeco, "Internal-external correlation investigations of respiratory induced motion of lung tumors," Med. Phys. **34**(10), 3893–3903 (2007).

24. E.M. Haacke, R.W. Brown, M.R. Thompson, and R. Venkatesan, *Magnetic Resonance*

Imaging Physicsl Principles and Sequence Design (Wiley-Liss John Wiley & Sons, Inc., New York, 1999).

25. P. Metcalfe, G.P. Liney, L. Holloway, A. Walker, M. Barton, G.P. Delaney, S. Vinod, and W. Tomé, "The Potential for an Enhanced Role for MRI in Radiation-Therapy Treatment Planning," Technol. Cancer Res. Treat. **12**(5), 429–446 (2013).

26. B.G. Fallone, B. Murray, S. Rathee, T. Stanescu, S. Steciw, S. Vidakovic, E. Blosser, and D. Tymofichuk, "First MR images obtained during megavoltage photon irradiation from a prototype integrated linac-MR system," Med. Phys. **36**(6), 2084–2088 (2009).

27. B.W. Raaymakers, J.J.W. Lagendijk, J. Overweg, J.G.M. Kok, A.J.E. Raaijmakers, E.M. Kerkhof, R.W. van der Put, I. Meijsing, S.P.M. Crijns, F. Benedosso, M. van Vulpen, C.H.W. de Graaff, J. Allen, and K.J. Brown, "Integrating a 1.5 T MRI scanner with a 6 MV accelerator: proof of concept.," Phys. Med. Biol. **54**(12), N229–N237 (2009).

28. J.F. Dempsey, D. Benoit, J.R. Fitzsimmons, A. Haghighat, J.G. Li, D. a. Low, S. Mutic, J.R. Palta, H.E. Romeijn, and G.E. Sjoden, "A Device for Realtime 3D Image-Guided IMRT," Int. J. Radiat. Oncol. **63**(2), S202 (2005).

29. M. Lamey, J. Yun, B. Burke, S. Rathee, and B.G. Fallone, "Radio frequency noise from an MLC: A feasibility study of the use of an MLC for linac-MR systems," Phys. Med. Biol. **55**(4), 981–994 (2010).

30. M. Lamey, B. Burke, E. Blosser, S. Rathee, N. De Zanche, and B.G. Fallone, "Radio frequency shielding for a linac-MRI system," Phys. Med. Biol. **55**(4), 995–1006 (2010).

31. B. Burke, B.G. Fallone, and S. Rathee, "Radiation induced currents in MRI RF coils:

Application to linac/MRI integration," Phys. Med. Biol. **55**(3), 735–746 (2010).

32. B. Burke, A. Ghila, B.G. Fallone, and S. Rathee, "Radiation induced current in the RF coils of integrated linac-MR systems: The effect of buildup and magnetic field," Med. Phys. **39**(8), 5004–5014 (2012).

33. E. Yip, J. Yun, K. Wachowicz, A. Heikal, Z. Gabos, S. Rathee, and B.G. Fallone, "Prior data assisted compressed sensing: A novel MR imaging strategy for real time tracking of lung tumours," Med. Phys. **41**(8), 1–12 (2014).

34. J. Yun, E. Yip, Z. Gabos, K. Wachowicz, S. Rathee, and B.G. Fallone, "Neural-network based autocontouring algorithm for intrafractional lung-tumor tracking using Linac-MR," Med. Phys. **42**(5), 2296–2310 (2015).

35. B. Dietz, E. Yip, J. Yun, B.G. Fallone, and K. Wachowicz, "Real-time dynamic MR image reconstruction using compressed sensing and principal component analysis (CS-PCA): Demonstration in lung tumor tracking," Med. Phys. **44**(8), 3978–3989 (2017).

36. A.J. Olch, L. Gerig, H. Li, I. Mihaylov, and A. Morgan, "Dosimetric effects caused by couch tops and immobilization devices: Report of AAPM Task Group 176," Med. Phys. **41**(6), 1–30 (2014).

37. A.J.E. Raaijmakers, B.W. Raaymakers, and J.J.W. Lagendijk, "Integrating a MRI scanner with a 6 MV radiotherapy accelerator: dose increase at tissue-air interfaces in a lateral magnetic field due to returning electrons.," Phys. Med. Biol. **50**(7), 1363–1376 (2005).

38. A. Keyvanloo, B. Burke, J.S. Aubin, D. Baillie, K. Wachowicz, B. Warkentin, S. Steciw, and B.G. Fallone, "Minimal skin dose increase in longitudinal rotating biplanar linac-MR

systems : examination of radiation energy and flattening filter design," Phys. Med. Biol. **61**, 3527–3539 (2016).

39. A.J.E. Raaijmakers, B.W. Raaymakers, and J.J.W. Lagendijk, "Magnetic-field-induced dose effects in MR-guided radiotherapy systems: dependence on the magnetic field strength," Phys. Med. Biol. 53(4), 909–923 (2008).

40. B.W. Raaymakers, A.J.E. Raaijmakers, A.N.J. Kotte, D. Jette, and J.J.W. Lagendijk, "Integrating a MRI scanner with a 6 MV radiotherapy accelerator: dose deposition in a transverse magnetic field," Phys. Med. Biol. 49, 4109–4118 (2004).

41. A J E Raaijmakers, B Hardemark, B W Raaymakers, C P J Raaijmakers and J J W Lagendijk, "Dose optimization for the MRI-accelerator: IMRT in the presence of a magnetic field" Phys. Med. Biol. 52, 7045 – 7054 (2007).

42. B.M. Oborn, P.E. Metcalfe, M.J. Butson, a. B. Rosenfeld, and P.J. Keall, "Electron contamination modeling and skin dose in 6 MV longitudinal field MRIgRT: Impact of the MRI and MRI fringe field," Med. Phys. 39(2), 874–890 (2012).

43. C. Kirkby, B. Murray, S. Rathee, and B.G. Fallone, "Lung dosimetry in a linac-MRI radiotherapy unit with a longitudinal magnetic field," Med. Phys. **37**(9), 4722–4732 (2010).

44. B.M. Oborn, S. Kolling, P.E. Metcalfe, S. Crozier, D.W. Litzenberg, and P.J. Keall, "Electron contamination modeling and reduction in a 1 T open bore inline MRI-linac system.," Med. Phys. **41**(5), 1–15 (2014).

45. A. Keyvanloo, B. Burke, B. Warkentin, T. Tadic, S. Rathee, C. Kirkby, D.M. Santos, and

B.G. Fallone, “Skin dose in longitudinal and transverse linac-MRIs using Monte Carlo and realistic 3D MRI field models,” Med. Phys. **39**(10), 6509–6521 (2012).

46. B.M. Oborn, P.E. Metcalfe, M.J. Butson, and a B. Rosenfeld, “Monte Carlo characterization of skin doses in 6 MV transverse field MRI-linac systems: effect of field size, surface orientation, magnetic field strength, and exit bolus.,” Med. Phys. **37**(10), 5208–5217 (2010).

47. A.J.E. Raaijmakers, B.W. Raaymakers, and J.J.W. Lagendijk, “Experimental verification of magnetic field dose effects for the MRI-accelerator.,” Phys. Med. Biol. **52**(14), 4283–4291 (2007).

48. C. Kirkby, T. Stanescu, S. Rathee, M. Carlone, B. Murray, and B.G. Fallone, “Patient dosimetry for hybrid MRI-radiotherapy systems,” Med. Phys. **35**(3), 1019–1027 (2008).

49. M. Reynolds, B.G. Fallone, and S. Rathee, “Dose response of selected ion chambers in applied homogeneous transverse and longitudinal magnetic fields,” Med. Phys. **40**(4), 1–7 (2013).

50. M. Reynolds, B.G. Fallone, and S. Rathee, “Dose response of selected solid state detectors in applied homogeneous transverse and longitudinal magnetic fields,” Med. Phys. **41**(9), 1–12 (2014).

51. V.N. Malkov and D.W.O. Rogers, “Charged particle transport in magnetic fields in EGSnrc,” Med. Phys. **43**(7), 4447–4458 (2016).

52. A. Ghila, B.G. Fallone, and S. Rathee, “Influence of standard RF coil materials on surface and buildup dose from a 6 MV photon beam in magnetic field,” Med. Phys.

43(11), 5808–5816 (2016).

53. A. Ghila, S. Steciw, B.G. Fallone, and S. Rathee, "Experimental verification of EGSnrc Monte Carlo calculated depth doses within a realistic parallel magnetic field in a polystyrene phantom," Med. Phys. **44**(9), 4804–4815 (2017).

Chapter 2: Theory

2.1 Interactions of High Energy Photons with Matter

When high energy photons traverse through matter, some of the photons' energy will be transferred to the matter. The energy transfer happens through various types of interactions whose probabilities depend on the photon's energy ($h\nu$) and the atomic number (Z) of the specific material being irradiated. The main interaction types are: Rayleigh (or coherent) scattering, the photoelectric effect, Compton (or incoherent) scattering, pair and triplet production, and photonuclear interactions[1,2].

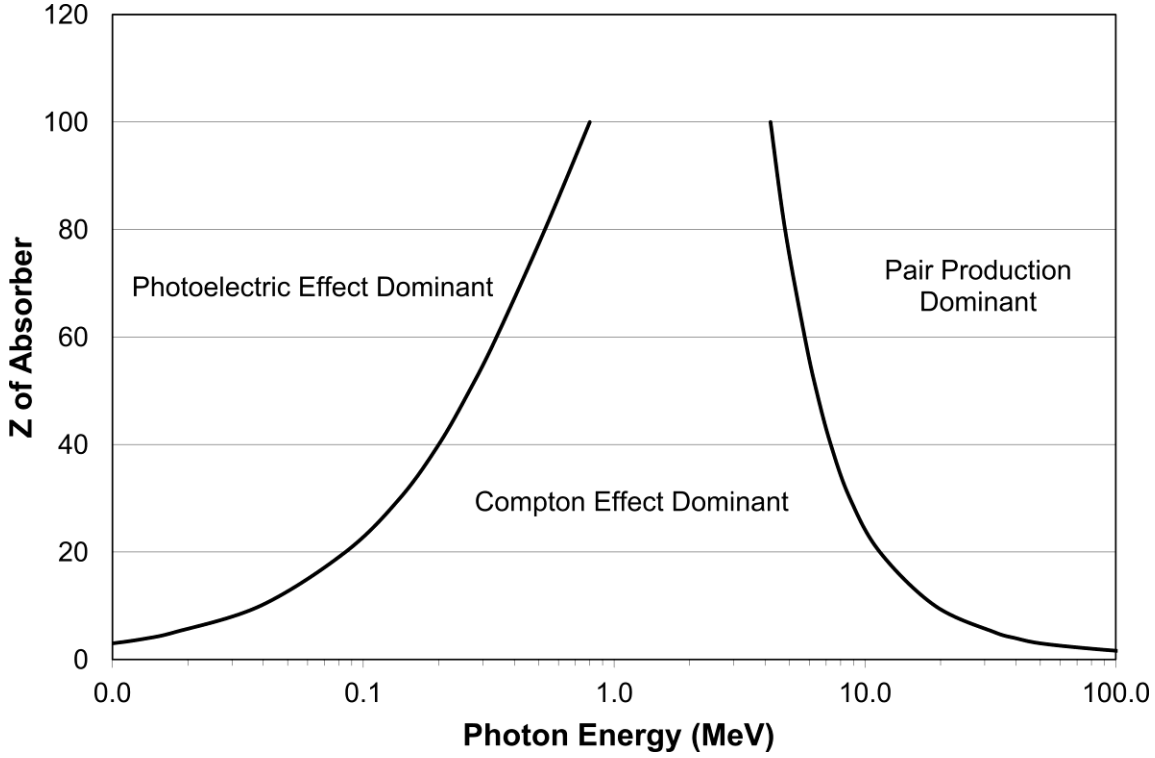

Figure 2.1 Relative importance of the three major types of high energy photon interactions. The solid lines represent the atomic numbers and photon energies for which two adjacent interactions have approximately the same probability.

For the photon energy range used in radiation therapy, the middle three are the most dominant in transferring energy to the irradiated medium by ionizing atoms and setting electrons in motion, processes which have the potential to cause biological damage[1,2]. Figure 2.1 above shows the regions in which a particular type of interaction is dominant as a function of both the photon energy and the atomic number. The data used to create this figure has been taken directly from NIST[3]. The solid lines in the figure represent the atomic number of materials as a function of energy for which the two neighboring interaction types have approximately the same probability of occurring. It can be seen that in the range of therapeutic photon energies (from ~1 to 10 MeV), Compton scattering is the most probable interaction for most materials. However for completeness purposes and as a preface to the subsequent Monte Carlo method description, each one of the previously mentioned interactions will be discussed below in more detail.

2.1.1 Rayleigh (Coherent) Scattering

Rayleigh scattering occurs when a photon (i.e. electromagnetic wave) passes over an atom and the photon's associated electric field sets the atom's electrons into momentary vibration. The oscillating electrons subsequently emit an electromagnetic wave of the same wavelength as the original photon. The electromagnetic waves from all the affected electrons combine to form the scattered wave. In this process, the interacting photons do not loose energy but only slightly change their propagation direction thereby the incident beam is slightly broadened. The probability of coherent scattering (also known as the cross section) is denoted as σ_{coh} and it decreases rapidly with increasing photon energy, being negligible for energies above ~100 keV[1,2].

2.1.2 The Photoelectric Effect

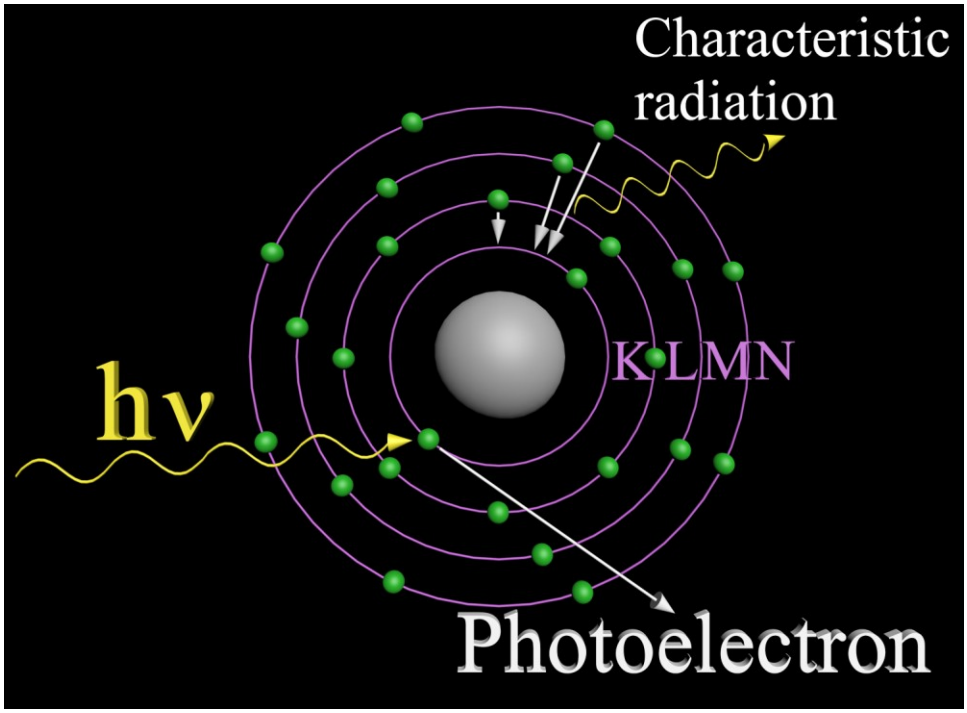

Figure 2.2 Representation of the interaction of a high energy photon with an atomic electron resulting in the ejection of a photoelectron from the K shell.

The photoelectric effect, schematically shown in Figure 2.2, consists of a high energy photon of energy $h\nu$ colliding with one of the K, L, M, or N shell electrons. The interacting, bound electron (i.e. the *photoelectron*) is ejected with a kinetic energy $h\nu$ - E_b and the photon ceases to exist. Here E_b is the binding energy of the shell from which the electron is ejected. The excited atom returns to ground state by transitioning another electron from the higher energy shells to fill the gap vacated by the ejected electron. This electron transition is accompanied by the emission of *characteristic radiation* accounting for the difference between the atomic energy levels. Any excess energy, not removed from the atom by the characteristic radiation, results in

the spontaneous ejection of *Auger electron(s)* with combined kinetic energy accounting for the excess energy of the atom[1,2].

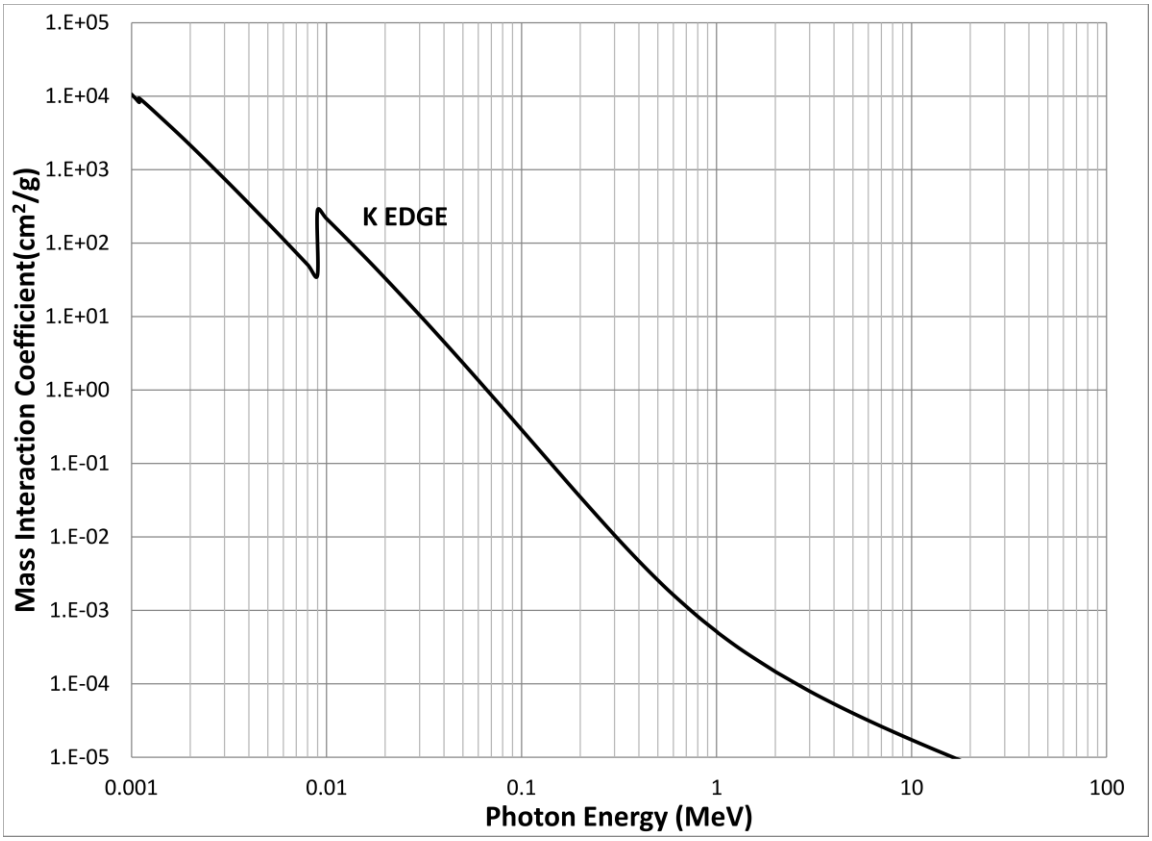

Figure 2.3 Photoelectric effect cross section (τ) for Copper. The K edge discontinuity is readily visible when the photons have enough energy to ionize the atom's K shell. Data from NIST.

The photoelectric effect probability (τ) decreases quite rapidly with increasing energy of the incident photon approximately as $1/(h\nu)^3$. Abrupt, discontinuous increases in the photoelectric cross section occur when the incident photon has just enough energy to remove an electron from its shell. Figure 2.3 illustrates one of these discontinuous increases in the photoelectric cross section for copper, for a photon energy of ~9 keV. In copper, below 9 keV, the two K shell electrons cannot participate in the photoelectric process since their binding energy E_b is greater than the incident photon energy. As the photon energy increases past E_b of

the K-edge, the K-shell electrons can also participate in the photoelectric process resulting in a sharp increase in τ. The photoelectric cross section also increases with increasing atomic number. The cross section per atom varies roughly like $Z^{4.8}$ for low atomic number materials, and like Z^4 for high atomic number materials[1,2].

2.1.3 Compton (Incoherent) Scattering

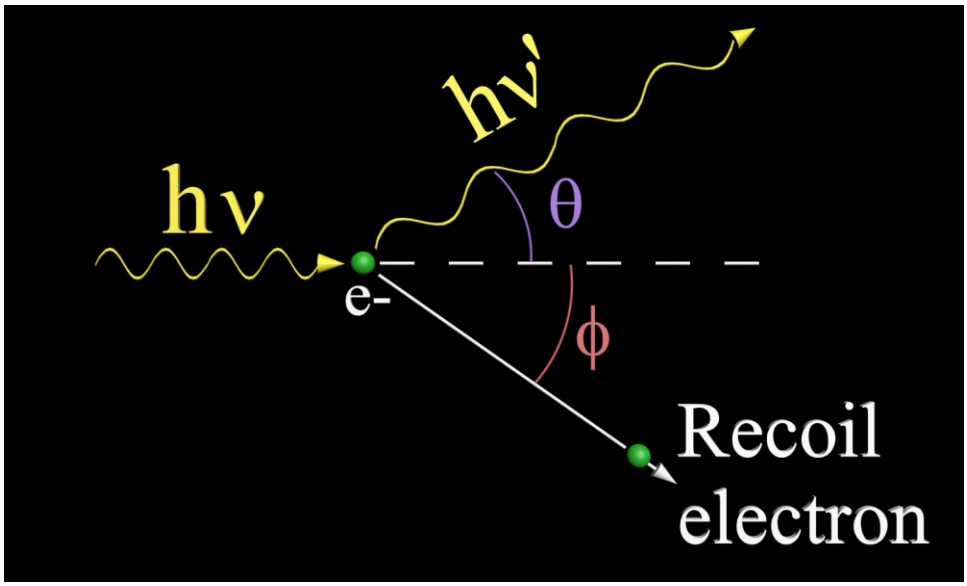

Figure 2.4 Representation of the Compton scattering process, where a photon ($h\nu$) transfers some of its energy to a free electron resulting in a recoil electron and a lower energy scattered photon ($h\nu'$).

During a Compton (or incoherent) collision, a high energy photon interacts with a loosely bound electron, and a fraction of the photon's initial energy $h\nu$ is transferred to the electron. Following a Compton interaction, the electron is set in motion with a kinetic energy E at an angle ϕ while the scattered photon of energy $h\nu'$ (= $h\nu$ – E) is deflected at an angle θ, as schematically illustrated in Figure 2.4.

Using the notation in Figure 2.4, and the laws of conservation of energy and momentum, it can be shown that:

$$h\nu' = \frac{h\nu}{1 + \alpha(1 - \cos\theta)} \tag{2.1}$$

This means that the energy of the scattered electron is:

$$E = h\nu - h\nu' = h\nu \frac{\alpha(1 - \cos\theta)}{1 + \alpha(1 - \cos\theta)} \tag{2.2}$$

where α is the ratio of the incident photon energy to the electron rest energy

$$\alpha = \frac{h\nu}{m_0 c^2} \tag{2.3}$$

with m_0 representing the electron's rest mass, and c the speed of light in vacuum[1,2].

Using quantum mechanical reasoning, Klein and Nishina have derived an analytical expression for the probability of a Compton collision. This was calculated as the probability of the system to go from its initial state (stationary unbound electron and photon with energy $h\nu$) to its final state (electron with energy E and photon with energy $h\nu'$). Their calculations yielded the differential cross section ($d\sigma$) per unit solid angle ($d\Omega$) to be:

$$\frac{d\sigma}{d\Omega} = \frac{r_0^2}{2}(1 + \cos\theta^2) \cdot F_{KN} \tag{2.4}$$

r_0 is the classical electron radius, defined as the radius of a sphere having the electron charge ($e = 1.6022 \times 10^{-19} C$) that was assembled entirely due to the electron's relativistic mass-energy (m_0c^2):

$$r_0 = \frac{1}{4\pi\varepsilon_0}\frac{e^2}{m_0 c^2} = 2.8179 \times 10^{-15} m \tag{2.5}$$

where the constant ε_0 is the *permittivity of free space* ($\varepsilon_0 = 8.8542 \times 10^{-12} F/m$).

The Klein-Nishina factor F_{KN} in equation (2.4) is given by:

$$F_{KN} = \left\{\frac{1}{1+\alpha(1-\cos\theta)}\right\}^2 \left\{1 + \frac{\alpha^2(1-\cos\theta)^2}{[1+\alpha(1-\cos\theta)](1+\cos^2\theta)}\right\} \qquad (2.6)$$

As before, α is given by Equation (2.3), and the angle θ is the photon's scattering angle as seen in Figure 2.4.

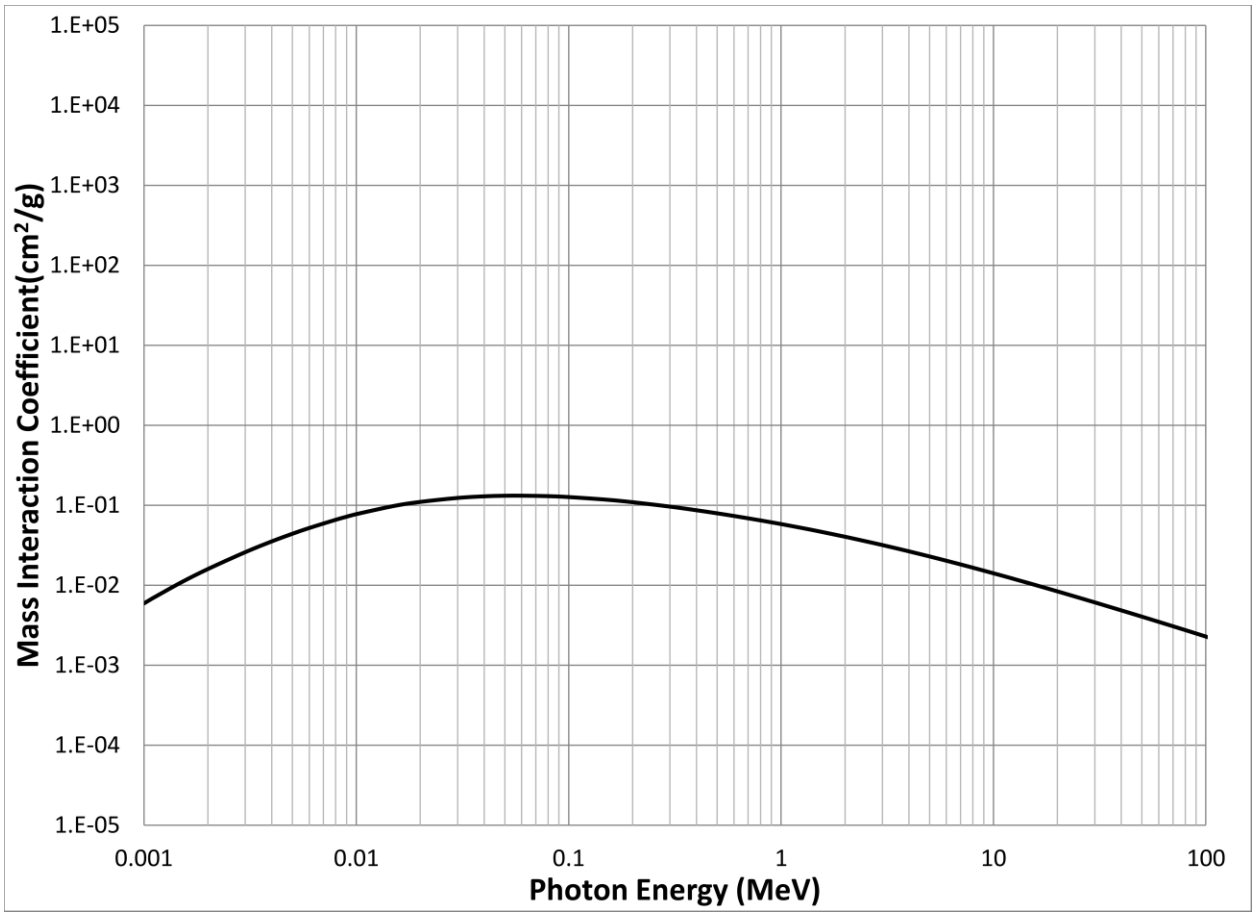

Figure 2.5 Compton (incoherent) scattering cross section (σ_{inc}) for Copper. Data from the NIST.

In order to obtain the total probability of the Compton (incoherent) scattering process, equation (2.4) is multiplied by $d\Omega = 2\pi \sin\theta \, d\theta$ and integrated over all angles. Thus:

$$\sigma_{inc} = 2\pi r_0^2 \left\{ \left(\frac{1+\alpha}{\alpha^2} \right) \left[\frac{2(1+\alpha)}{1+2\alpha} - \frac{\ln(1+2\alpha)}{\alpha} \right] + \frac{\ln(1+2\alpha)}{2\alpha} - \frac{1+3\alpha}{(1+2\alpha)^2} \right\} \quad (2.7)$$

For this derivation the electron was assumed to be free, which results in a very small overestimation of σ_{inc}, and makes σ_{inc} independent of atomic number Z. Any substantial overestimation occurs for energies below ~10 keV, where the photoelectric effect is far more likely than Compton. The Compton process is the dominant interaction[1,2] in the radiotherapy energy range, and it slowly decreases with increasing energy as can be seen in Figure 2.5.

2.1.4 Pair and Triplet Production

In the pair production process, a photon spontaneously disappears in the Coulomb field of an atom and an electron-positron pair is created to conserve energy and charge. However if this process takes place in the Coulomb field of another electron, it is called triplet production, since the original electron also acquires a substantial kinetic energy, and there are two electrons and a positron leaving the interaction site. Pair production in the nuclear field occurs for a threshold photon energy $\geq 2m_0c^2 = 1.022\ MeV$.

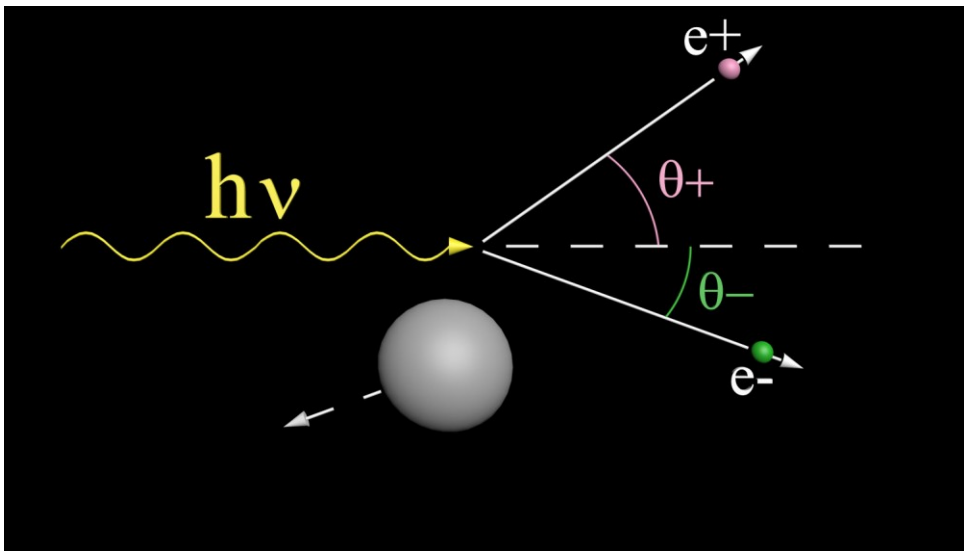

Figure 2.6 Representation of the pair production process in the Coulomb field of a nucleus.

Any energy in excess of 1.022 MeV is shared between the electron and the positron as follows:

$$h\nu - 2m_0c^2 = E_- + E_+ \qquad (2.8)$$

Where E_- and E_+ are the kinetic energies of the electron and the positron respectively. The distribution of the excess energy between the two particles is virtually a continuous spectrum. One extreme is where, following a pair production interaction, one particle emerges with almost all the excess energy while the other gets essentially none, or the two particles can both emerge with essentially identical kinetic energies[1,2].

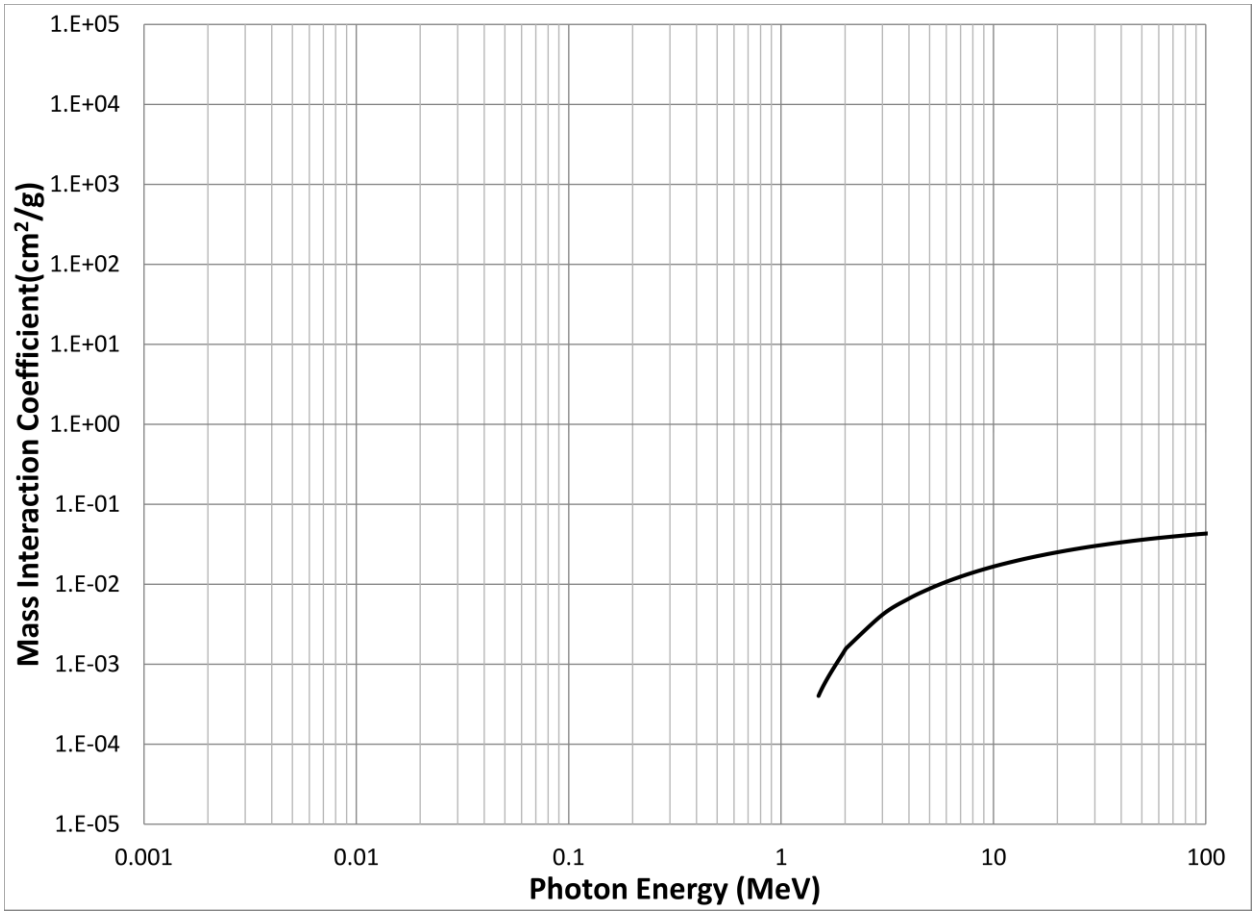

Figure 2.7 Pair production cross section (κ) for Copper. Data from the NIST.

The cross section per unit mass for pair production (κ) is proportional to the atomic number of the irradiated material (Z). Above the 1.022 MeV threshold, the pair production probability increases rapidly with increasing energy (see Figure 2.7), becoming the dominant interaction for most materials for photon energies above 10 MeV.

2.1.5 Photonuclear Interactions

In the photonuclear interaction process an energetic photon ($h\nu$ in excess of several MeV) excites the atomic nucleus which emits a proton or neutron while returning to ground state. Although the emitted protons are directly ionizing particles and do contribute to the total dose, their contribution is usually negligible in comparison to the other types of interactions. Photonuclear interactions are responsible for the neutron contamination of the poly-energetic therapeutic x-ray beams produced by clinical x-ray generators (linacs, betatrons or microtrons) that have peak photon energies > 10 MeV. Thus, photonuclear interaction becomes important from a radiation protection standpoint, and is taken into account when designing radiation vault shielding or when servicing x-ray generator components that might have been activated by the neutrons[2].

2.2 Exponential Attenuation

As a high energy photon beam traverses a material, the photons interact with the medium via the aforementioned processes. Following a photon interaction, whether its path is simply deflected or it is completely absorbed and ceases to exist, the photon is said to have been removed from the beam. Thus, if a photon beam containing N photons passes through a thin absorber, it will emerge on the other side containing fewer photons. The beam is said to have been attenuated by the absorber with the attenuation following the well-known exponential law

$$N = N_0 e^{-\mu_{tot} x} \tag{2.9}$$

Equation (2.9) allows us to calculate the number of photons that are left in a beam that originally had N_0 photons after passing through an absorber of thickness x[1].

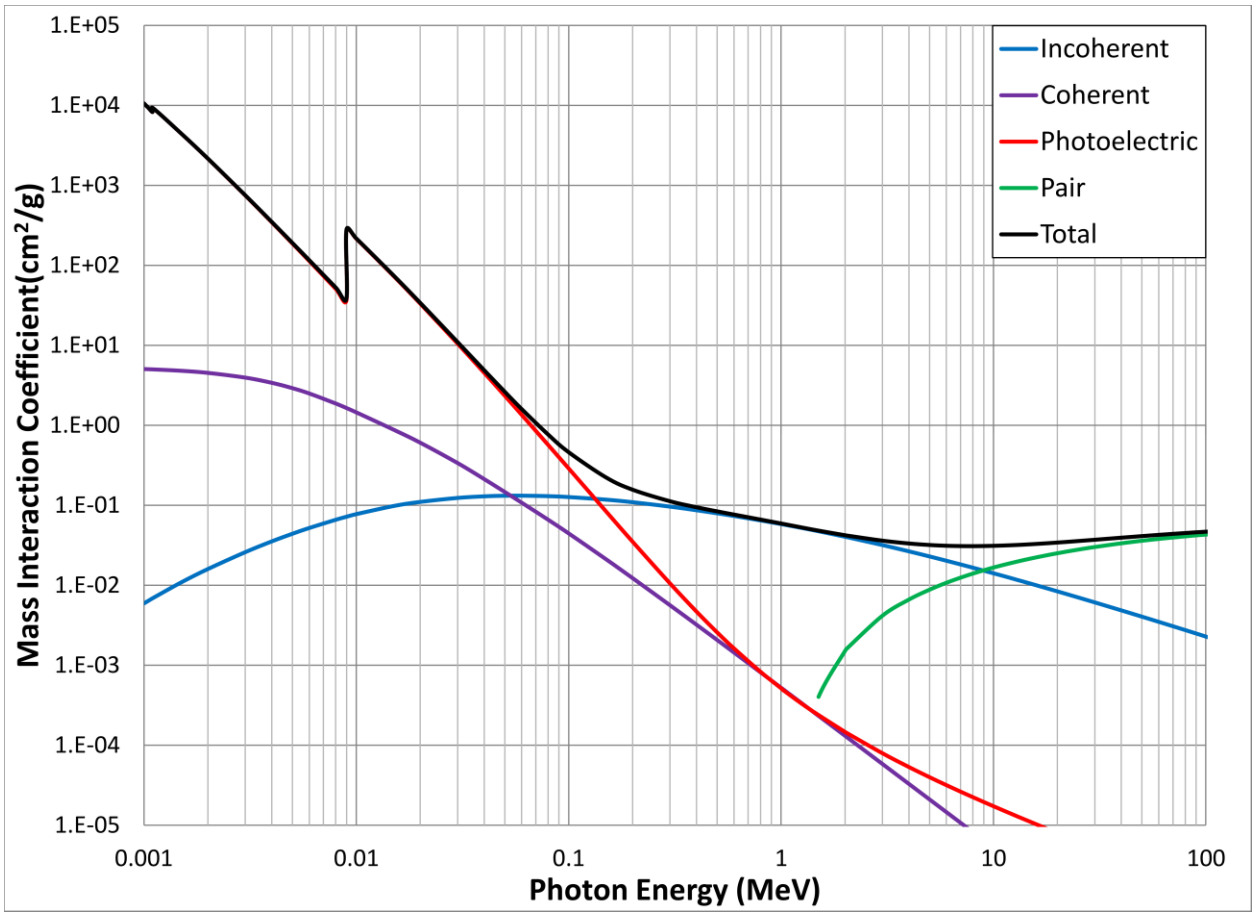

Figure 2.8 Mass attenuation coefficient as a function of incident photon energy for copper. Each one of the interactions that are important in the radiotherapeutic energy range is represented as well as the total mass attenuation coefficient. (Data from NIST).

The total interaction coefficient (μ_{tot}) will be the sum of the interaction coefficients for each individual type of interaction:

$$\mu_{tot} = \sigma_{coh} + \tau + \sigma_{inc} + \kappa \tag{2.10}$$

With σ_{coh}, τ, σ_{inc}, and κ representing the attenuation coefficients for coherent scattering, photoelectric effect, Compton scattering, and pair production, respectively, as described in the previous section.

Figure 2.8 shows the total mass attenuation coefficient of copper as well as the contribution of various interaction types as a function of photon energy. The energy regions where a type of interaction is dominant are indicated by the near overlap between the total mass attenuation coefficient and that of the dominant interaction.

2.3 Electron Interactions

Electrons, as well as charged particles in general, interact with matter differently than uncharged particles (photons, or neutrons). While an uncharged particle could potentially go through a layer of matter without interacting, charged particles, surrounded by their Coulomb field, have practically zero probability of passing through matter with no interactions[2]. As an energetic charged particle traverses a medium, its electric field interacts with the electric field of the charged particles present in the medium. This interaction constitutes the main reason that the energetic charged particle loses its kinetic energy to the medium[1].

As energetic electrons move through the medium they can excite and sometimes ionize the nearby atoms. If the energetic electrons pass in close proximity to an atom, an orbital electron can be set in motion via a knock-on collision. Energetic electrons can also travel in close proximity to the atomic nucleus. In most such cases, the energetic electrons scatter elastically loosing very little energy. However, due to the very small mass of electrons, their interaction with the Coulomb field of the nucleus can sometimes cause the electron to be decelerated

rapidly. This causes the electron to lose a considerable portion of its energy via radiative losses, a phenomenon known as the *Bremsstrahlung* (or "braking") radiation[1, 2].

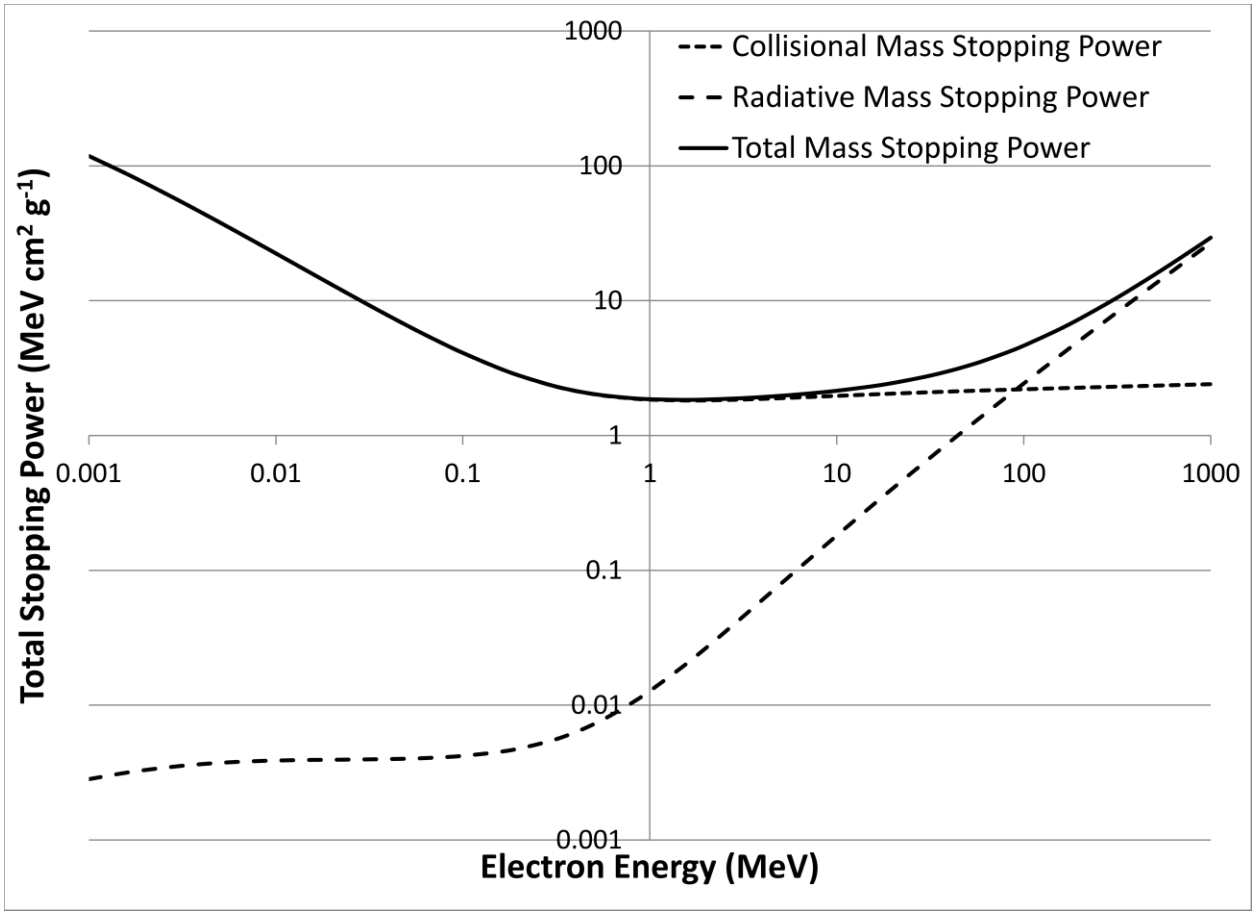

Figure 2.9 The collisional, radiative, and total mass stopping power as a function of incident electron energy for water. Data from NIST.

The amount of energy lost per unit path length along the track of a particle is called the linear *stopping power* (*S*). The units for the stopping power are either *J/m* or *MeV/cm*. The *mass stopping power* is obtained by dividing the linear stopping power by the density of the absorbing medium with units of either $J\ m^2/kg$ or $MeV\ cm^2/g$. The stopping power is further divided into *collisional stopping power* and *radiative stopping power*. The collisional stopping power is the macroscopic energy lost per unit path length via excitations and ionizations, while the radiative stopping power is the macroscopic energy lost via radiative interactions (usually

Bremsstrahlung)[2]. Figure 2.9 shows the collisional, radiative, and the total mass stopping power of water as a function of the incident electron energy. At low energies, the stopping power is inversely proportional to the energy. As the energy increases, the stopping power decreases, reaching a minimum around 1.0 MeV. In tissue like materials the total stopping power is due almost entirely to the collisional interactions up to ~ 10 MeV.

2.4 Kerma and Dose

The transfer of the photon energy to the irradiated material is a two step process. In the first step, the photon transfers all, or part, of its energy to charged particles, usually orbital electrons, through one of the processes described in Section 2.1. The second step consists of the energetic charged particles (also called secondary, or directly ionizing particles) transferring their excess energy to the surrounding medium as discussed in the previous section. The quantity describing the energy transfer from the photons to the irradiated medium is called *kerma* which stands for Kinetic Energy Released per unit Mass of the medium. *Kerma* is defined as:

$$Kerma; K = \frac{d\overline{E_{tr}}}{dm} \tag{2.11}$$

where $d\overline{E_{tr}}$ represents the mean energy transferred from the photons to the secondary electrons within a volume *dV* with mass *dm*. Kerma is typically expressed in units of J/kg and it accounts for all of the energy that the photon beam looses to the medium, whether this energy stays in the medium or escapes by Bremsstrahlung photons, which have the potential to escape the medium. Thus, *kerma* can be split into two components: the *collision kerma* (K_c) and the *radiative kerma* (K_r). The *collision kerma* accounts for the energy transferred from photons to charged particles, energy that is subsequently spent by the charged particles through various excitations and ionizations. This energy is assumed to stay in the medium. The *radiative kerma* accounts for the

part of the energy that although is initially transferred to charged particle kinetic energy, is subsequently converted back to photon energy. Thus we can write:

$$K = K_c + K_r \tag{2.12}$$

Theoretically, *kerma* can be calculated if the terms in Equation (2.11) are known, however they are extremely difficult to accurately measure experimentally. Absorbed dose on the other hand, can readily be measured, and is defined as:

$$Absorbed\ Dose; D = \frac{d\overline{E_{ab}}}{dm} \tag{2.13}$$

with $d\overline{E_{ab}}$ representing the mean energy absorbed by a mass *dm*. The units of absorbed dose are the same as the ones for *kerma*, but unlike for *kerma*, the unit for absorbed dose has a special name: *the gray* (Gy). Thus the gray is defined as: 1 Gy = 1 J/kg. The *absorbed dose* accounts for only the part of the energy that is retained inside the medium. The *kerma* and the *absorbed dose*, do not take place at the same spot along the path of a photon beam. *Kerma* happens at the spot where a primary photon transfers energy to a charged particle and sets it in motion with a certain kinetic energy. The dose is the energy absorbed by the medium along the path over which the charged particle slows downs and comes to rest[1].

2.5 Charged Particle Equilibrium

Charged particle equilibrium (*CPE*) is said to exist in a volume V if for every type of particle of a certain energy leaving V another particle of the same energy and type enters that volume[2]. Since electrons are the majority of the charged particles participating in establishing this equilibrium, CPE is loosely called *electronic equilibrium*[4].

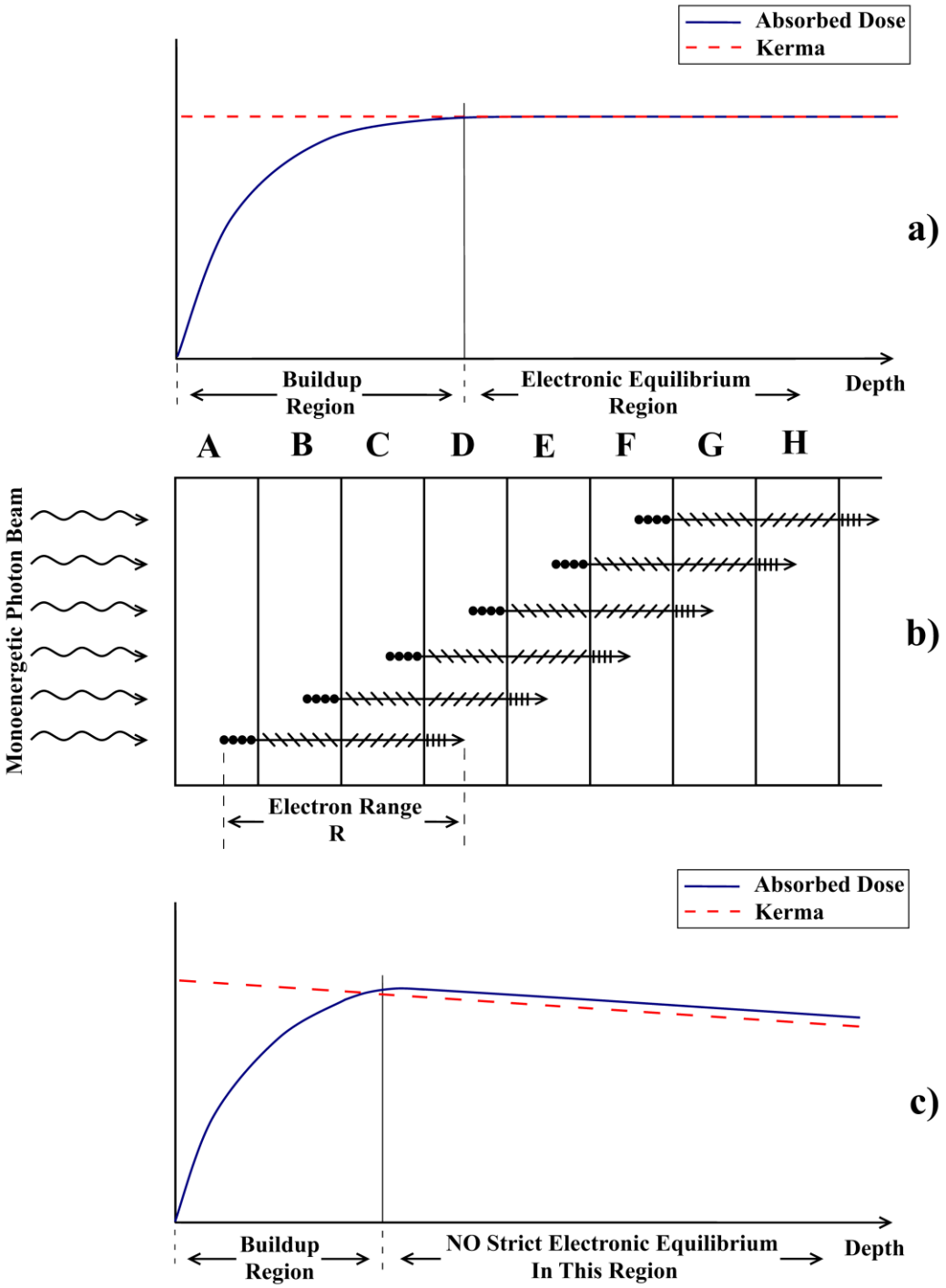

Figure 2.10 Schematic representation of two simplified theoretical scenarios showing the relationship between *absorbed dose* and *kerma*.

Figure 2.10 schematically shows a high energy, mono-energetic photon beam incident on a homogeneous phantom, divided into sections labeled A through H. The interacting photons

transfer energy to charged particles, and set electrons (straight arrows) in motion. Electrons will spend this energy through further excitations and ionizations (represented by the symbols *, \, /, and |) until they reach the end of their range R.

The idealized case where the primary photon beam is not attenuated, is schematically shown in Figure 2.10(a). In this simplified case, the same number of electrons is set in motion in each one of the regions A through H, and thus, the *kerma*, represented by the red dotted line, remains constant with increasing depth. The electrons set in motion in A, will deposit some of their energy (*) in the layer where they originated, but most of their energy is taken downstream. In region B, the same number of electrons is set in motion as in A. These new electrons will deposit some of their energy (*) in B, plus we have the electrons coming from A depositing part of their energy (\ )in B as well. Thus there will be more energy deposited in B than in A. In C, we have another batch of new electrons being set in motion and depositing some of their energy (*) in C before moving on, deeper within the phantom. We also have the electrons coming from B (\ ) and from A (/) depositing their energy. Thus the energy deposited in C is higher than the one deposited in B. In region D, the electrons that started in A come to the end of their range, and deposit the last of their energy (|). For the first time in this region we have all the types of energy deposition modes (*, \, /, and |). This means that this region has the highest energy deposited and that CPE has been reached, since the same amount of energy that leaves the volume also enters it from upstream. The region from the surface of the phantom all the way to the depth where *electronic equilibrium* is first established is called the *buildup region*, as shown in Figure 2.10. For the scenario in Figure 2.10 (a), past the *electronic equilibrium* point, the *dose* deposited is equal to the *kerma*, or more exactly to the collisional *kerma*[1,2]:

$$D \overset{CPE}{=} K_C \tag{2.14}$$

The slightly more realistic scenario, where the photon beam is attenuated by the medium is presented in Figure 2.10 (c). Since, as the beam interacts, there are going to be progressively less photons releasing their energy to the medium, the *kerma* will be constantly decreasing with increasing depth. If radiative losses are considered negligible, in the buildup region, the dose increase is similar to the no attenuation case, however, past the buildup region the dose will be constantly higher than the *collisional kerma*. This effect is due to the fact that, as noted in Section 2.3, *kerma* and *dose* are not deposited at the same spot. Thus, the kinetic energy released by the beam at a certain depth will always be lower than the dose deposited at that depth since the dose is due to more photons having already interacted upstream. This also means that, when beam attenuation is taken into account, at any given depth past the buildup region, there will be more electrons coming from upstream and depositing their energy than electrons leaving downstream and taking energy away. Thus CPE is no longer truly established past the buildup region, and instead, we have what is called a transient charged particle equilibrium (TCPE) where the *dose* is proportional to the *collisional kerma*[5].

$$D \overset{TCPE}{=} \beta \cdot K_C \;\; where \;\; \beta > 1 \tag{2.15}$$

When a depth dose curve, similar to the one shown in Figure 2.10, c) is normalized to the maximum dose value (D_{max}), it is called a *percent depth dose* curve, or simply a PDD.

2.6 Ionization Chambers and Cavity Theory

For accurate dose measurements in radiotherapy, the single most widely used dosimeter is the ionization chamber. The ionization chambers vary in shape, size, and design, but they all measure the charge liberated by a radiation beam inside an air cavity using an applied electric

field[2,5]. The measured charge can be directly related to absorbed dose to the medium via calibration and correction factors. The necessary correction factors were initially based on the Bragg-Gray cavity theory, and subsequently on Spencer-Attix cavity theory, both of which will be detailed below, after a brief description of the most common types of ionization chambers.

2.6.1 Cylindrical and Parallel Plate Ionization Chambers

The most common ion chambers have cylindrical (or spherical) air cavities as shown schematically in Figure 2.11(a). With typical gas volumes between 0.1 cm^3 to 3.0 cm^3 these types of chambers have a reasonably isotropic sensitivity to radiation. A high voltage, (±200 V - ±500 V) is applied to the chamber wall, and the collector, usually kept near ground potential, is connected to an electrometer. Some cylindrical ion chambers are fitted with a gas connector that allows gas (other than air) to fill the cavity and be continuously replenished, while other chambers are just vented to the atmosphere. If the cylindrical ion chamber is used to measure dose in photon or neutron beams, the ion chamber wall should be thick enough to ensure that any particles originating outside of the wall are kept out of the gas cavity. When using a cylindrical ion chamber to measure dose in a charged particle field, the chamber wall should be thin compared to the range of the incident charged particles[2].

Parallel plate ion chambers, schematically shown in Figure 2.11(b), have several advantages over cylindrical chambers. Very thin foils can be used to construct either just the top, or both flat chamber walls, resulting in minimal attenuation and scattering, while the gas layer can be made as thin as half a millimetre, resulting in an excellent spatial resolution in the direction perpendicular to the flat chamber walls. The increased resolution compared to cylindrical ion chambers makes parallel plate chambers ideal for measuring depth dose in the

buildup region. A guard electrode helps provide a uniform electric field, with the radius of the collecting volume defined by the collector radius, plus half the width of the insulating groove around it[2].

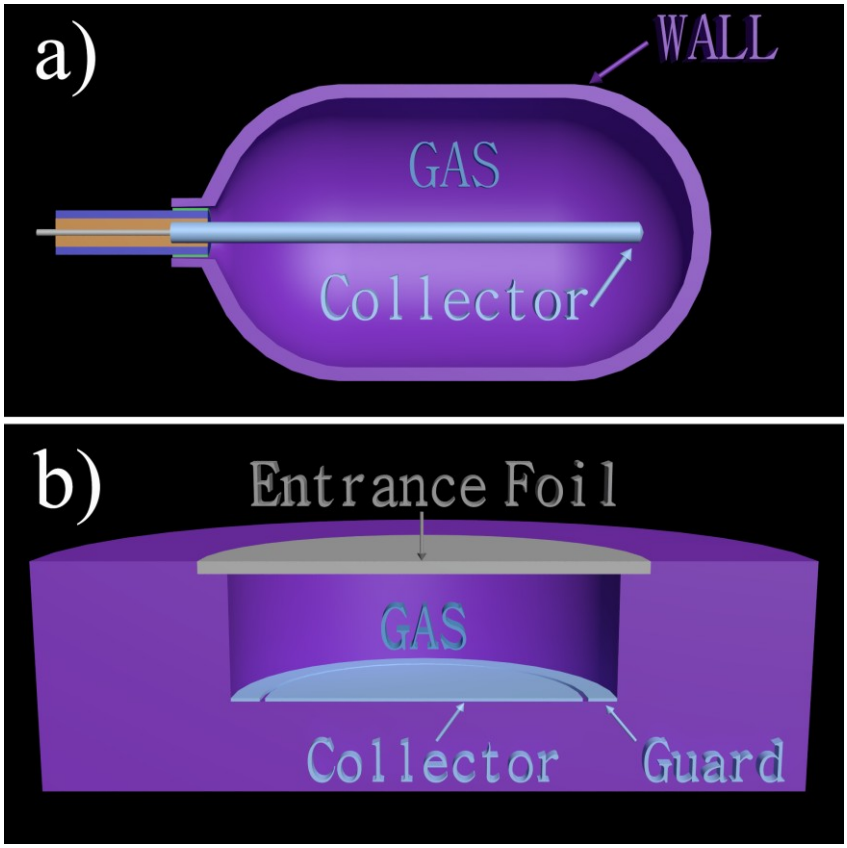

Figure 2.11 Simplified cross sectional representation of the main components present in a cylindrical (a), and parallel plate (b) ionization chamber.

Most commercial parallel plate chambers are designed with a thin entrance foil, but a thick back wall in which the collecting electrode and guard ring are embedded. When irradiated by high energy photons, electrons are knocked out of the back electrode. Replacement of knocked out electrons via electric circuit of the electrometer results in a current, known as the Compton Current. This current either adds or subtracts from the ionization current depending on the electric field direction through the air cavity. The Compton current is additive to ionization

current for the positively biased entrance foil and *vice versa*. This effect is known as the polarity effect, and it affects surface and buildup dose measurements, particularly when parallel plate ion chambers are used. The true ionization current is obtained by averaging two readings obtained with opposing polarities[2]. All the ion chamber measurements presented in this work use this method to remove the polarity effect and obtain the true ionization current.

Extrapolation chambers are parallel plate chambers designed with a variable thickness of the gas layer, by means of an adjustable screw. This type of chamber allows for the extrapolation of the measured ionization per unit gas thickness to zero thickness. An extrapolation chamber can accurately measure the surface dose in a phantom, and by adding thin sheets of material on top, the buildup dose can be measured as a function of depth[2].

2.6.2 Bragg-Gray Cavity Theory

The Bragg-Gray theory deals with small cavities, and relates the dose inside the cavity to the dose within the medium immediately surrounding the cavity. Assuming the medium inside the cavity is a gas in which the radiation produces a charge Q of either sign, the dose to the cavity material D_{gas} is:

$$D_{gas} = \frac{Q}{m}\left(\frac{\bar{W}}{e}\right)_{gas} \tag{2.16}$$

where m is the mass of the gas within the cavity, and $(\bar{W}/e)_{gas}$ represents the mean energy spent by the radiation to produce a unit of charge in the gas of the cavity. This mean energy per unit charge turns out to be fairly constant over a wide range of gas pressures and electron energies, and for dry air it has the value of $(\bar{W}/e)_{gas} = 33.97\ J/C$.

The Bragg-Gray cavity theory uses the following assumptions:

- the photon and electron fluence in the medium is not affected by the presence of the small cavity;
- the dose inside the cavity is due entirely to the electron fluence crossing the cavity (i.e. no secondary particles are created by photons inside the cavity itself);
- the electrons lose energy gradually as they traverse the cavity, in a series of interactions that only transfer small fractions of the electron's energy to the medium. This assumption is often referred to as the *continuous slowing down approximation* (CSDA);
- no bremsstrahlung interactions take place[1,2].

Under these conditions, the dose to the air cavity and the dose to the medium, are both being delivered by the same electron fluence. Assuming the electrons have a spectrum of energies from *0* to E_{max} the Bragg-Gray relation can be written as:

$$\frac{D_{med}}{D_{gas}} = \frac{\int_0^{E_{max}} \varphi_e(E) \cdot \left(\frac{S}{\rho}\right)_{med} dE}{\int_0^{E_{max}} \varphi_e(E) \cdot \left(\frac{S}{\rho}\right)_{gas} dE} \tag{2.17}$$

Where $\varphi_e = dN_e/da$ is the *electron fluence* through the cavity, and S/ρ is called the *mass collisional stopping power*. The mass collisional stopping power is defined as the expectation value of the rate of energy loss of a particle with kinetic energy E per unit path length per unit density, in a medium of atomic number Z.

$$\left(\frac{S}{\rho}\right) = \frac{1}{\rho}\frac{dE}{dl} \tag{2.18}$$

The average mass collisional stopping power is defined as:

$$\left(\frac{\bar{S}}{\rho}\right) = \frac{\int_0^{E_{max}} \varphi_e(E) \cdot \left(\frac{S}{\rho}\right) dE}{\int_0^{E_{max}} \varphi_e(E) dE} \tag{2.19}$$

So we can now write the Bragg-Gray relationship as:

$$\frac{D_{med}}{D_{gas}} = \frac{\left(\frac{\bar{S}}{\rho}\right)_{med}}{\left(\frac{\bar{S}}{\rho}\right)_{gas}} = \left(\frac{\bar{S}}{\rho}\right)_{gas}^{med} \tag{2.20}$$

And substituting D_{gas} from Eq. (2.16) we have:

$$D_{med} = \frac{Q}{m}\left(\frac{\bar{W}}{e}\right)_{gas} \cdot \left(\frac{\bar{S}}{\rho}\right)_{gas}^{med} \tag{2.21}$$

Using this equation, one is able to calculate the dose to the medium provided the values of $m, (\bar{W}/e)_{gas}, and\ (\bar{S}/\rho)_{gas}^{med}$ are all known. Typically, for uncharged particle measurements, the medium surrounding the air cavity of an ionization chamber is the solid ion chamber wall. Since the wall has to be thick enough to ensure that the electrons traversing the cavity must have originated within the wall, the Bragg-Gray relationship is also said to relate the dose in the gas cavity to the dose in the wall of an ion chamber[1,2,5].

One of the drawbacks of the Bragg-Gray cavity theory is that it assumes electrons can only lose energy according to the CSDA and ignores the creation of δ-rays. δ-rays are energetic electrons produced through knock on electron-electron collisions (hard collisions) in which up to half the energy of the primary electron can be transferred. Ignoring δ-rays causes Bragg-Gray to incorrectly predict the ionization in air-filled cavities for high energy beams.

2.6.3 Spencer-Attix Cavity Theory

The Spencer-Attix cavity theory expands the Bragg-Gary theory to account for the effects of δ-rays. This was achieved by introducing the *restricted mass collisional stopping power* (L/ρ). δ-rays are capable of taking their energy far enough away from the point where the

interaction takes place which leads to overestimates in dose calculations using the *unrestricted mass collisional stopping power* for higher electron energies. The restricted stopping power accounts for all the soft collisions, and a few of the hard collisions that produce δ-rays with energies below a certain cutoff value Δ. Within the Spencer-Attix formalism, Δ was defined as the mean electron energy of an electron that can just barely cross the air cavity. Electrons with energy above Δ can transport energy further downstream, while electrons with energy below Δ are assumed to have zero range and their energy is considered to be deposited locally. Thus, the restricted mass collisional stopping power can be written as:

$$\left(\frac{L}{\rho}\right) = \frac{1}{\rho}\frac{dE_{\Delta}}{dl} \tag{2.22}$$

Where dE_{Δ} is simply the energy lost by a charged particle by soft collisions and all the hard collisions producing δ-rays with energy below Δ. The average restricted mass collisional stopping power can be then defined similar to Eq. (2.19):

$$\left(\frac{\bar{L}}{\rho}\right) = \frac{\int_{\Delta}^{E_{max}} \varphi(E) \cdot \left(\frac{L}{\rho}\right) dE}{\int_{\Delta}^{E_{max}} \varphi(E) dE} \tag{2.23}$$

where the lower integration limit is Δ, since by definition, δ-rays with energy below Δ have zero range (deposit their dose at the point of creation) and are not part of the equilibrium electron spectrum $\varphi(E)$. Thus, the Spencer-Attix relationship relating the dose inside the air cavity to the dose in the medium surrounding the cavity is:

$$\frac{D_{med}}{D_{gas}} = \frac{\int_{\Delta}^{E_{max}} \varphi_e(E) \cdot \left(\frac{L}{\rho}\right)_{med} dE}{\int_{\Delta}^{E_{max}} \varphi_e(E) \cdot \left(\frac{L}{\rho}\right)_{gas} dE} \tag{2.24}$$

Finally the Spencer-Attix dose to the medium surrounding an air cavity can be shown to be:

$$D_{med} = \frac{Q}{m}\left(\frac{\bar{W}}{e}\right)_{gas} \cdot \left(\frac{\bar{L}}{\rho}\right)_{gas}^{med} \tag{2.25}$$

One thing to note is that the above equations for both the Bragg-Gray and the Spencer-Attix theory assume a monoenergetic source of electrons. The averages for both the unrestricted and the restricted mass collisional stopping power are taken over the spectrum of electron energies that arise from the initially monoenergetic electrons traversing the medium and interacting. A second averaging could be done if the source is a monoenergetic beam of photons setting a spectrum of electrons in motion. Finally, a third average will have to be taken over the spectrum of photons if the photon beam is not monoenergetic.

By taking the δ-ray production into account, and relating the dose integral to the cavity size, the Spencer-Attix cavity theory agrees with experimental observations better than the Bragg-Gray theory for small cavities[1,2,5].

2.7 Radiochromic Film Dosimetry

Radiochromic films are able to measure depth dose or isodose curves in high dose gradient regions, while overcoming some of the limitations of radiographic film. Some of the general features of radiochromic film are: very high spatial resolution, low spectral sensitivity, insensitivity to room light, and image formation through self-development. The image is formed through a process of polymerization, as the energy transferred from an energetic photon or particle initiates chemical changes that result in color formation in the leuco dye or colourless photomonomer molecule[6].

GafChromic film is a type of radiochromic film designed for use within the radiotherapy environment for dose measurements in brachytherapy, radiosurgery, and external beam

radiotherapy. The newest type of general purpose GafChromic film is the EBT3. Nearly tissue equivalent and water resistant EBT3 film has low energy dependence and a special coating to stop Newton Rings from forming when scanned using a flatbed scanner. The symmetrical structure of the EBT3 films (see Figure 2.12) means that the film can be scanned on either side (unlike previous versions of the EBT films). The yellow dye incorporated in the active layer allows for multi-channel dosimetry while at the same time decreasing the sensitivity to ultraviolet light.

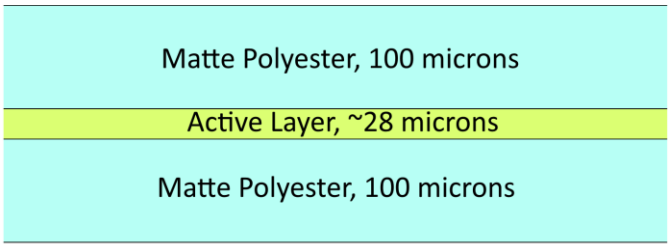

Figure 2.12 Cross section, showing the GafChromic EBT3 dosimetry film configuration.

A multichannel scanner is useful in offering a selection between the red channel, for low dose sensitivity, and the green or blue channel, both of which can be used to extend the film's dynamic range to higher doses. Methods have also been developed[7] in which the data acquired from all the color channels is used to separate the dose dependent information from the dose independent information. The dose independent information is caused by a combination of thickness variations in the film's active layer, as well as variations in the response of the flatbed scanner which can cause increasing film density values as the distance from the central scan axis increases. Thus, in addition to the single-channel method (using the red channel) of converting film density to dose, there are the dual-channel method (using the red and the blue channel), and

the triple-channel method (using all the red, green, and blue channels). The dual-channel method makes use of the blue channel to account for the thickness variations of the active layer, while the triple-channel method also uses the information in the green channel to separate any other dose independent disturbances present in the system. The reader is encouraged to refer to Micke *et al* for a full theoretical derivation of each of these film dosimetry methods[7].

GafChromic film is easy to use for quickly measuring high resolution 2D dose distributions. However when measuring absolute dose the typical uncertainty for GafChromic film is between 2% to 5%[8,9]. For sub percent uncertainties, ion chambers are still the instruments of choice.

2.8 Overview of Electromagnetism

As the current work deals with dose deposited in the presence of strong electromagnetic fields, a brief discussion on electromagnetism is needed. The current chapter introduces some basic concepts, as well as Maxwell's equations. For full derivations and a more detailed discussion of electrostatics and electrodynamics the reader is encouraged to consult either Griffiths[10] or Jackson[11], the two main references used for this chapter.

Electrostatics virtually started with Coulomb's quantitative statement describing the force between charged bodies that are at rest with respect to each other. Coulomb showed experimentally that the force on a test charge *Q,* due to another charge *q* located a distance *r* away is given by:

$$\vec{F} = \frac{1}{4\pi\varepsilon_0}\frac{Qq}{r^2}\hat{r} \tag{2.26}$$

where ε_0 is the permitivity of free space ($\varepsilon_0 = 8.85 \times 10^{-12}\ C^2/(N\ m^2)$), and $\hat{r}$ is simply the direction unit vector for r. A useful concept to introduce at this point is that of an electric field (E) that can be defined as the force per unit charge ($\vec{F} = Q\vec{E}$). Thus, a stationary point charge will produce an electric field around it defined by:

$$\vec{E}(\vec{r}) = \frac{1}{4\pi\varepsilon_0}\frac{q}{r^2}\hat{r} \tag{2.27}$$

where q is the electric charge that produces the field E, and r is the distance from that charge to the point of interest. More generally, if the charge q is distributed continuously over some region of space the electric field is:

$$\vec{E}(\vec{r}) = \frac{1}{4\pi\varepsilon_0}\int \frac{1}{r^2}\hat{r}dq \tag{2.28}$$

Furthermore, if the charge is uniformly distributed in a volume with charge per unit volume ρ then $dq = \rho\, dV$ (where dV is an infinitesimal volume element), and (2.28) above becomes

$$\vec{E}(\vec{r}) = \frac{1}{4\pi\varepsilon_0}\int_{\mathcal{V}} \frac{\rho(\overrightarrow{r})}{r^2}\hat{r}\, dV \tag{2.29}$$

The electric field permeates space in every direction with field lines starting on a positive charge and ending on a negative one. As a measure of the number of field lines passing through a surface $\mathcal{S}$ we can define the *electric flux* as:

$$\Phi_E = \int_{\mathcal{S}} \vec{E}\cdot d\vec{a} \tag{2.30}$$

By combining Eq. (2.28) and Eq. (2.30) we can calculate the electric flux through a sphere enclosing a point charge to be:

$$\oint_S \vec{E} \cdot d\vec{a} = \iiint \frac{1}{4\pi\varepsilon_0}\left(\frac{q}{r^2}\hat{r}\right) \cdot (r^2 \sin\theta \, d\theta \, d\phi \hat{r}) = \frac{1}{\varepsilon_0} q \tag{2.31}$$

The formula for the point charge can easily be generalized for a random charge distribution:

$$\boxed{\oint_S \vec{E} \cdot d\vec{a} = \frac{1}{\varepsilon_0} Q_{enc}} \tag{2.32}$$

with Q_{enc} being the total charge enclosed within the closed surface. Eq. (2.32) is known as *Gauss's Law* which states that the electric flux over a closed surface is proportional to the total charge enclosed within that surface[10,11].

Gauss's Law can be converted from its integral form to a differential form by using the divergence theorem, which states that the integral over a closed surface $\mathcal{S}$ of a vector field is equal to the integral of the divergence of that vector field over the volume enclosed by $\mathcal{S}$. Thus, for our electric field we have:

$$\oint_S \vec{E} \cdot d\vec{a} = \int_V \vec{\nabla} \cdot \vec{E} \, dV \tag{2.33}$$

If Q_{enc} is written as the volume integral of the charge density ρ, we have the final differential form of *Gauss's Law*:

$$\boxed{\vec{\nabla} \cdot \vec{E} = \frac{1}{\varepsilon_0} \rho} \tag{2.34}$$

In addition to generating an electric field *E*, like a stationary charge, a moving charge will also generate a magnetic field *B* in the space around it. This was first discovered when it was noticed that a compass needle could be deflected by a current carrying wire, thus establishing a link between electricity and magnetism[11].

A charge Q moving in a magnetic field $\vec{B}$ with velocity $\vec{v}$ will experience a magnetic force given by the *Lorentz force law*:

$$\vec{F}_{mag} = Q(\vec{v} \times \vec{B}) \tag{2.35}$$

When both magnetic and electric fields are present the total force on the moving charge *Q* will be:

$$\vec{F} = Q\left[\vec{E} + \left(\vec{v} \times \vec{B}\right)\right] \tag{2.36}$$

The magnetic field produced by a steady line current is given by the Biot-Savart law:

$$\vec{B}(\vec{r}) = \frac{\mu_0}{4\pi}\int \frac{\vec{I} \times \hat{r}}{r^2} dl = \frac{\mu_0 I}{4\pi}\int \frac{d\vec{l} \times \hat{r}}{r^2} \tag{2.37}$$

Where *B* is the magnetic field measured in Tesla (T), *I* is the magnitude of the steady current, *dl* is an element of length along the current carrying wire, *r* is the distance between the length element *dl* and the point of interest, and $\hat{r}$ is the unit vector pointing from *dl* towards the point of interest. The constant μ_0 is called the *permeability of free space* and has a value of $\mu_0 = 4\pi \times 10^{-7} N/A^2$. For the more general case where we have a volume current density *J*, the Biot-Savart law becomes:

$$\vec{B}(\vec{r}) = \frac{\mu_0}{4\pi}\iiint \frac{\vec{J}(\vec{r}) \times \hat{r}}{r^2} dV \tag{2.38}$$

Where the integration is now over the volume (*dV*) containing the current density *J*. Calculating the divergence of *B* we get:

$$\vec{\nabla} \cdot \vec{B} = \frac{\mu_0}{4\pi}\iiint \vec{\nabla} \cdot \left(\frac{\vec{J} \times \hat{r}}{r^2}\right) dV \tag{2.39}$$

Applying vector product rules to expand the integrand and noting that both $\vec{\nabla} \times \vec{J} = 0$ and $\vec{\nabla} \times (\hat{\mathrm{r}}/\mathrm{r}^2) = 0$, the divergence of *B* can be shown to be:

$$\boxed{\vec{\nabla} \cdot \vec{B} = 0} \tag{2.40}$$

Applying the curl to Eq. (2.38) we have:

$$\vec{\nabla} \times \vec{B} = \frac{\mu_0}{4\pi} \iiint \vec{\nabla} \times \left(\frac{\vec{J} \times \hat{r}}{r^2} \right) dV \tag{2.41}$$

Yet again, using vector product rules to expand the integrand, noting that the derivatives of J go to zero, and finally calculating the divergence $\nabla \cdot (\hat{r}/r^2) = 4\pi\delta^3(\vec{r})$, with δ^3 representing the three dimensional delta-function, it can be shown that:

$$\boxed{\vec{\nabla} \times \vec{B} = \mu_0 \vec{J}(\vec{r})} \tag{2.42}$$

Equation (2.42) is known as *Ampere's law*. To convert Ampere's law to integral form we have to apply Stoke's theorem which states that the integral of the curl of a vector field over a surface is equal to the line integral of the vector field over the closed loop that represents the boundary of that surface. Thus:

$$\iint (\vec{\nabla} \times \vec{B}) \cdot d\vec{a} = \oint \vec{B} \cdot d\vec{l} = \mu_0 \iint \vec{J} \cdot d\vec{a} = \mu_0 I_{enc}$$

$$\boxed{\oint \vec{B} \cdot d\vec{l} = \mu_0 I_{enc}} \tag{2.43}$$

with I_{enc} being the total current enclosed in the amperian loop.

The highlighted equations above are part of a set, better known as the *Maxwell equations*. As written in Eq. (2.42), Ampere's law is not strictly true beyond magnetostatics. Maxwell realized this, since the divergence of the curl should always be zero, while when taking the divergence of Eq. (2.42) the left hand side does not necessarily go to zero. Maxwell fixed this problem by adding a time dependent term to *Ampere's law*.

The corrected *Ampere's law*, as well as *Faraday's law* which states that a changing magnetic field induces an electric field, complete the Maxwell equations set. Thus, rewriting some of the previous equations for completeness purposes, Maxwell's equations in differential form are:

$$\vec{\nabla} \cdot \vec{E} = \frac{1}{\varepsilon_0}\rho \qquad (Gauss's\ Law) \tag{2.44}$$

$$\vec{\nabla} \cdot \vec{B} = 0 \qquad (No\ Name) \tag{2.45}$$

$$\vec{\nabla} \times \vec{E} = -\frac{\partial \vec{B}}{\partial t} \qquad (Faraday's\ Law) \tag{2.46}$$

$$\vec{\nabla} \times \vec{B} = \mu_0 \vec{J} + \mu_0 \epsilon_0 \frac{\partial \vec{E}}{\partial t} \quad (Ampere's\ Law) \tag{2.47}$$

Using vector product rules one can easily write Maxwell's equations in either integral or differential form, as shown above for Gauss's law and Ampere's law. As the current work uses electric and magnetic fields that are constant over time, a more thorough derivation of Faraday's law will be omitted. Full derivations for all of Maxwell's equations can be found in either of the references used for this chapter[10,11].

2.9 Introduction to Monte Carlo

Monte Carlo is a computational technique that makes use of random numbers to solve various complex problems[12]. One of the earliest scientists to make use of random numbers to solve an integral was the French naturalist Georges-Louis Leclerc, comte de Buffon in 1777[13]. The experiment he described (now referred to as Buffon's needle) involved randomly throwing a needle of length L onto a horizontal plane ruled with straight parallel lines a distance d apart (where $d > L$), and calculating the probability P that the needle will intersect one of these lines. As the probability turns out to be $P=2L/\pi d$, Laplace suggested, over a hundred years later, that

this needle throwing method could be used to evaluate π.[14] The development of the technique in its current form as well as the application of the name "Monte Carlo" to this class of mathematical methods is attributed to the work done by John von Neumann, Stanislaw Ulam, and Enrico Fermi while developing nuclear weapons in Los Alamos in the 1940s[14-16].

One of the drawbacks of the Monte Carlo method is that the answers obtained are statistical in nature and thus subject to the laws of chance. However, the accuracy of an answer can be determined and, if needed, a more accurate answer can be obtained by simply running more Monte Carlo experiments[14].

For a better understanding of Monte Carlo a brief overview of elementary probability theory will be presented next, followed by an introduction to EGSnrc Monte Carlo, and ending with the theory behind implementing electromagnetic fields in the EGSnrc code.

2.9.1 Elementary Probability Theory

A *random variable* is any quantity that requires probability laws in order to be properly specified[16]. Thus, the actual values (or realizations) of a random variable cannot be predicted exactly[15]. If a random variable *x* can only take a number of distinct values it is said to have a discrete distribution. If the random variable can take *any* value between certain limits then it is said to have a continuous distribution[16].

The probability that the random number *x* will be obtained in a differential interval *dx* about a specific value x_1 can be written as:

$$P\{x|x_1 < x < x_1 + dx\} = p(x_1)dx \tag{2.48}$$

where $p(x)$ is referred to as the *probability density function* (or PDF) of *x*. The PDF must be positive (since negative probabilities don't have meaning), and normalized to unity:

$$p(x) \geq 0 \quad \text{and} \quad \int_{x_{min}}^{x_{max}} p(x)dx = 1 \tag{2.49}$$

The *cumulative distribution function* (CDF) of *x* for a continuous random variable is defined by:

$$\mathcal{P}(x) \equiv \int_{x_{min}}^{x} p(x')dx' \tag{2.50}$$

$\mathcal{P}(x)$ is a monotonically increasing function that takes values in between $\mathcal{P}(x_{min}) = 0$ and $\mathcal{P}(x_{max}) = 1$. The probability of *x* being in the interval *(a, b)* can now be written as:

$$P\{x|a < x < b\} = \int_{a}^{b} p(x)dx = \mathcal{P}(b) - \mathcal{P}(a) \tag{2.51}$$

Thus the probability density function *p(x)* is simply the derivative of the CDF: $p(x) = d\mathcal{P}(x)/dx$.

The *n*-th moment of *p(x)* is by definition:

$$\langle x^n \rangle \equiv \int_{x_{min}}^{x_{max}} x^n \, p(x)dx \tag{2.52}$$

The 0th moment, $\langle x^0 \rangle$ is simply the PDF integral and is by definition equal to unity (see Eq. (2.49)). The 1st moment, $\langle x^1 \rangle$ is also called the mean, or expectation value, of the random variable *x*.

$$\langle x \rangle = \int x \, p(x)dx \tag{2.53}$$

If the 1st and 2nd moments of *p(x)* exist, the variance of *x* can be defined as:

$$var(x) \equiv \langle (x - \langle x \rangle)^2 \rangle = \int (x - \langle x \rangle)^2 p(x) dx = \langle x^2 \rangle - \langle x \rangle^2 \tag{2.54}$$

The *standard deviation* is simply the square root of the variance:

$$\sigma \equiv \sqrt{var(x)} \tag{2.55}$$

and it represents a measure of the width of the PDF, or the spread of the values of the random variable.

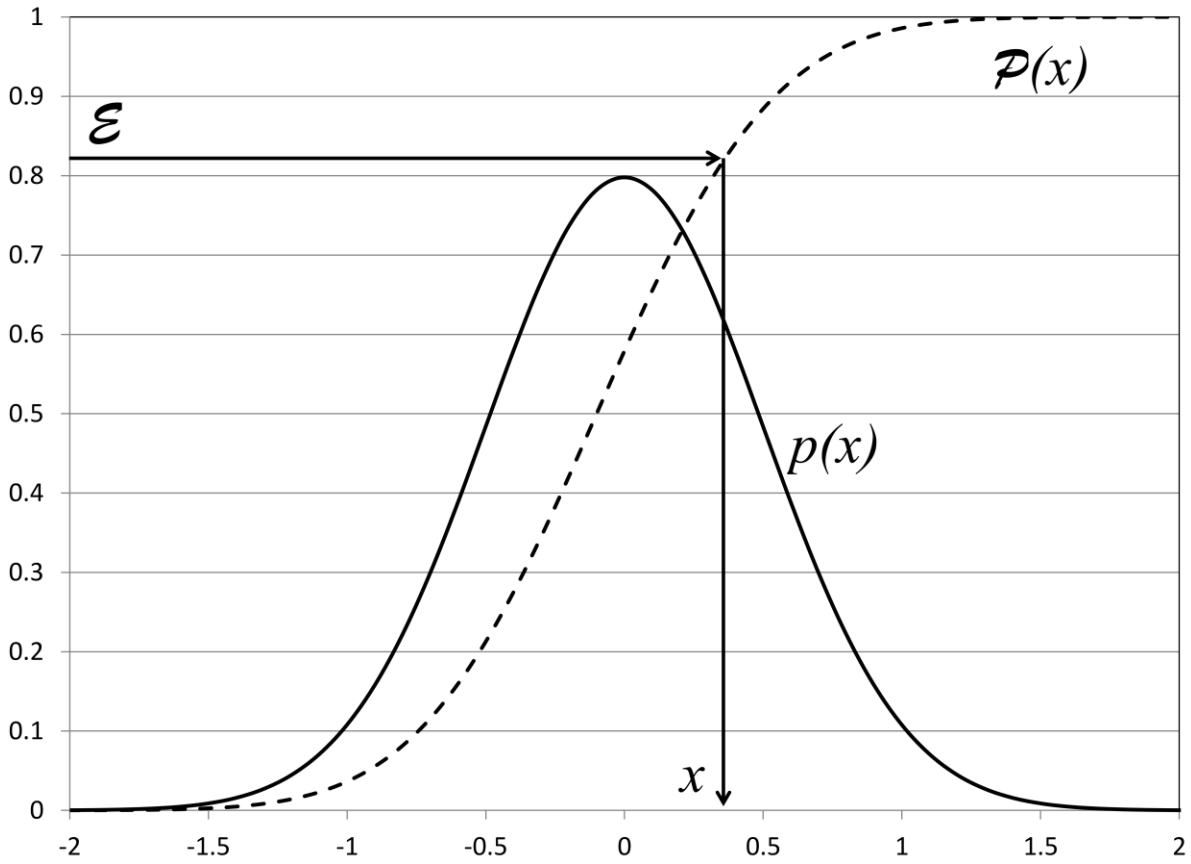

Figure 2.13 Illustration of the inverse transform method: using uniformly distributed random numbers **ε** to generate random numbers $x = \mathcal{P}^{-1}(\mathcal{E})$ with a probability density function $p(x)$.

Since the CDF, $\mathcal{P}(x)$, is a continuous monotonically increasing function, it will have an inverse function $\mathcal{P}^{-1}(\mathcal{E})$. This means that:

$$x = \mathcal{P}^{-1}(\mathcal{E}) \text{ and } \mathcal{E} = \mathcal{P}(x) \tag{2.56}$$

As long as *x* is a random number distributed in the interval (x_{min}, x_{max}) with *PDF = p(x)*, then $\boldsymbol{\mathcal{E}}$ will also be a random number in the interval (*0, 1*). This also means that if we are starting with a series of random numbers $\boldsymbol{\mathcal{E}_1, \mathcal{E}_2, \ldots}$, uniformly distributed in the interval (0, 1), we can generate another series of random numbers $x_1, x_2, \ldots$, that will be distributed in the (x_{min}, x_{max}) interval according to *p(x)*. This particular procedure for random sampling is called the *inverse transform method* and is schematically represented in Figure 2.13 above[15,16].

The sampling equation for the random variable *x,* for which *x* is the unique root, is given below:

$$\mathcal{E} = \int_{x_{min}}^{x} p(x')dx' \tag{2.57}$$

The inverse transform method can be used for either analytical distributions or for continuous distributions available in numerical form[15,16].

Another random sampling method is called *rejection sampling*. This method can be easily employed when exact computation of *p(x)* is straightforward, or when computing $\mathcal{P}^{-1}$ is particularly complicated mathematically. Given a PDF *p(x)* defined on the interval *[a, b]*, to implement the rejection sampling method, first the distribution function is scaled by its maximum value, thus obtaining the function $p(x)/p(x_{max})$. Two uniformly distributed random numbers, r_1 *and* r_2, have to be generated. Then our random number coordinates (X, Y) will be generated as follows: $X = a + (b - a) * r_1$ and $Y = r_2$. If $r_2 \leq p(X)/p(x_{max})$ then the randomly generated point is below the distribution curve in the region of acceptance and is considered accepted, otherwise it is rejected. The scaled PDF as well as the regions of acceptance and rejection (shaded) are shown below in Figure 2.14.

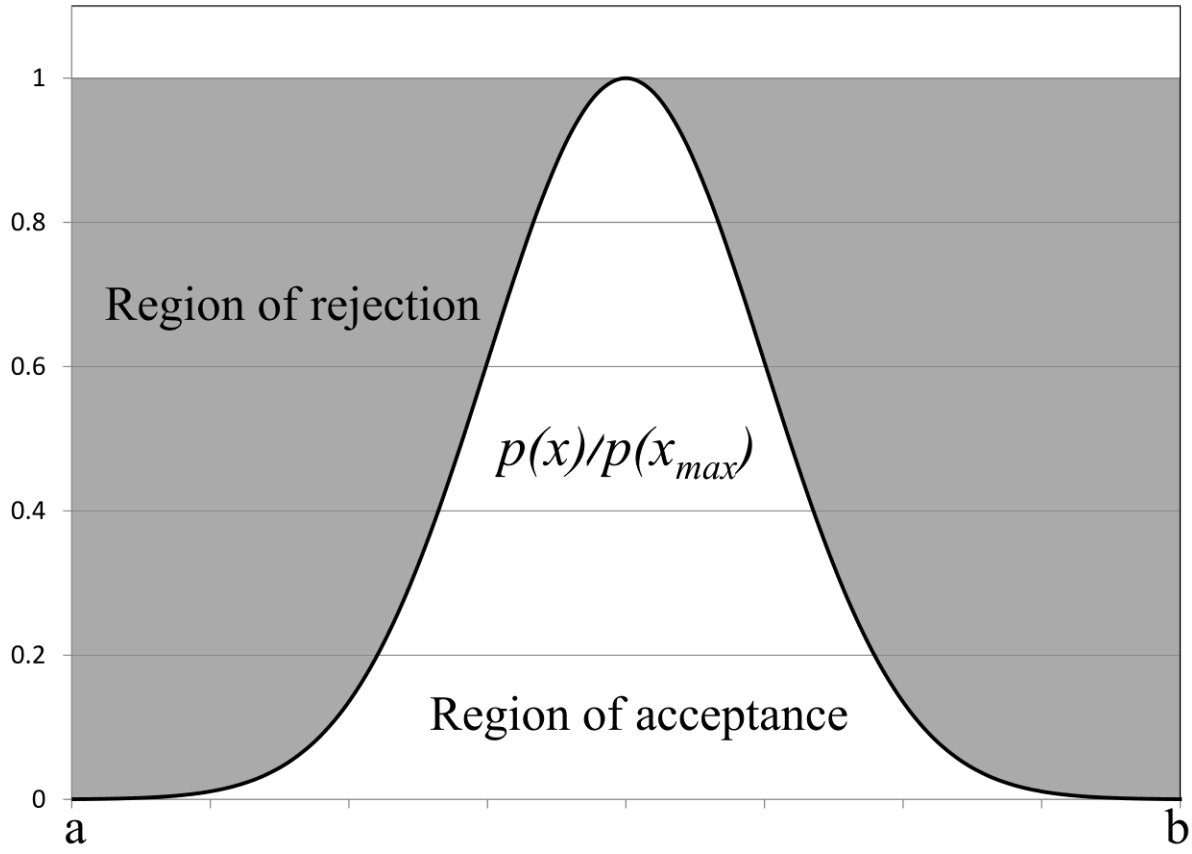

Figure 2.14 An illustration of the rejection sampling method. If the point generated is below the curve it will be accepted, otherwise it will be rejected.

2.9.2 EGSnrc Monte Carlo

The Electron Gamma Shower (or EGS) Monte Carlo system is a general purpose package for simulating the coupled transport of photons and electrons in an arbitrary geometry. Photons and electrons (as well as positrons) with energies between a few keV and several hundred GeV can be simulated in any element, compound or mixture. The cross sectional data is generated by the PEGS4 companion code using tables of the cross section for elements (Z = 1 through 100). In most situations the PEGS4 code only needs to be run once, with the generated cross section data being useable for all the subsequent Monte Carlo simulations[17].

The physical reality of particle transport is simulated faithfully using Monte Carlo. Using pseudo-random numbers, distributions describing the particle source are sampled and particles are 'born'. The total interaction cross section is then sampled to determine the distance of travel to the next interaction site. This distance is also known as the step size. The particles leave the interaction site after deciding their energy and angle by sampling the appropriate cross sections. New particles may also be produced at the interaction site, and these new particles are added to the particle stack and subsequently transported. This process is repeated over and over, until all the particles spend all their energy and are absorbed or until they leave the volume of interest[17]. Since photons undergo a relatively small number of interactions, before they either leave the geometry of interest or get absorbed, their interactions can be simulated in an analogue fashion that directly imitates the physical reality[18].

On the other hand, a fast electron and the particles it creates typically undergo hundreds of thousands of interactions before their energy is spent. Since an analogue, event by event, simulation for charged particles is impractical in terms of the time and computing power requirements, EGSnrc employs the *condensed history technique*. The condensed history technique, first developed by Martin Berger, "condenses" a large number of transport and collision processes into one single "step". The changes in the charged particle's energy, direction of motion, and position, are sampled from appropriate inelastic and multiple scattering distributions that take into account the cumulative effect of the individual interactions. The use of the condensed history technique is justified by the fact that most charged particle interactions only result in small changes in the particle's energy and direction. However this technique also introduces a dependence of the calculated result on an artificial parameter, namely the step

length, which has become known as a step size artefact[18]. The condensed history method, has been shown to converge to the correct result in the limit of a small step size[19].

In the condensed history algorithm used by EGSnrc, 'catastrophic' electron collisions (i.e. bremsstrahlung photons with energies greater than *AP*, and δ-rays with energies above *TE = AE - 0.511 MeV*) are simulated explicitly. Sub threshold energy losses are grouped together and the particles loose energy according to CSDA. AP and AE are two user defined parameters used to set this threshold for radiative losses and discrete collisions respectively[17]. The variable TE is the Δ of the restricted stopping power discussed in Section 2.6.3.

2.9.3 Electron transport in electromagnetic fields

In this section the theory, developed by A. Bielajew, of implementing electromagnetic fields in EGSnrc is explored. An electron moving in vacuum experiences a force due to an electromagnetic field according to Eq.(2.36). For the electron charge *e* that equation can be rewritten as:

$$\frac{d\vec{p}}{dt} = e\left(\vec{E} + \vec{v} \times \vec{B}\right) \tag{2.58}$$

where $\vec{p}$ is the momentum of the electron and *t* is time. By making the relativistic substitutions

$\vec{\beta} = v/c$, where *c* is the speed of light, $\gamma = \left(1 - \vec{\beta} \cdot \vec{\beta}\right)^{-1/2}$, expressing the time *dt* in terms of *ds* (the differential path length) so that $ds = (ds/dt) \cdot dt = (c\beta)dt$, and expressing the momentum as $\vec{p} = m\vec{v} = \gamma m_0 c\vec{\beta}$ we can rewrite equation (2.58) as:

$$\frac{d(\gamma\vec{\beta})}{ds} = \frac{e}{m_0 c^2 \beta}\left(\vec{E} + c\vec{\beta} \times \vec{B}\right) \tag{2.59}$$

The left hand side of Eq. (2.59) can be expanded as $d(\gamma\vec{\beta}) = \gamma d\vec{\beta} + \vec{\beta}d\gamma$ and writing out the derivative of γ with respect to β as $d\gamma = \gamma^3(\vec{\beta}\cdot d\vec{\beta})$ we now have:

$$\frac{\gamma d\vec{\beta}}{ds} + \frac{\gamma^3\vec{\beta}(\vec{\beta}\cdot d\vec{\beta})}{ds} = \frac{e}{m_0c^2\beta}(\vec{E} + c\vec{\beta}\times\vec{B}) \tag{2.60}$$

If we take the dot product of both sides of Eq. (2.60) with $\vec{\beta}$, the magnetic field term on the right hand side goes to zero (dot product of a cross product is always zero). On the left hand side we can factor out $\gamma^3\vec{\beta}\cdot d\vec{\beta}/ds$ which gives us:

$$\frac{\gamma^3\vec{\beta}\cdot d\vec{\beta}}{ds} = \frac{e}{m_0c^2\beta}(\vec{E}\cdot\vec{\beta}) \tag{2.61}$$

Eq. (2.61) can be substituted in Eq. (2.60) and after rearranging we obtain:

$$\frac{d\vec{\beta}}{ds} = \frac{e}{m_0c^2\beta\gamma}\left[\vec{E} - \vec{\beta}(\vec{E}\cdot\vec{\beta}) + c\vec{\beta}\times\vec{B}\right] \tag{2.62}$$

Writing this equation in terms of the unit direction vector of the charged particle, $\vec{u} = \vec{\beta}/\beta$, results in:

$$\frac{d\vec{u}}{ds} = \frac{e}{m_0c^2\beta^2\gamma}\left[\vec{E} - \beta^2\vec{u}(\vec{E}\cdot\vec{u}) + c\beta\vec{u}\times\vec{B}\right] \tag{2.63}$$

The EGSnrc implementation of electro-magnetic fields makes use of the above two equations: (2.62) and (2.63).[20]

2.9.4 Transport in a medium in the presence of E and B fields

Although the transport of charged particles in a medium in the presence of electromagnetic fields can be quite difficult to work out theoretically, it can still be simulated by using certain approximations. As a charged particle moves through a medium it will couple to the external electromagnetic fields. In addition, the particle will undergo inelastic and elastic

(multiple scattering) interactions. If the medium through which the particle is traveling is assumed to be isotropic and homogeneous, the equation of motion can be written as:

$$\frac{d\vec{p}}{dt} = \vec{F}_{ret}\big(E(t)\big) + \vec{F}_{ms}\big(E(t)\big) + \vec{F}_{em}(\vec{x}(t), E(t), \vec{u}(t)) \tag{2.64}$$

where $\vec{F}_{ret}$ is the force felt by the charged particle due to inelastic (retarding) interactions, $\vec{F}_{ms}$ is the force due to elastic (or multiple scattering) interactions, and $\vec{F}_{em}$ is the force due to external electromagnetic fields. If we integrate Eq. (2.64) we obtain

$$\vec{v} = \vec{v}_0 + \frac{1}{m_0\gamma(E)}\int_0^t \left[\vec{F}_{ret}\big(E(t')\big) + \vec{F}_{ms}\big(E(t')\big) + \vec{F}_{em}(\vec{x}(t'), E(t'), \vec{u}(t'))\right] dt' \tag{2.65}$$

$$\vec{x} = \vec{x}_0 + \vec{v}_0 t + \int_0^t \vec{v}(t")\, dt" \tag{2.66}$$

The interplay among the various constituents of (2.65) and (2.66) make these equations very difficult to solve directly. The inelastic processes ($\vec{F}_{ret}$), like electron-electron interactions and creation of bremsstrahlung photons, affect the energy *E* of the particle and consequently the magnitude of the velocity *v*. The fact that $\vec{F}_{ms}$ and $\vec{F}_{em}$ also depend on energy causes them to be coupled to $\vec{F}_{ret}$. Most elastic processes ($\vec{F}_{ms}$) consist of deflections caused by the nuclei present in the medium. While the energy lost to the recoiling nucleus is small and can usually be ignored, $\vec{F}_{ms}$ does cause changes in the direction of the velocity, and thus couples to $\vec{F}_{em}$ since $\vec{F}_{em}$ depends on the direction vector ($\vec{u}$) of the charged particle. $\vec{F}_{em}$ itself can alter both the magnitude and direction of the velocity, thus coupling to both $\vec{F}_{ret}$ and $\vec{F}_{ms}$. Also, we must not forget about the gamma factor in front of the integral in Eq. (2.65) that also depends on energy, since when the energy changes the mass of the charged particle also changes. A further complication, when using a condensed history Monte Carlo like EGSnrc, is that the exact

trajectories of the charged particles are not known, nor are the exact forms of $\vec{F}_{ret}$, and $\vec{F}_{ms}$. However, the already existing statistical treatments of $\vec{F}_{ret}$ (Bethe-Bloch slowing down theory[21-23]), and of $\vec{F}_{ms}$ (Molière multiple-scattering theory[24,25]) can be used.

If for the different possible charged particle trajectories the external electromagnetic fields are different, the problem is impossible to solve. Thus a first approximation would be to demand that the particle step size be small enough so that over the course of a particle step *the electromagnetic fields do not change much*. With this approximation Eq. (2.65) can be rewritten as follows:

$$\vec{v} = \vec{v}_0 + \frac{1}{m_0\gamma(E)}\int_0^t \left[\langle\vec{F}_{ret}\big(E(t')\big)\rangle + \langle\vec{F}_{ms}\big(E(t')\big)\rangle + \vec{F}_{em}(\vec{x}_0, E(t'), \vec{u}(t'))\right] dt' \qquad (2.67)$$

With $\vec{x}_0$ representing the position at the beginning of the step, and the angle brackets denoting the fact that the statistical formulation of the physical effects produced by the individual forces is employed.

The second approximation is that *the energy does not change much* over the course of the particle's step. Thus, in the small energy loss limit Eq. (2.67) becomes:

$$\vec{v} = \vec{v}_0 + \frac{1}{m_0\gamma(E_0)}\left[\langle\vec{F}_{ret}(E_0)\rangle t + \langle\vec{F}_{ms}(E_0)\rangle t + \int_0^t \vec{F}_{em}\big(\vec{x}_0, E_0, \vec{u}(t')\big)\, dt'\right] \qquad (2.68)$$

where, analogous to before, E_0 is the energy the particle has at the beginning of its step.

The third and final approximation we need to make is that the *direction of the particle* ($\vec{u}$) *changes very little* over the course of the particle's step. With this approximation we have:

$$\vec{v} = \vec{v}_0 + \frac{t}{m_0\gamma(E_0)}\left[\langle\vec{F}_{ret}(E_0)\rangle + \langle\vec{F}_{ms}(E_0)\rangle + \vec{F}_{em}(\vec{x}_0, E_0, \vec{u}_0)\right] \quad (2.69)$$

with $\vec{u}_0$ representing the direction vector at the beginning of the particle's step. In Eq. (2.69) $\vec{F}_{ret}$, $\vec{F}_{ms}$, and $\vec{F}_{em}$ are decoupled by virtue of the three approximations we have made. None of the approximations have assumed anything about the magnitude of any of the forces involved: the overall assumption was simply that the step size is small enough so that the forces do not modify the "force-free" trajectory too much. The approximation that the direction of the particle ($\vec{u}$) does not change much over the course of the particle's step is bound to be broken sometimes if the multiple-scattering model we use in our Monte Carlo includes large angle single event Rutherford scattering. However, the probability of such an event happening is low enough, that the error introduced by this constraint being occasionally broken is negligible[20].

2.10 References:

1. H.E. Johns and J.R. Cunningham, The Physics of Radiology, Fourth Edi (Charles C Thomas, Springfield, Illinois, 1983).

2. F.H. Attix, Introduction to Radiological Physics and Radiation Dosimetry (Wiley-Interscience John Wiley & Sons, New York, 1986).

3. M.J. Berger, J.H. Hubbell, S.M. Seltzer, J. Chang, J.S. Coursey, R. Sukumar, D.S. Zucker, and K. Olsen, https://www.nist.gov/pml/xcom-photon-cross-sections-database, (n.d.).

4. P. Mayles, A. Nahum, and J. Rosenwald, Handbook of Radiotherapy Physics: Theory and Practice (Taylor & Francis Group, New York, 2007).

5. F.M. Khan, The Physics of Radiation Therapy, Second Edi (Williams & Wilkins, Baltimore, 1994).

6. C.R. Blackwell, B.M. Coursey, K.P. Gall, J.M. Galvin, W.L. Mclaughlin, A.S. Meigooni, and C.G. Soares, "Radiochromic Film Dosimetry: Recommendation of AAPM Radiation Therapy Committe Task Group 55," Med. Phys. 25(11), 2093–2115 (1998).

7. A. Micke, D.F. Lewis, X. Yu, A. Micke, D.F. Lewis, and X. Yu, "Multichannel film dosimetry with nonuniformity correction Multichannel film dosimetry with nonuniformity correction," Med. Phys. 38(5), 2523–2534 (2011).

8. H. Morrison, G. Menon, and R.S. Sloboda, "Radiochromic film calibration for low-energy seed brachytherapy dose measurement," Med. Phys. 41(7), 1–11 (2014).

9. E.Y. León Marroquin, J.A. Herrera González, M.A. Camacho López, J.E. Villarreal Barajas, and O.A. García-Garduño, "Evaluation of the uncertainty in an EBT3 film dosimetry system utilizing net optical density," J. Appl. Clin. Med. Phys. 17(5), 466–481 (2016).

10. D.J. Griffiths, Introduction to Electrodynamics, Third Eddi (Prentice-Hall, Upper Saddle River, NJ, 1999).

11. J. Jackson, Classical Electrodynamics, Third Edit (Wiley, New York, 1999).

12. F. James, "Monte Carlo theory and practice," Rep. Prog. Phys. 43, 1147–1189 (1980).

13. G Comte de Buffon, "Essai d'arithm´etique morale," Suppl´ement ` a l'Histoire Nat. 4, (1777).

14. M.H. Kalos and P.A. Whitlock, Monte Carlo Methods, Second (Wiley, New York, 2008).

15. F. Salvat, M. Fern, and S. J, PENELOPE , a code system for Monte Carlo simulation of electron and photon transport (2006).

16. R. Morin, Monte Carlo Simulation in the Radiological Sciences (CRC Press Inc., 1988).

17. I. Kawrakow, E. Mainegra-Hing, D.W.O. Rogers, F. Tessier, and B.R.B. Walters, The EGSnrc Code System : Monte Carlo Simulation of Electron and Photon Transport (NRC Canada, 2011).

18. T.M. Jenkins, W.R. Nelson, and A. Rindi (eds.), Monte Carlo Transport of Electrons and Photons (Plenum Press, New York, 1988).

19. E.W. Larsen, "A theoretical derivation of the condensed history algorithm," Ann. Nucl.

Energy 19(10), 701–714 (1992).

20. A.F. Bielajew, “Electron transport in E and B Fields,” in Monte Carlo Transp. Electrons Photons, edited by T.M. Jenkins, W.R. Nelson, A. Rindi, A.E. Nahum and D.W.O. Rogers (Plenum Press, New York, 1989), pp. 421 – 434.

21. H.A. Bethe, “Theory of passage of swift corpuscular rays through matter,” Ann. Phys. 397(3), 325–400 (1930).

22. H.A. Bethe, “Braking Formula for Electrons of Relativistic Speed,” Zeitschrift fur Phys. 76, 293–299 (1932).

23. F. Bloch, “Bremsvermogen von Atomen mit mehreren Elektronen .,” Zeitschrift fur Phys. Phys. 81(5–6), 363–376 (1933).

24. G. Moliére, “Theorie der Streuung schneller geladener Teilchen I. Einzelstreuung am abgeschirmten Coulomb-Feld,” Zeitschrift für Naturforsch. A 2(3), 133–145 (1947).

25. G. Moliére, “Theorie der Streuung schneller geladener Teilchen II Mehrfach- und Vielfachstreuung,” Zeitschrift für Naturforsch. A 3(2), 78–97 (1948).

Chapter 3: Influence of Standard RF Coil Materials on Surface and Buildup Dose in Magnetic Fields

A version of this chapter has been published as: A. Ghila, B.G. Fallone, S. Rathee ***Influence of Standard RF Coil Materials on Surface and Buildup Dose from a 6MV Photon Beam in Magnetic Field,*** *Med. Phys.* ***43(11)*** *5808-5816, 2016.*

3.1 Introduction

An integrated linac-MR system[1–3] will offer an increased level of accuracy for radiation delivery, by combining the skin sparing and penetration of the high-energy linac with the superior soft tissue contrast and real time imaging capabilities of the MRI. As mentioned in Chapter 1, two human linac-MR prototypes have been built at the Cross Cancer Institute (Edmonton, Canada) to date: a head sized, 0.22 T, transverse field unit (Prototype I) and a whole-body sized, 0.56 T, parallel field unit (Prototype II). Some of the dosimetric effects for both the transverse and parallel linac-MR configurations have been investigated by our group[4–7] and by others[8–11]. The presence of the MRI's main magnetic field and its fringe alters the trajectory of secondary electrons resulting from photon irradiation both inside and outside the patient. For a transverse configuration system, the contaminant electrons that accompany the high energy photons[12] are swept from the beam by the magnetic field. However at tissue-air or tissue-lung interfaces, the magnetic field causes the exiting electrons to return back to the tissue, drastically increasing the distal dose[8]. Inverse planning based optimization, including the effects of the magnetic field, has been suggested as a possible solution to reduce the impact of this electron return effect (ERE) in head and neck, and prostate radiotherapy[13] for the transverse configuration. Parallel opposed fields have also been suggested as a simple way to reduce the dose modifications produced by the ERE[8]. The parallel configuration linac-MR systems will

confine secondary electrons within the beam aperture, resulting in sharper penumbras[14] and eliminating the problem of returning electrons[5]. This also means that the contaminant electrons produced by the high energy photon beam in the linac head and irradiated air column have a reduced lateral scatter which can increase the entrance surface dose[6, 11]. However, it has been determined[6, 7] that the surface dose increase is minimal for parallel configuration systems that have low magnetic fringe fields at the linac head.

Another source of dose perturbation in an integrated linac-MR system is the MRI's radio-frequency (RF) coils. During imaging, MRI uses RF coils to both excite the nuclear spins in the imaged volume and to acquire the signal from their subsequent relaxation. To pick up MR signals efficiently, the receive RF coils have to be in close proximity to the patient with separations typically ranging from ~0 cm (for surface coils) to ~10 cm (for other solenoidal or birdcage type coils). Regardless of whether a transverse or a parallel configuration linac-MR is used, for real time tumor tracking, the imaged volume has to contain the treated volume. Using commercially available RF coils implies the patient will probably be irradiated *through* the RF coil. A typical RF coil consists of a copper conductor, plastic casing that electrically insulates the conductor from the patient, and the tuning and matching electronics. The parts of the RF coil, which touch the patient, usually have a layer of foam padding as well. Thus, the high-energy photon beam will have to pass through all, or at least some of these materials, before reaching the patient. Any material inserted in the path of the beam is known to increase the patient surface and build-up dose, and attenuate the photon beam[15]. A previous study[16] investigated the effects of a flexible RF coil on patient dose distributions, using an in-house developed treatment planning software that accounted for the presence of the 1.5 T transverse magnetic field. Comparing dose distributions calculated with and without the RF coil, it was determined the

flexible coil would have a minimal impact on the target volume dose. However, experimental measurements of surface and buildup dose modifications due to RF coils in parallel and transverse magnetic fields have not been presented previously.

This chapter experimentally investigates the surface and buildup dose changes for some standard, off-the-shelf RF coil materials in both parallel and transverse magnetic fields. Depth dose was measured with these materials placed in the path of a 6 MV photon beam at various distances from the surface of polystyrene phantoms. Data was acquired with no magnetic field present, with a transverse 0.22 T magnetic field, and with a parallel 0.21 T magnetic field applied during the irradiation.

3.2 Materials and Methods

3.2.1 Surface and buildup dose measurements using ion chambers

An extrapolation chamber can accurately measure surface dose. However various fixed separation parallel plate ion chambers (ppic) have been used over the years, and the differences in measured surface dose between these chambers and extrapolation chamber measurements are well documented[17]. For the ion chamber measurements presented in this chapter, the dose measured with the entrance window aligned with phantom surface was taken as the surface dose. Thus the effective point of measurement was the bottom of the front entrance window, as suggested by the manufacturers.

The measurements without magnetic field were performed using a thin window Capintec PS-033 (Capintec, INC., Ramsey, NJ) ppic, embedded in a custom-built polystyrene phantom (ρ_{poly}=1.04g/cm^3) machined to provide a tight fit for the ion chamber. The ion chamber and

polystyrene phantom were placed on the couch of a Varian Silhouette clinical unit (Varian Medical Systems, Palo Alto, CA) and irradiated using 6 MV photons (Figure 3.1). For these measurements, the phantom source to surface distance (SSD) was the standard 100 cm and a 10×10 cm^2 field size was used.

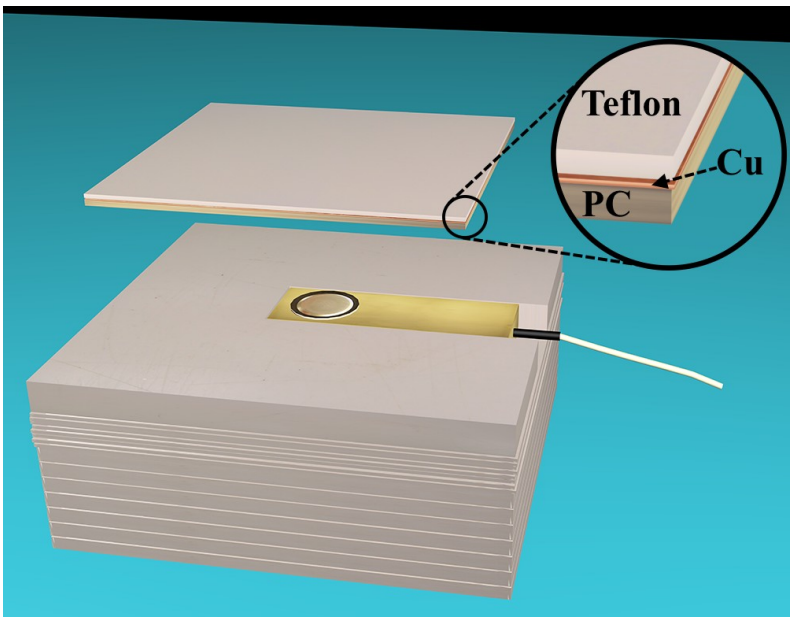

Figure 3.1 Polystyrene phantom with embedded Capintec PS-033 ppic. The imitation surface RF coil (1.5 mm PC, 0.08mm copper tape, 0.9 mm Teflon) was placed at various distances from the phantom surface in the path of the 6 MV beam.

The linac-MR Prototype I[1] was used for the transverse magnetic field measurements. This head-scale prototype uses a Varian 600C accelerating structure to provide 6 MV photon irradiation between the pole plates of the bi-planar permanent magnet. At the time of the measurements using this unit, the 600C accelerating structure only had the primary collimator installed. Thus, all the experiments performed with a transverse magnetic field used an un-collimated circular field. Although the un-collimated beam will have different treatment head electron contamination compared to the previous setup using the clinical linac, the 0.22 T transverse magnetic field will largely prevent these contaminant electrons from reaching the

phantom surface. The surface and depth dose were measured using the same Capintec PS-033 ion chamber and polystyrene phantom, modified to allow for horizontal depth dose measurements along the central axis of the beam (Figure 3.2 (a)). The phantom surface was positioned to coincide with the centre of the magnet at a SSD of ~80 cm. This is a non-standard SSD limited by the machine design. The transverse magnetic field purges the contaminant electrons from the treatment head, and the electron fluence, generated in the coil materials that reaches the chamber, depends on the air gap between the coil material and chamber surface. Thus, the measured surface dose in these experiments may be insensitive to the SSD.

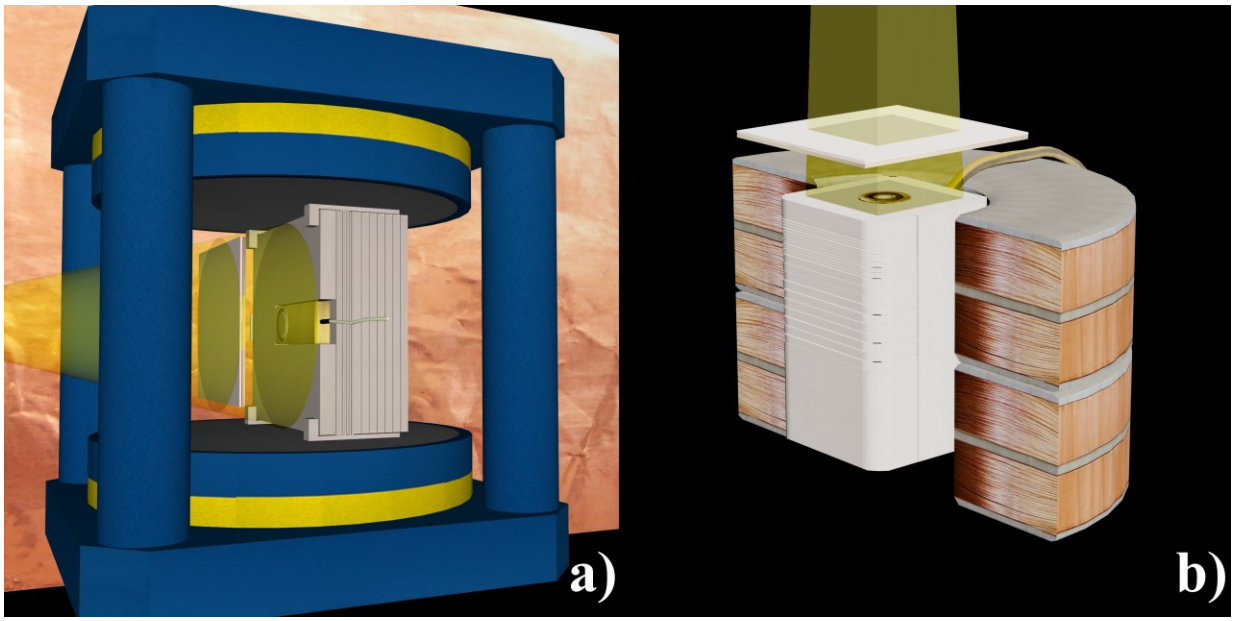

Figure 3.2 Ion chamber measurement setups: (a) Capintec PS-033 ppic depth dose measurement setup in the transverse magnetic field of the linac-MR Prototype I; (b) PTW Markus ppic depth dose measurement setup shown inside a cross section of the parallel configuration GMW electromagnets.

Since the sensitive volume of the Capintec PS-033 ion chamber is embedded in the acrylic body of the chamber by design, potential error-inducing air gaps[18] may only occur between buildup material and top of the entrance window. However, given the low (0.22 T)

magnetic field that results in a larger radius of curvature for the electrons, the errors due to air gaps were considered negligible for these transverse magnetic field measurements.

Experimental measurements of surface and buildup dose in a parallel configuration were facilitated by two solenoid electromagnets (model 3472-70, GMW Associates, San Carlos, CA). The two coils, placed on top of one another, provided a 26.5 cm deep, 17.5 cm diameter common bore, and a magnetic field strength of 0.21 T at the centre. A custom build wooden stand supported these magnets. The stand with the magnets was placed on the floor and the common bore was centered in the 6 MV photon beam of the Varian Silhouette unit. This placed the centre of the bore 183 cm from the radiation source, which ensured that the magnetic field would not affect the operation of the clinical linac. The magnetic field strength varied from 0.21 T in the center of the electromagnet bore to ~6 Gauss at the linac exit window, thus most of the contaminant electrons originating in the treatment head were located in the region of fringe magnetic field. These contaminant electrons were not as strongly confined by the weaker fringe magnetic field, and the coil materials absorbed most of the contaminants remaining in the beam.

A small size PTW Markus ppic (PTW, Freiburg, Germany) was embedded in another custom-built polystyrene phantom that fit inside the electromagnet's bore. The phantom used a rail design so that the ion chamber could be reproducibly stepped down, with varying thicknesses of buildup on top. The phantom surface coincided with the top of the electromagnets at an SSD of ~170 cm (Figure 3.2 (b)). Most parallel magnetic field measurements used a field size of 8.5 x 8.5 cm^2 at the surface of the phantom so as not to irradiate the electromagnet's coil structure directly, thereby reducing the unwanted scatter in the measurements. To study the influence of a smaller field size on the surface dose under the imitation RF coil (described in the next section)

we repeated a few surface dose measurements using a 5.1x5.1 cm^2 field size with the magnetic field turned off.

3.2.2 Typical RF coil materials

Various RF coil materials were placed in the 6 MV photon beam for all three measurement setups described above. An imitation RF coil was approximated using a 1.5 mm thick sheet of polycarbonate, with 0.08 mm copper tape, and 0.9 mm sheet of Teflon to simulate the base, conductor, and cover, respectively of a typical surface coil (Figure 3.1 insert). For this surface RF coil, the percent depth dose (PDD) curves were measured up to 2 cm depth.

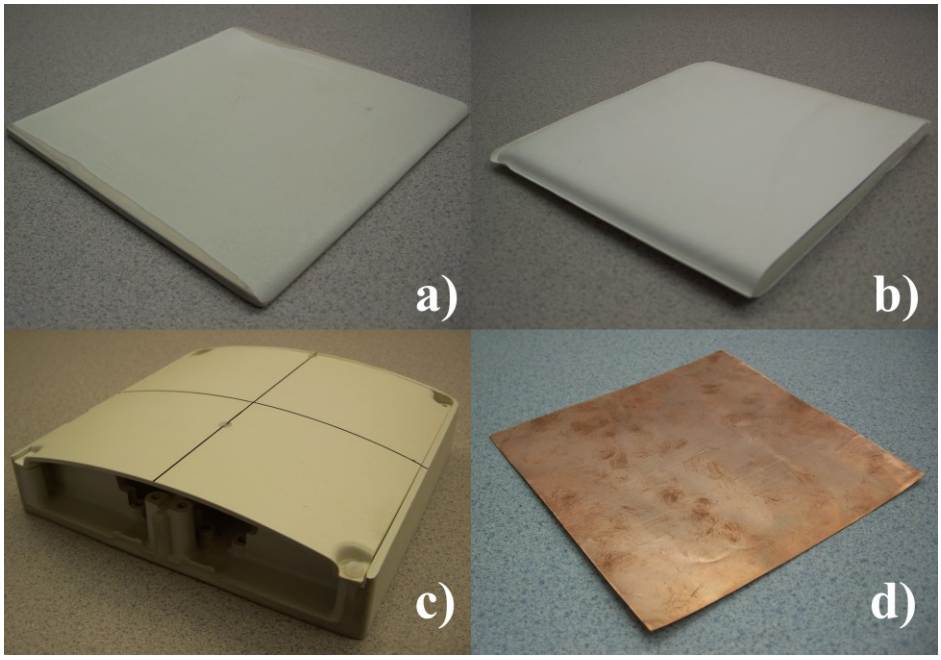

Figure 3.3 RF coil materials and parts: a) RF coil plastic cover (6mm thick); b)RF coil padding (15mm thick); c) full RF coil plastic casing (conductor removed); d) copper sheet representing RF coil conductor (0.1mm thick).

The surface dose increase, resulting from the following typical RF coil materials, was also investigated: 6 mm thick, single sheet, RF coil plastic cover (Figure 3.3 (a)); 15 mm thick RF coil foam padding (Figure 3.3 (b)); a RF coil plastic case with the conductor and electronics

removed (Figure 3.3 (c)); and a thin 0.1 mm copper sheet representing the conductor of an RF coil. For these materials, we measured the maximum dose (D_{max}) in the open beam (i.e. no coil material in the beam path), and then used D_{max} to normalize the measured surface dose with the coil materials in the beam path.

The surface dose effects of irradiating through a thin copper pipe (outer diameter 3.2 mm, inner diameter 1.5 mm), typically used as a conductor in birdcage type RF coils, were also investigated. As the thin copper pipe was comparable in size to the active volume of the PTW Markus chamber, and considerably smaller than the size of the Capintec PS-033 active volume, GAFChromic EBT3 film was used instead to measure surface beam profiles.

3.2.3 Dose measurements using GAFChromic film

A polystyrene phantom, that fit inside the parallel configuration electromagnet (Figure 3.4 (b)), was designed and built with a central film plane for depth dose measurements. The film was calibrated using the Varian Silhouette unit, and the dose was calculated using the dual channel method outlined by Micke *et. al*.[19] For each measured surface profile, two pieces cut from the same EBT3 film sheet were used: one piece was placed on the phantom surface (surface film), and the other along the central plane (depth dose film) of the polystyrene phantom. The surface film was carefully taped to the polystyrene phantom to minimize air gaps, while the depth dose film was taped and sandwiched between the two halves of the polystyrene phantom. Several measurements were acquired with the copper pipe placed at distances ranging from 0 cm to 5 cm from the surface of the phantom, using custom built holders placed outside the radiation beam. These measurements provided the surface dose profiles normalized to D_{max} of the open beam depth dose film. For the measurements in a transverse magnetic field, the phantom was placed on its side and centered in the beam with its height raised using an appropriate thickness

of Styrofoam (Figure 3.4 (a)). The measurements with no magnetic field used the same setup as shown in Figure 3.4(b) but with the electromagnet turned off. For both setups, the surface dose profiles were extracted parallel to the x-axis (Figure 3.4) along the center of the surface film.

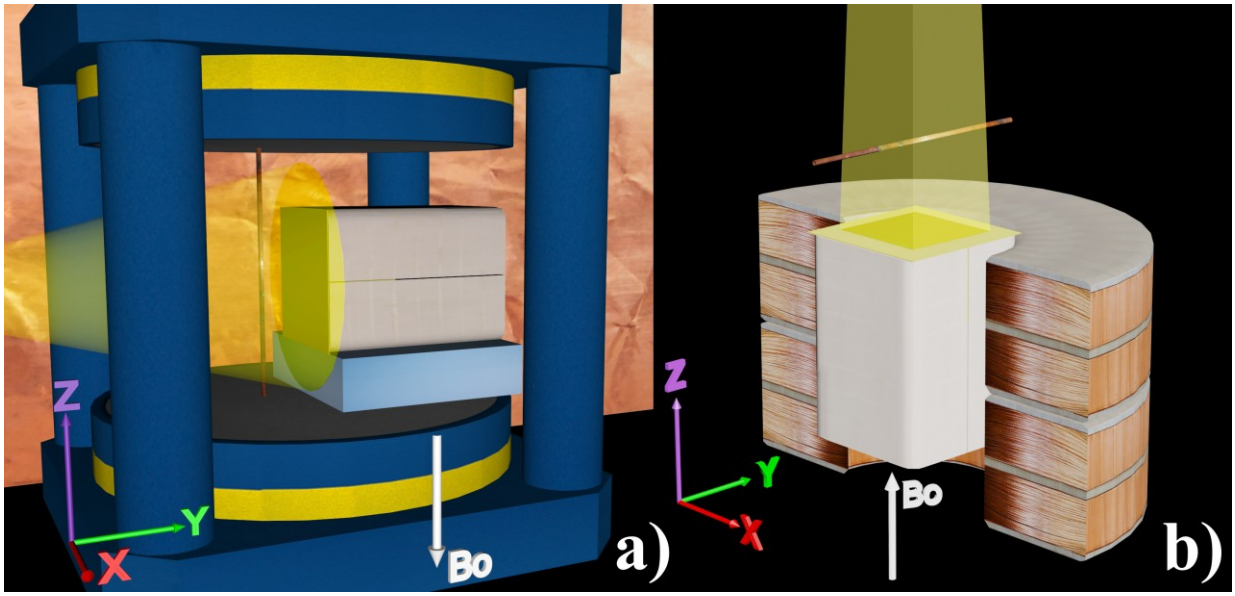

Figure 3.4 GAFChromic film phantom setup for copper pipe measurements in: (a) transverse magnetic field, and (b) parallel magnetic field. The beam profiles were measured parallel to the x-axis in the centre of the surface film.

3.3 Results and Discussion

3.3.1 Surface and buildup dose ion chamber measurements

Figure 3.5 shows the PDD changes caused by the imitation surface RF coil without any magnetic field, compared to the open beam PDD. The measured surface dose for the open beam (20%) matches the one measured by Gerbi and Khan[17] (19.8%) using the same chamber, which includes the surface dose measured by the extrapolation chamber and the correctional offset for the Capintec PS-033 ion chamber. When placed as a surface coil the imitation RF coil increases the surface dose from 20% to 78% of D_{max}. The buildup dose increases as well, with the coil essentially acting as a bolus and shifting the open beam PDD towards the phantom's surface.

Increasing the separation between the phantom surface and the imitation coil mitigates this effect, as more of the secondary electrons produced in the imitation coil by the 6 MV photon beam scatter laterally, and thus, less dose is deposited to the surface and in the buildup region. However, even with a 10 cm separation, the surface dose is still doubled (40%) when compared to the open beam.

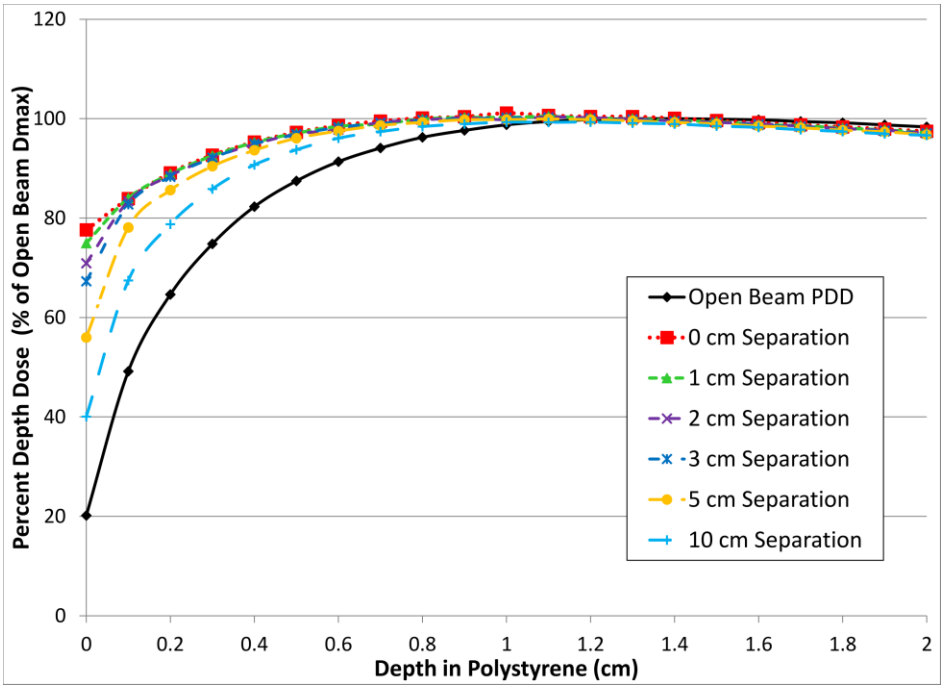

Figure 3.5 Influence of the imitation surface RF coil on the surface and buildup dose of a 6MV photon beam with NO magnetic field present. The indicated separation is between the imitation RF coil and the surface of the phantom.

Figure 3.6 compares the open field PDD with depth doses measured with the imitation surface coil in the beam for our parallel magnetic field configuration. The open beam PDD with no magnetic field was also measured with the PTW Markus chamber using the setup shown in Figure 3.2(b), but with the electromagnet powered down. We normalized the data to the no magnetic field D_{max}. This unshielded parallel magnetic field increases the surface dose of the

open beam by altering the direction of contaminant electrons originating in the treatment head and within the long air column (170 cm SSD).

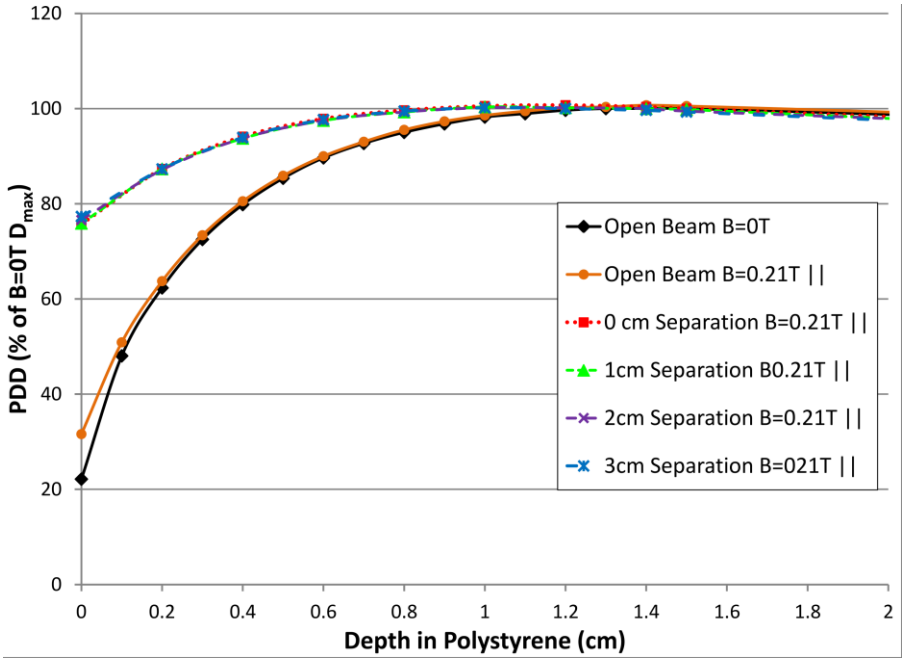

Figure 3.6 Depth dose profiles showing the influence of the imitation RF coil on surface and buildup dose in the presence of a 0.21T parallel magnetic field. The indicated separations are between the RF coil and the surface of the phantom.

Two processes contribute to the overall parallel magnetic field effect. Firstly the electrons with a tendency to scatter laterally will experience a Lorentz force that reduces their scatter out of the beam[14, 20]. Any contaminant electron with a directional vector not perfectly parallel to the local magnetic field will spiral around the magnetic field lines and thus have a reduced lateral scatter. The second process results from the fringe magnetic field lines of the electromagnet that converge towards the centre of the bore. Since the centre of the bore is aligned with the beam CAX, the contaminant electrons' spiral will be directed along the converging fringe magnetic field lines towards the centre of the beam. This concentration of contaminant electrons, in the parallel fringe magnetic field, towards the centre of the beam is responsible for the ~10% surface dose increase and a small increase in dose at 1 mm depth. The same effect was responsible for

the surface dose increase simulated by our group[6] and by the Australian group[11] although using completely different magnetic field configurations. With the imitation RF coil placed directly on the phantom, the apparent bolus effect raises the surface dose to 76%. As expected, when irradiating in the presence of a parallel magnetic field, increasing the separation between the RF coil and the surface of the phantom no longer decreases the surface and buildup dose. The strong magnetic field confines most of the electrons produced in the imitation RF coil, within the beam area for all the separations measured in this experiment. In another open beam experiment, the phantom surface was moved further away from the x-ray source and placed in the centre of the magnet bore. This setup created an additional 13 cm of air column in relatively high magnetic field and increased the open beam surface dose by >10%. There may also be a small increase in surface dose due to the imitation coil compared to what we measured with the current setup since the magnetic field at the top surface is lower (0.13 T) than in the center.

When a transverse magnetic field is present (Figure 3.7), the imitation surface coil produces a similar bolus effect with the corresponding surface PDD at 74% of open field D_{max}. However, the surface dose rapidly decreases as the separation increases between the surface of the phantom and the coil. Thus, with a separation of 3 cm and a transverse magnetic field, the surface and buildup dose increases are comparable to those obtained for a 10 cm separation and no magnetic field. This accelerated surface dose reduction is due to the electron return effect[8]. The electrons produced in the imitation coil have their largest directional component perpendicular to the main magnetic field causing their trajectories to curve away from the surface of the phantom. For example, the radius of curvature of 2 MeV electrons in 0.22 T perpendicular magnetic field is approximately 0.5 cm. Thus, the transverse magnetic field effectively sweeps

the contaminant electrons, produced in the RF coil, away from the surface of the phantom if given enough separation.

The shape of the buildup dose in Figure 3 of the paper[16] by Hoogcarspel *et al* conceptually agrees with the results presented in the current study, although Hoogcarspel *et al* calculated the dose using a treatment planning software at 1.5 T instead of measurement.

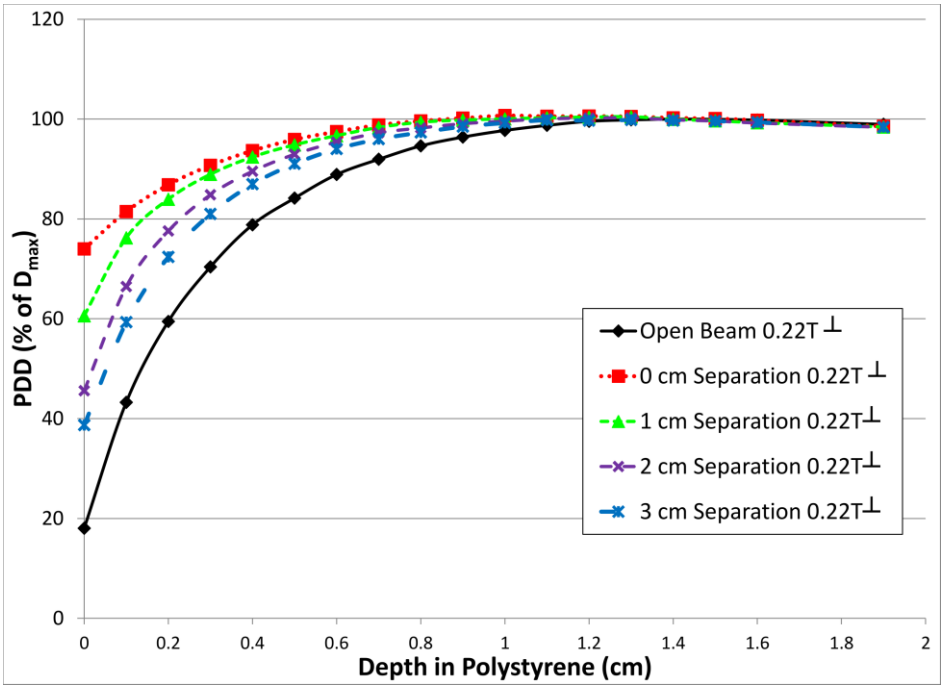

Figure 3.7 Influence of the imitation RF coil on surface and buildup dose in the presence of a 0.22T transverse magnetic field. The indicated separation is between the RF coil and the surface of the phantom.

3.3.2 Surface only dose ion chamber measurements

Figure 3.8 presents a summary of the surface dose effects caused by the imitation surface RF coil and the other investigated RF coil materials. The case without magnetic field used the experimental setup of Figure 3.2(b) with the electromagnet turned off. The data shown are averages over several measurements carried out on separate days; the standard deviation is

smaller than graph symbols. All the data points were normalized to the individual setup's open beam D_{max}. The solid horizontal lines represent the open beam surface dose.

With no magnetic field (Figure 3.8(a)), all the investigated materials display a similar trend with the surface dose being reduced by an increasing separation between the coil material and the surface of the phantom. When positioned right against the surface of the phantom, the 6 mm thick plastic cover and the RF coil casing result in the highest surface doses of 87%, and 83%, respectively. Even the low density RF coil foam padding increases the surface dose to 63% when placed, as it would be in a practical situation, in direct contact with the surface. The RF coil copper conductor by itself is responsible for approximately 20% surface dose increase when placed in close proximity (0 - 3 cm) to the polystyrene phantom.

In the parallel magnetic field, for zero separation, all the RF coil materials produce dose increases similar to the ones measured with no magnetic field present. Increasing the separation between coil material and surface however, no longer decreases the surface dose appreciably. In fact, except for the 0.1 mm copper conductor, a slight (1%-4%) surface dose increase is noticed for surface to coil separations between 0 and 3 cm. A noticeable decrease in surface dose occurs only for a 10 cm separation. This effect is due both to the parallel magnetic field confining the spread of the electrons produced in the coil material and the converging fringe magnetic field concentrating these contaminants towards the centre of the magnet, thus increasing the CAX dose since the center of the magnet bore is aligned with CAX. Increasing the separation between the coil material and the surface of the phantom will initially allow more electrons from the edges of the irradiated part of the coil to reach the central axis. If the separation is increased further, some of these electrons have a higher chance to interact within the air or to scatter laterally and thus to be effectively removed from the beam. Moreover, by increasing the

separation, the coil material moves towards the fringe magnetic field of lower strength (from 0.13 T at surface of phantom to 0.08 T at 10 cm separation). Thus electrons produced in the material are not as efficiently concentrated towards the centre of the beam by the weaker fringe magnetic field; however, this is a small effect.

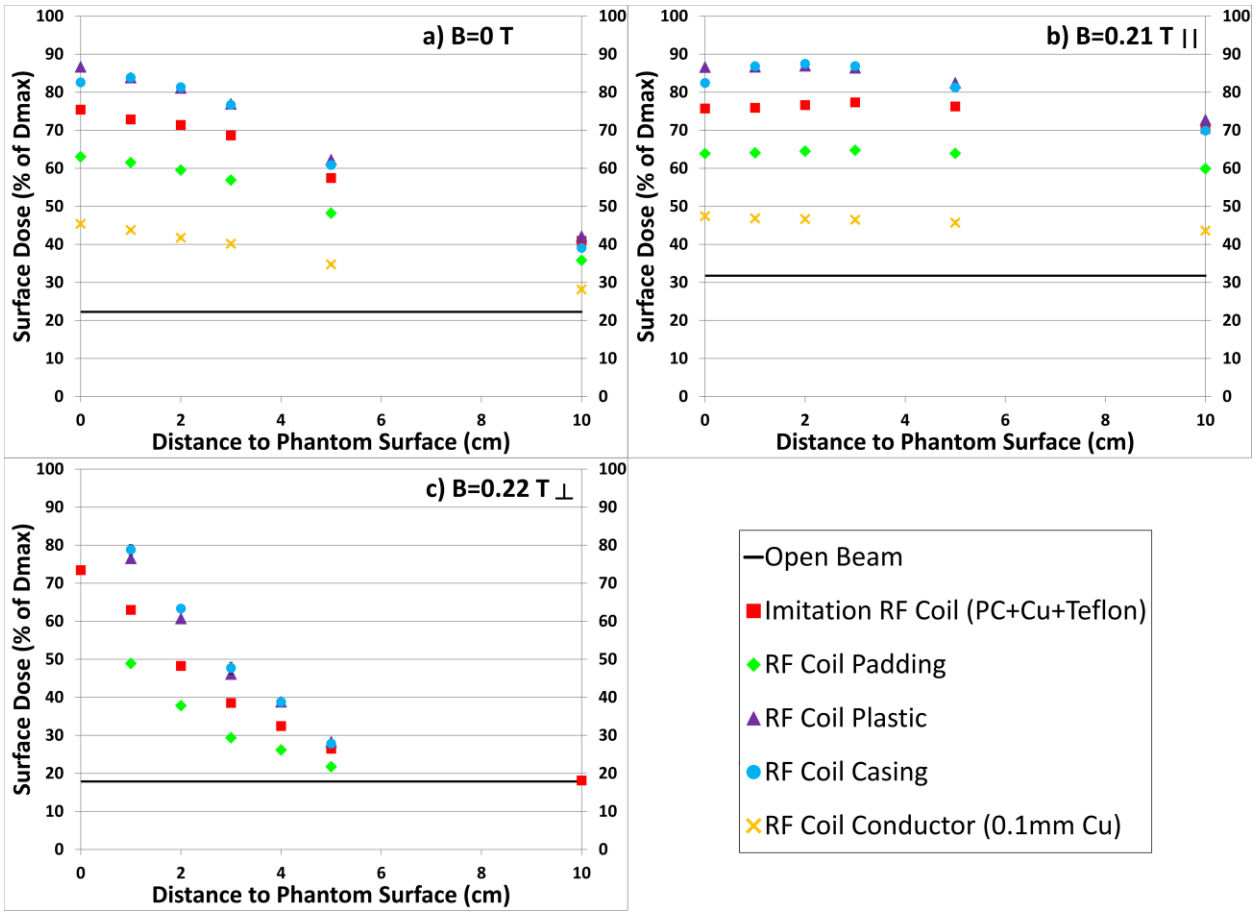

Figure 3.8 Surface dose increase due to the imitation RF coil, RF coil padding, RF coil plastic, RF coil casing, and RF coil conductor as a function of increasing separation from phantom surface with: a) NO magnetic field present; b) 0.21 T parallel magnetic field present, and c) 0.22T transverse magnetic field present during irradiation.

Figure 3.8(c) shows the surface dose rapidly decreasing with increasing separation between coil materials and phantom surface, with the same materials placed in the beam path in the presence of a transverse magnetic field. With a 5 cm separation, the surface dose increase was at most 10% compared to the open beam case, for all investigated RF coil materials placed

in the beam. For the imitation RF coil placed at 10 cm distance from the phantom, there was virtually no surface dose increase. This implies that for this large a separation, all the contaminant electrons produced in the coil materials were swept away from the phantom surface by the transverse magnetic field. For surface coils, however, this large separation between coil and patient surface is not advisable as it will decrease image quality considerably.

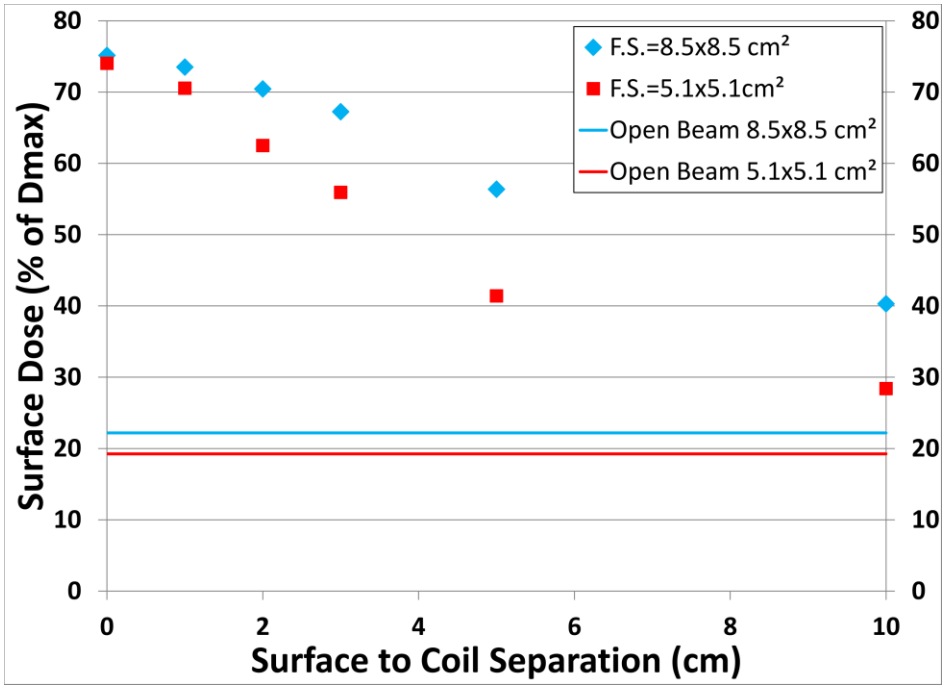

Figure 3.9 Influence of radiation field size on surface dose as a function of phantom surface to imitation RF coil separation, with no magnetic field.

Figure 3.9 shows the influence of the field size on the surface dose after the beam has passed through the imitation surface coil. When the imitation coil is in direct contact with the surface of the phantom, the difference between 8.5x8.5 cm^2 and the 5.1x5.1 cm^2 field sizes is only ~1%. However the surface dose for the smaller field size decreases more rapidly as the separation between the phantom surface and the imitation RF coil is increased. Thus, the surface dose for a 5 cm separation with the 5.1x5.1 cm^2 field size is comparable with a 10 cm separation for the 8.5x8.5 cm^2 field. Smaller field sizes are not expected to considerably change the surface

dose of a beam passing through an RF coil in the presence of a parallel magnetic field, based on the results from Figure 3.8(b). For a transverse configuration and with increasing separation between the coil and the patient surface however, the surface dose will decrease even faster than in Figure 3.8(c).

3.3.3 Surface dose GafChromic film profiles

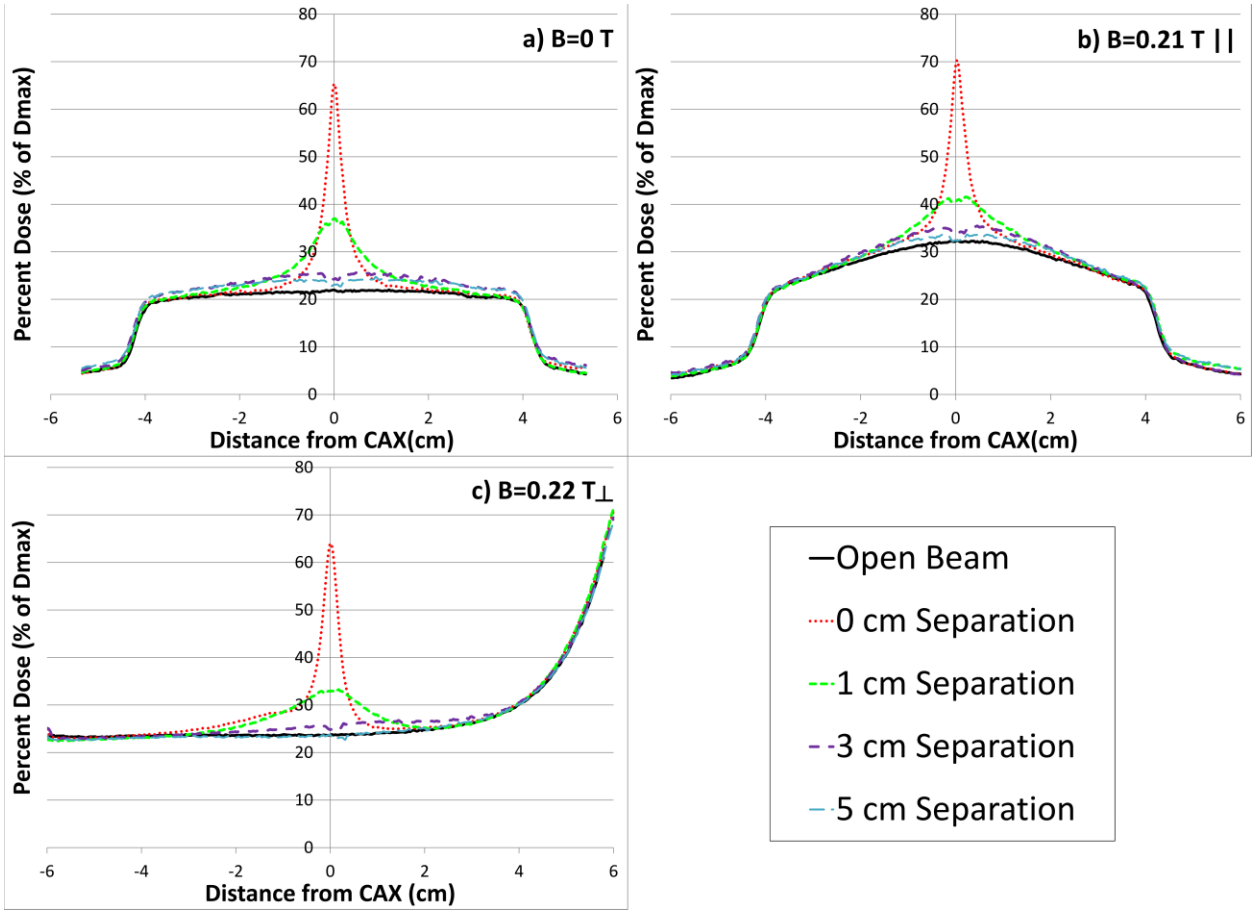

Figure 3.10 GAFChromic film measurements of the influence of thin copper pipe present in the 6MV photon beam on surface dose profiles with: a) no magnetic field, b) 0.21 T parallel magnetic field and c) 0.22 T transverse magnetic field. The separation between copper pipe and surface of phantom is as indicated in the legend.

Figure 3.10 summarizes the surface dose profiles measured perpendicular to the long axis of a thin copper pipe. Irrespective of magnetic field, a direct contact between the film and copper

pipe gives the highest surface dose (64% to 70% of D_{max}). As the distance between the copper pipe and phantom surface increases, the surface dose decreases and spreads out laterally. The surface dose increase is between 4% to 2% for separations from 3 cm to 5 cm and no magnetic field (Figure 3.10(a)).

In the parallel magnetic field (Figure 3.10(b)), the open beam profile dose increases symmetrically around the CAX. The open beam profile with a parallel magnetic field is no longer flat due to the parallel fringe magnetic field concentrating the contaminant electrons towards the beam centre. Adding the copper pipe in the beam both produces extra electrons that contribute to the surface dose and at the same time shields the surface from some of the contaminant electrons originating above the pipe. As such, the relative increase in dose is slightly smaller for all the separations when compared to the no magnetic field case.

In a transverse magnetic field, the previously observed lateral electron return effect[9, 21] can be seen on the positive *x* direction (see Figure 3.4(a) for axis orientation) of the surface beam profile in Figure 3.10(c). The lateral electron return effect is caused by the polystyrene phantom being smaller than the size of the un-collimated radiation field. The surface dose increase due to the lateral electron return effect is greater in magnitude than the increase caused by placing the small copper pipe in the radiation beam. The surface dose increase, due to the copper pipe with zero separation, is approximately the same as for the case without magnetic field (64% of D_{max}). For a separation of 5 cm, only a slight (1.1% of D_{max}) attenuation is observed at CAX. The transverse magnetic field also deflects the secondary electrons produced in the pipe towards positive *x* direction causing an asymmetry in the surface dose profile. When the pipe is in direct contact with the film, the electrons scattered from the pipe in the positive *x* direction are curved away from the film plane while the ones scattered in the negative direction are curved towards

the film. This causes the pipe profile to have a sharper drop off in the positive x direction. As the copper pipe is moved away from the surface of the film, the electrons scattered in the negative *x* direction actually curve under the pipe and some of them deposit their dose on the positive side. This leads to the observed dose overshoot in the positive *x* direction.

3.4 Conclusions

Irradiating through a surface RF coil, during a linac-MR treatment, will increase the surface and buildup dose considerably, regardless of magnetic field presence or orientation. The use of solenoidal or bird cage RF coils, which can be positioned several centimeters away from the patient skin, mitigates the surface dose increase for the transverse magnetic field orientation. In the parallel configuration, the surface dose stays relatively high regardless of patient to coil distance, only slightly decreasing for separations > 5 cm.

To avoid overdosing the patient skin the RF coil materials and their positioning with respect to the patient are important factors to consider. The effect of coils on dose distribution could be accounted for by integrating the coils in the treatment planning and dose calculation in the presence of magnetic fields. However, this could prove difficult as the RF coil location and the exact configuration of materials within must be accurately known. The use of RF coils with radiation windows that allow unobstructed irradiation of the patient for various beam angles would also not increase the entrance skin dose. Another potential solution to reduce the skin dose is to design and use RF coils with thin, low-density materials, which reduce the number of secondary electrons produced by the high energy photon beam in the RF coil materials. Ideally, being able to irradiate through the RF coil, at any beam angle, with the least amount of impact on

the surface and buildup dose, would allow for the greatest flexibility in treatment planning, setup, and delivery.

3.5 References:

1. B.G. Fallone, B. Murray, S. Rathee, T. Stanescu, S. Steciw, S. Vidakovic, E. Blosser, and D. Tymofichuk, "First MR images obtained during megavoltage photon irradiation from a prototype integrated linac-MR system," Med. Phys. **36**(6), 2084–2088 (2009).

2. B.W. Raaymakers, J.J.W. Lagendijk, J. Overweg, J.G.M. Kok, A.J.E. Raaijmakers, E.M. Kerkhof, R.W. van der Put, I. Meijsing, S.P.M. Crijns, F. Benedosso, M. van Vulpen, C.H.W. de Graaff, J. Allen, and K.J. Brown, "Integrating a 1.5 T MRI scanner with a 6 MV accelerator: proof of concept.," Phys. Med. Biol. **54**(12), N229–N237 (2009).

3. B.M. Oborn, S. Kolling, P.E. Metcalfe, S. Crozier, D.W. Litzenberg, and P.J. Keall, "Electron contamination modeling and reduction in a 1 T open bore inline MRI-linac system.," Med. Phys. **41**(5), 1–15 (2014).

4. C. Kirkby, T. Stanescu, S. Rathee, M. Carlone, B. Murray, and B.G. Fallone, "Patient dosimetry for hybrid MRI-radiotherapy systems," Med. Phys. **35**(3), 1019–1027 (2008).

5. C. Kirkby, B. Murray, S. Rathee, and B.G. Fallone, "Lung dosimetry in a linac-MRI radiotherapy unit with a longitudinal magnetic field," Med. Phys. **37**(9), 4722–4732 (2010).

6. A. Keyvanloo, B. Burke, B. Warkentin, T. Tadic, S. Rathee, C. Kirkby, D.M. Santos, and B.G. Fallone, "Skin dose in longitudinal and transverse linac-MRIs using Monte Carlo and realistic 3D MRI field models," Med. Phys. **39**(10), 6509–6521 (2012).

7. A. Keyvanloo, B. Burke, J.S. Aubin, D. Baillie, K. Wachowicz, B. Warkentin, S. Steciw, and B.G. Fallone, "Minimal skin dose increase in longitudinal rotating biplanar linac-MR

systems : examination of radiation energy and flattening filter design," Phys. Med. Biol. **61**, 3527–3539 (2016).

8. A.J.E. Raaijmakers, B.W. Raaymakers, and J.J.W. Lagendijk, "Integrating a MRI scanner with a 6 MV radiotherapy accelerator: dose increase at tissue-air interfaces in a lateral magnetic field due to returning electrons.," Phys. Med. Biol. **50**(7), 1363–1376 (2005).

9. A.J.E. Raaijmakers, B.W. Raaymakers, S. Van der Meer, and J.J.W. Lagendijk, "Integrating a MRI scanner with a 6 MV radiotherapy accelerator: impact of the surface orientation on the entrance and exit dose due to the transverse magnetic field," Phys. Med. Biol. **52**(7), 929–939 (2007).

10. B.M. Oborn, P.E. Metcalfe, M.J. Butson, and a B. Rosenfeld, "Monte Carlo characterization of skin doses in 6 MV transverse field MRI-linac systems: effect of field size, surface orientation, magnetic field strength, and exit bolus.," Med. Phys. **37**(10), 5208–5217 (2010).

11. B.M. Oborn, P.E. Metcalfe, M.J. Butson, a. B. Rosenfeld, and P.J. Keall, "Electron contamination modeling and skin dose in 6 MV longitudinal field MRIgRT: Impact of the MRI and MRI fringe field," Med. Phys. **39**(2), 874–890 (2012).

12. B. Nilsson and a Brahme, "Absorbed dose from secondary electrons in high energy photon beams.," Phys. Med. Biol. **24**(5), 901–12 (1979).

13. A.J.E. Raaijmakers, B. Hårdemark, B.W. Raaymakers, C.P.J. Raaijmakers, and J.J.W. Lagendijk, "Dose optimization for the MRI-accelerator: IMRT in the presence of a magnetic field.," Phys. Med. Biol. **52**(23), 7045–7054 (2007).

14. D.W. Litzenberg, B. a Fraass, D.L. McShan, T.W. O'Donnell, D. a Roberts, F.D. Becchetti, a F. Bielajew, and J.M. Moran, "An apparatus for applying strong longitudinal magnetic fields to clinical photon and electron beams.," Phys. Med. Biol. **46**(5), N105–N115 (2001).

15. A.J. Olch, L. Gerig, H. Li, I. Mihaylov, and A. Morgan, "Dosimetric effects caused by couch tops and immobilization devices: Report of AAPM Task Group 176," Med. Phys. **41**(6), 1–30 (2014).

16. S.J. Hoogcarspel, S.P.M. Crijns, J.J.W. Lagendijk, M. van Vulpen, and B.W. Raaymakers, "The feasibility of using a conventional flexible RF coil for an online MR-guided radiotherapy treatment.," Phys. Med. Biol. **58**(6), 1925–1932 (2013).

17. B.J. Gerbi and F.M. Khan, "Measurement of dose in the buildup region using fixed-separation plane-parallel ionization chambers," Med. Phys. **17**(1), 17–26 (1990).

18. S.L. Hackett, B. Van Asselen, J.W.H. Wolthaus, J.G.M. Kok, S.J. Woodings, J.J.W. Lagendijk, and B.W. Raaymakers, "Consequences of air around an ionization chamber : Are existing solid phantoms suitable for reference dosimetry on an MR-linac ?," Med. Phys. **43**(7), 3961–3968 (2016).

19. A. Micke, D.F. Lewis, X. Yu, A. Micke, D.F. Lewis, and X. Yu, "Multichannel film dosimetry with nonuniformity correction," Med. Phys. **38**(5), 2523–2534 (2011).

20. Y. Chen, A.F. Bielajew, D.W. Litzenberg, J.M. Moran, and F.D. Becchetti, "Magnetic confinement of electron and photon radiotherapy dose: a Monte Carlo simulation with a nonuniform longitudinal magnetic field.," Med. Phys. **32**(12), 3810–3818 (2005).

21. A.J.E. Raaijmakers, B.W. Raaymakers, and J.J.W. Lagendijk, “Experimental verification of magnetic field dose effects for the MRI-accelerator.,” Phys. Med. Biol. **52**(14), 4283–4291 (2007).

Chapter 4: Experimental Verification of EGSnrc Within a Realistic Parallel Magnetic Field

A version of this chapter has been published as: Andrei Ghila, Stephen Steciw, B.Gino Fallone, Satyapal Rathee ***Experimental verification of EGSnrc Monte Carlo calculated depth doses within a realistic parallel magnetic field in a polystyrene phantom,*** *Med. Phys.* ***44(9)*** *4804-4815, 2017.*

4.1 Introduction

The ultimate goal of developing an integrated linac-MR system is to use the MRI's exquisite soft tissue contrast to acquire real time images of the irradiated volume and adapt the treatment delivery concurrently[1-3]. Tracking moving tumors, and adapting the plan to changes in tumors' shape and size as well as to changes in patients' anatomy would allow for a reduction in treatment margins and lead to greater healthy tissue sparing.

Whether using a transverse configuration system or a parallel linac-MR, like the ones developed at the Cross Cancer Institute,[1,4-6] the patient will be irradiated in the presence of a strong magnetic field which will cause dose deposition modifications. It has been previously shown that systems with a transverse magnetic field configuration suffer from significant dose modifications when compared to conventional, no magnetic field, treatments[7-10]. Effects such as the previously mentioned electron return effect[8], depth dose modifications, and lateral beam profile shifts have all been investigated, and shown to increase the exit surface dose and create hot and cold spots at tissue-air or tissue-lung interfaces. These dose perturbations generally become more severe at higher magnetic field strengths[9].

The aforementioned dosimetric effects are considerably reduced for a parallel magnetic field configuration system, since the Lorentz force no longer causes the secondary electrons to

return, but simply confines their lateral spread within the beam area. The electron path confinement however, results in an increased number of contaminant electrons being concentrated within the beam area by the parallel magnetic field. These extra contaminant electrons, originating in the linac head and in the irradiated air column between the linac head and the patient, will cause an increase in the surface and buildup doses of the patient, as was shown in the "open beam" and surface measurements presented in the previous chapter. The magnitude of this increase will depend on the configuration and strength of the main magnetic field and of the fringe fields. The surface dose increase has been calculated using MC to be >400%[11] of D_{max} for unrealistic fringe magnetic fields (or for magnets with no yoke), and as low as ~3%[5] for realistically small fringe magnetic fields (or for magnets with appropriately designed yokes) for a 20×20 cm^2, 6 MV photon beam in the presence of a 0.5 T magnetic field.

A precise understanding of all the magnetic field dose effects is paramount to the clinical implementation of an integrated linac-MR unit. All the magnetic field induced dose differences compared to a conventional treatment have to be thoroughly understood and incorporated in the treatment planning process. The MC simulation method of dose calculation is considered one of the most accurate methods of calculating dose distributions in an arbitrary geometry[12]. The two main MC packages that have been used extensively so far to simulate the magnetic field effects for integrated linac-MR units are Geant4[3,8,13,14] and EGSnrc[4,5,10,15], with the PENELOPE package also having been used in determining the change in the response of selected detectors in magnetic fields[16,17]. Geant4 dose calculations, in the presence of a magnetic field for a transverse linac-MR, have been experimentally validated by Raaijmakers *et al*[14] using a small magnet for the experimental setup. Malkov and Rogers[18] have recently compared EGSnrc calculated point doses for the NE2571 ion chamber to measurements[19] in the context of ion chamber response

with various magnetic field strengths. However, to date, EGSnrc depth dose calculations in phantom or patient in the presence of a parallel magnetic field have not been verified by experiment. The purpose of the current chapter is to experimentally explore the accuracy of EGSnrc calculated depth doses in a homogeneous tissue-like phantom, with a slight modification to the EGS code required to read in the 3D magnetic field map and use it in the standard electromagnetic field macros, as previously described[5,15]. This is achieved by verifying the agreement between the EGS calculated percent depth doses (PDDs) and the measurements performed using a parallel plate ion chamber in a polystyrene phantom placed inside the bore of a solenoidal electromagnet and irradiated using a clinical linac.

4.2 Materials and Methods

4.2.1 Electromagnet Measurement Setup

Two solenoid electromagnets (model 3472-70, GMW Associates, San Carlos, CA) were used to produce a magnetic field parallel to a 6 MV photon beam. Each of these electromagnets consists of two cylindrical copper coils connected in series, with water cooled disks above, below, and in between them, shown as thin grey bands in Figure 4.1. The electromagnets have an outer diameter of 39.4 cm, and an inner diameter of 17.7 cm, while each copper coil and water cooling disk have a height of 5.15 cm and 0.95 cm respectively. The two electromagnets were stacked on top of each other, electrically connected in series, and placed on a wooden stand as shown in Figure 4.1. To reduce the distortion in the magnetic field, the stand was constructed with no metal components. The wooden stand with the two electromagnets on top was placed on the floor of the treatment vault, and the bore was centered in the 6 MV beam of a Varian Silhouette linac (Varian Medical Systems, Palo Alto, CA). The magnetic field at the center of the

26.3 cm deep, 17.7 cm diameter common bore was measured to be 0.207 T, for a 69.0 A current. This magnetic field is close to the highest obtainable with this experimental setup, as the maximum allowed current for the two electromagnets is 70.0 A.

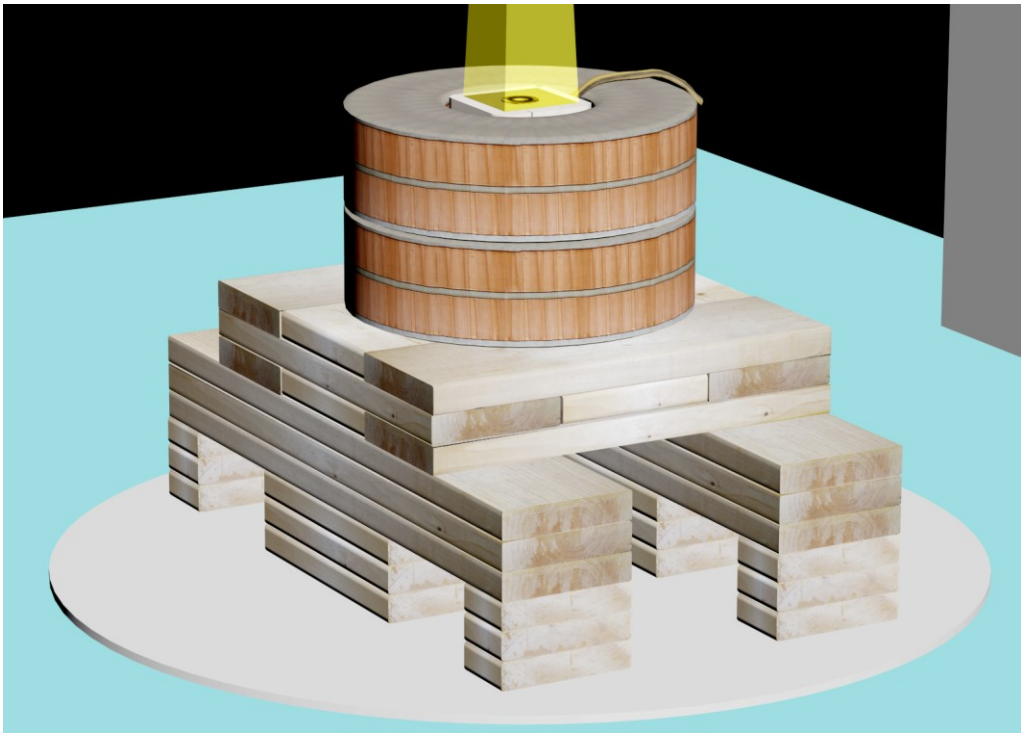

Figure 4.1 Dual GMW Electromagnet setup, with wooden stand, and polystyrene phantom. Setup is placed on the floor with the high energy photon beam irradiating straight down, from above.

The magnetic field distribution resulting from the two GMW electromagnetic coils is different from the magnetic field distribution of a parallel configuration linac-MR. Magnetic field homogeneity is significantly poorer compared to the imaging magnet, and the fringe magnetic fields, in a relative sense, are significantly larger since the experimental magnet is yokeless. However, the experimental magnet was mobile enough to be placed in a clinical linac vault to study the increase in surface and buildup doses. For the parallel linac-MR configuration, both the COMSOL calculation of the 3-D magnetic field distribution and the creation of a

validated linac head model are very complex and being pursued. This experimental magnet provided a more controlled, simple approach to test the EGSnrc Monte Carlo system with a realistic, variable, parallel magnetic field.

Figure 4.2 Cut-away view of the electromagnet showing the polystyrene phantom with build-up sheets and ion chamber insert on rails. This design allowed the ion chamber insert to be reproducibly stepped down through the stack of build-up sheets from the surface to a maximum possible depth of 16 cm.

A polystyrene phantom was custom built for measurements inside the parallel field electromagnet as shown in Figure 4.2. The phantom had a rail design that allowed the ion chamber insert to be reproducibly stepped up or down within the magnet bore with various thicknesses of buildup material on top. The dimensions of the phantom were 13×13×28 cm when fully loaded with buildup inserts, with rounded corners that allowed it to be easily inserted in the electromagnet bore. The buildup inserts were 0.1 cm and 0.6 cm thick, and the 1.4 cm thick ion chamber insert was custom built. A small PTW Markus parallel plate ion chamber (PTW, Freiburg, Germany) was snuggly fit in the phantom's ion chamber insert for the depth dose measurements. This ion chamber has a 0.03 mm polyethylene entrance window, 5.3 mm

diameter collector electrode and 2.0 mm electrode separation, and it is small enough to fit and be easily centered in the electromagnet bore.

Air gaps around cylindrical ion chambers are known to alter the chamber response in a transverse magnetic field[20]. The sensitive volume of the Markus ion chamber used in this study is embedded by design in the acrylic body of the chamber with a guard ring, making air gaps virtually nonexistent. Air gaps may potentially exist only between the entrance window and the buildup material layers. However, magnetic field lines at the location of the chamber within the electromagnet's volume are essentially parallel to the radiation beam. Therefore, the presence of a possible slab like air gap in a parallel magnetic field is expected to have a minimal impact on our parallel plate ion chamber's response.

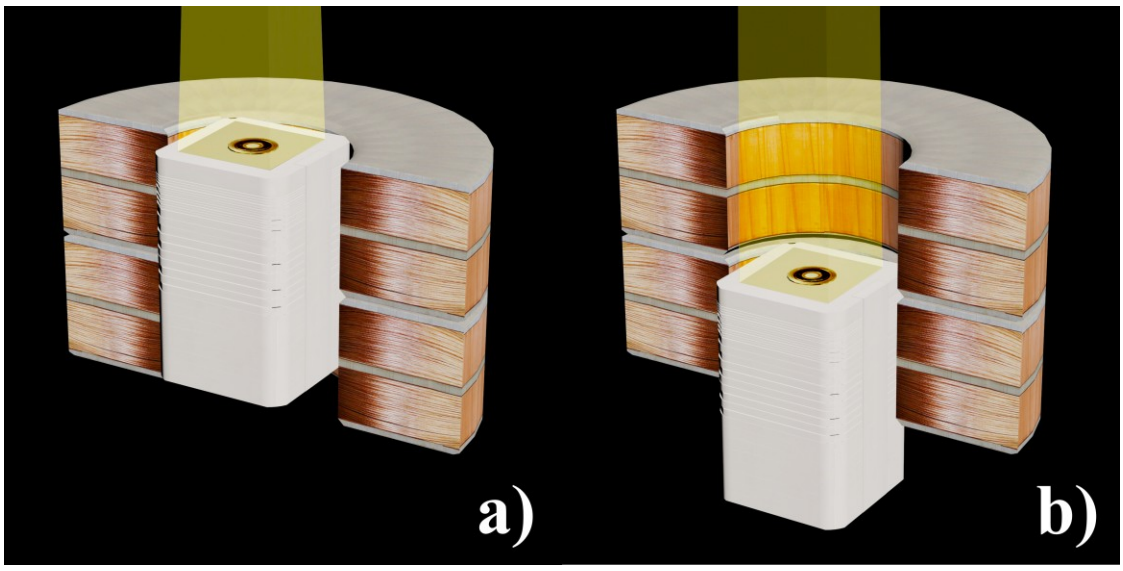

Figure 4.3 The two experimental setups used for measuring the depth dose in a parallel magnetic field: a) Surface of polystyrene phantom coincides with the top of electromagnet; b) surface of polystyrene phantom coincides with the center of electromagnet's bore.

Two experimental setups were used with regards to the position of the phantom within the electromagnet's bore. The first setup had the surface of the phantom at approximately the

same height (±2 mm) as the top of the electromagnets, as shown in Figure 4.3(a), with a source to surface distance (SSD) of ~170 cm; for the second setup the top surface of the phantom was aligned with the center of the bore (given by the plane where the top electromagnet rests on the bottom one, Figure 4.3(b)), with an SSD of ~183 cm.

4.2.2 Simulating the Linac

The EGSnrc MC Package was first used for modeling the high energy Varian Silhouette linac. All the MC simulations were run on the Westgrid* (Western Canada Research Grid) computing cluster. The linac head components were modeled, based on the dimensions and materials provided by the manufacturer, using BEAMnrc, while the depth dose and lateral beam profiles in a water phantom were scored using DOSXYZnrc. The simulated head components were from top to bottom: target, primary collimator, vacuum window, flattening filter, ion chamber, mirror, and collimator jaws. The simulated lateral beam profiles and depth dose curves were compared to the commissioning data measured using a water tank (Blue Phantom, IBA Dosimetry, Bartlett, TN) and an IC-10 ion chamber.

The EGSnrc parameters used for the BEAMnrc linac head simulations were as follows: directional bremsstrahlung splitting, with a splitting radius equal to the field size (5 cm, 10 cm, 20 cm and 40 cm), as recommended by the BEAMnrc manual[21], a distance from the bremsstrahlung target to the isocenter (where the field size is defined) of 87.3 cm, and a splitting factor of 1000. The Russian roulette plane was placed approximately 0.12 cm above the bottom of the flattening filter, (~12.82 cm from the top of the target). The global electron (ECUT) and photon (PCUT) cut-off energies were set to 0.700 MeV and 0.01 MeV, respectively, for all the

* Further details on installing and running EGSnrc on Westgrid/linux systems can be found in: G:\Medical Physics\Andrei\Westgrid MonteCarlo\

linac head components simulated in BEAMnrc, except for air which had ECUT = 0.521 MeV. This parameter set was chosen to speed up the calculation while generating a realistic contaminant electron fluence in the air column within, and right below the linac head, and was achieved by using a modified cross sectional data file for the BEAMnrc simulations. In this modified data file, air was the only material with cross sectional data for electron energies below 0.700 MeV (i.e. AE=0.521 MeV only for air). This ensured that, for all the higher density materials used in the simulation of the treatment head, electrons with energies below 0.700 MeV (including rest mass) would be absorbed locally, while in air, the contaminant electrons could be tracked all the way down to an energy of 0.521 MeV before stopping. For all the DOSXYZnrc simulations ECUT and PCUT were set to 0.521 MeV and 0.01 MeV respectively, and the regular (521icru.pegs4dat) cross sectional data file was used.

A phase space was scored 12 cm below the jaws of the linac, slightly (1.4 cm) above the Mylar exit window, and used as the input for DOSXYZnrc (ISOURCE 2, phase space source incident from any direction). Scoring the phase space file below all the components of the linac head would allow us to use the exact same phase space file for our magnetic field simulations once an acceptable match to the commissioning measurements was obtained. The DOSXYZnrc water phantom was modeled to be 66×66×50 cm^3, approximately the same dimensions as the water tank used during the commissioning measurements. Since the measured data was acquired using an IC-10 ion chamber with an active volume of 0.14 cm^3 and data points were acquired every 0.02 cm, two different phantoms were simulated in DOSXYZnrc to emulate the measurements. One phantom was used for scoring PDDs and had 0.5×0.5×0.1 cm^3 voxels, while the other phantom was used for scoring lateral beam profiles and had 0.1×0.5×0.5 cm^3 voxels. A five voxel moving average was used in the 0.1 cm direction to emulate a 0.5×0.5×0.5 cm^3

volume sampling the dose with an interval of 0.1 cm either down along the beam's central axis or across the beam profile. This process resulted in volume averaging of data points, similar to the one caused by the IC-10 ion chamber, separated at 0.1 cm intervals both in the lateral and depth directions. To speed up the simulations, and since the water phantoms were homogeneous, the HOWFARLESS algorithm was used. This algorithm removes the restriction that charged particle steps have to stop at each voxel boundary and only takes into account the whole phantom's outer boundaries yielding accurate dose results across all energies while improving the simulation efficiency by up to ~30%[22].

The spatial and energy distribution of the electron beam hitting the target in the BEAMnrc simulations were both modeled as Gaussian functions. The mean and full width half maxima (FWHM) of these Gaussians were adjusted until the simulated beam profiles and depth dose profiles matched the measurements. As described by Sheikh-Bagheri and Rogers[23], the small field (5×5 cm^2) profiles are virtually insensitive to the electron beam energy, but are extremely sensitive to the electron beam focal spot size, while large field profiles (40×40 cm^2) are sensitive to both the energy and size of the electron beam hitting the target. Thus, starting with the recommended parameters[23] the size of the electron beam was adjusted until the 5×5 cm^2 profile at a depth of 10 cm in water matched the measured one. Then, keeping the same electron beam size as in the previous step, the energy of the electron beam was adjusted until the 40×40 cm^2 beam profile at 10 cm depth matched the measurements. Intermediate field sizes of 10×10 cm^2, and 20×20 cm^2 were also investigated. For each of the four field sizes, the simulated PDD, and the cross beam profiles at 1.5 cm, 5.0 cm, 10.0 cm and 20.0 cm depths were compared to the ones measured during the commissioning process. Each curve was separately compared using a γ factor[24] analysis with a 2%, 2mm acceptance criterion, and without using a threshold.

To obtain a better match, the BEAMnrc default global Monte Carlo transport parameters for Bremsstrahlung angular sampling and the Bremsstrahlung cross sections had to be changed from their default values, 'Simple' and 'BH' (Bethe-Heitler), to the more accurate 'KM' (Koch-Motz) and 'NRC' respectively. 'Simple' determines the emission angle of Bremsstrahlung photons by using only the leading term in the Koch-Motz distribution while the 'KM' option uses the full modified Koch-Motz equation (2BS)[21,25]. The 'NRC' option ensures the NIST Bremsstrahlung cross section data base is used and includes corrections for electron-electron Bremsstrahlung[21].

4.2.3 Measurement and Simulation of the Magnetic Field

An accurate 3D magnetic field map extending all the way to the linac head was required for implementing the magnetic field of the two GMW electromagnets into the MC simulations. The magnetic field was measured using a three-axis Hall magnetometer (Model THM1176, Metrolab Technology SA, Switzerland), with the electromagnets placed in the treatment vault under the linac head. The magnetic field measurements were performed along the three orthogonal axes presented in the Figure 4.4 insert, and the measurements were repeated on different days.

The axial component of the magnetic field (B_Z) was measured along the central axis of the electromagnets (the Z axis in Figure 4.4 insert) starting from the centre of the common bore, and continuing towards the linac head up to a distance of 110 cm from the magnet centre. Both the radial and the axial components (B_X and B_Z respectively) were measured from -50 cm to +50 cm in both the X and Y directions. For this set of measurements the magnetic field values were acquired in a plane corresponding to the top of the two magnets (Z~14 cm), parallel to the X and Y axes (see Figure 4.4 insert).

By using the GMW coil dimensions mentioned in Section 2.1, 3D magnetic field maps were simulated using the finite element method (FEM) in COMSOL Multiphysics V4.4 (Burlington, MA), as our group has previous experience in simulating magnetic fields using COMSOL[6]. The simulations provided us with a 3D magnetic field map of the magnetic field components B_X, B_Y and B_Z at 1.0 cm intervals, extending from -50 cm to +50 cm in the X and Y directions, and from -20 cm to +182 cm in the Z direction. This map was validated using the magnetic field measurements, and then implemented in EGSnrc.

4.2.4 EGSnrc simulations in the presence of a magnetic field

To implement the magnetic field in EGSnrc, the macro packages dosxyznrc_user_macros.mortran and emf_macros.mortran were modified as previously described[4,10,15]. These two macros are called at the end of a charged particle transport step performed in the absence of an electro-magnetic field. This approach is based on the implementation by Alex F. Bielajew[26,27] where the transport in the presence of an electro-magnetic (EM) field is superimposed on the field-free charge particle transport. This method implements the approximations that over the charged particle's step: (a) the change in the particle's kinetic energy is small, (b) the change in the EM field magnitude is small, and (c) the relative change in the particle's direction of motion due to the Lorentz force is also small. Under these approximations the deflections of charged particles caused by inelastic scattering, multiple scattering and by the EM fields can be decoupled, as was shown in Chapter 2. To ensure that the conditions a), b), and c) are all met simultaneously, emf_macros.mortran uses macros that restrict the step size by imposing upper limits on the amount of deflection in the EM field (EMULMT), the amount of energy loss in the EM field (EMELMT), the amount the EM field changes over the transport step (EMFLMT), and finally on the average amount of change of the

direction vector due to multiple scattering (EMMLMT). After a few test simulations, we decided to use the default values for these parameters (EMELMT=0.02; EMFLMT=0.02; EMMLMT=0.20), except for EMULMT which was changed from 0.02 to 0.001. This caused the step sizes to be shorter, and thus increased the simulation time ~2.9 times compared to using the default EMULMT=0.02, but resulted in a better agreement of the final results with measurements.

The DOSXYZnrc macros were modified in-house to read the full 3D magnetic field map simulated using COMSOL, and to interpolate for any possible particle location. This caused a further increase in simulation time by a factor of ~3.5. The same phase space file obtained without a magnetic field was used for both the no magnetic field and with magnetic field DOSXYZnrc simulations. The linac head contains magnetic parts that will modify the magnetic field along the beam path between the target and the Mylar exit window below the collimator jaws. However, we considered that the magnetic field was weak enough (measured ~6.4 G at the Mylar window) that it would not significantly modify the contaminant electron trajectories above the linac exit window located 13.4 cm below the lower jaw.

The linac head presence was also not taken into account when calculating the magnetic field. Thus we are assuming that the ferromagnetic linac head parts only influence the area of very small magnetic field in their immediate vicinity, and have a minimal influence on the magnetic field around the phantom placed at a large SSD, which should lead to negligible effects on the final PDD simulations. To test this assumption, an iron cylinder (20 cm tall, 90 cm diameter) was placed in the COMSOL simulation with its bottom part at a distance of 130 cm from the centre of the magnet, approximately where the linac head is located in the experimental setup, and at the same height as the phase space file in the simulations. The magnetic field

recalculated with this iron cylinder in place was implemented in DOSXYZnrc and full depth dose profiles were simulated for each of the two setups. These were compared to the depth dose curves obtained using the magnetic field calculated without the iron plate.

For the surface and in the buildup region the simulated PDD values depend on the voxel size in the depth direction. Thus, to emulate the volume averaging present in the measurements a $0.5\times0.5\times0.2$ cm^3 cuboid air cavity with a $0.5\times0.5\times0.003$ cm^3 polyethylene window above the air cavity were simulated inside a $13\times13\times28$ cm^3 polystyrene block at each measurement depth in separate MC simulations. The whole simulated setup was surrounded by air on all sides. The actual (cylindrical) air cavity of the ion chamber was approximated as a cuboid because DOSXYZnrc only allows cuboidal geometries. More importantly, the chamber dimension in the depth direction (0.2 cm) is accurately modeled to simulate the volume averaging. A more accurate representation of the ion chamber cavity and window could have been defined in DOSRZnrc but that would not accurately implement the scattering in the cuboidal phantom by the rectangular beam.

Each simulation used 200 million particles, and the dose was scored as the dose to the air cavity, with a resulting statistical uncertainty of 0.4% on average. For each depth a new simulation was performed with both the air cavity and polyethylene window shifted down. Simulating the setup in this manner served to closely approximate the way the ion chamber is stepped down through the polystyrene phantom during the experiments and offered more accurate results, as any ion chamber specific dose perturbations were taken into account by the simulation. It also enabled us to directly compare the measurements and simulations without having to apply any extra correction factors[28]. Both the measured and the simulated data points were normalized to their respective no magnetic field maximum dose. The absolute difference

between the ratio of measurements and simulations and unity, were compared to the estimated total uncertainty for each data point.

The slab geometry, described above, is very similar to one of the setups investigated by Malkov and Rogers[18]. Using the default values for the EMULMT, EMELMT, EMFLMT, and EMMLMT parameters, and the default condensed history implementation (one point integration technique) EGSnrc has been shown to pass the Fano test[18], modified to accommodate an external magnetic field as described by Bouchard *et al.*[29]. Malkov and Rogers also modified the boundary crossing algorithm and implemented the single scatter calculations which used an analytical expression to transport particles in a constant magnetic field. Thus the calculations were accurate even when large particle step sizes were used in the EGSnrc simulations. Aside from reading the magnetic field map and interpolating the magnetic field for any particle position the current study uses EGSnrc's default magnetic field implementation. The current implementation is expected to pass the modified Fano test, since the parameter that controls the deflection in the EM field (EMULMT) has been reduced from the default 0.02 to 0.001, thus restricting particle transport to fairly small step sizes.

4.3 Results and Discussion

4.3.1 Measurement and simulation of the magnetic field

The comparison between the COMSOL simulated and the measured magnetic field of the two combined GMW electromagnets is presented in Figure 4.4. The measured data points were calculated as an average of the +X, -X, +Y, and -Y measurements based on the rotational symmetry of the magnetic field. The axial field (Bz) measurements along the Z axis were

performed twice on separate days, and averaged. A ±1 cm positioning error was considered for the Metrolab probe, as the sensitive tip of the probe is ~1.7 cm long.

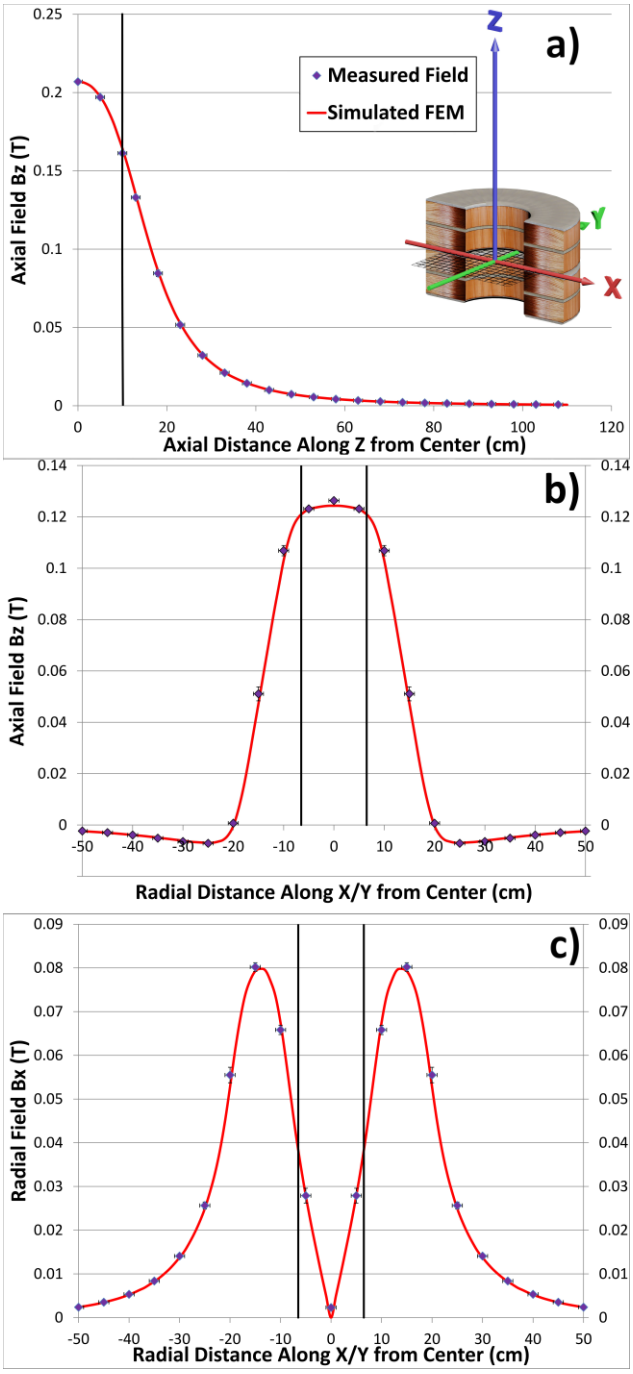

Figure 4.4 FEM calculated magnetic field compared to point measurements: a) Axial field Bz along central Z axis; b) Axial field Bz along either X or Y axis, at Z=14 cm; c) Radial field Bx along either X or Y axis, at Z=14 cm. The X, Y, Z axes are shown in the top right insert and the black vertical lines represent the physical limits of the phantom with respect to the magnetic field.

The simulated data is in excellent agreement with the measurements, all points agreeing within 2% of the maximum 0.207 T central field. More than half of all the simulated points, at the locations where the magnetic field was measured, matched the measured values within the experimental uncertainty of 1.5% of the maximum field.

As this magnetic field simulation does not take into account the presence of the ferromagnetic linac head, this also indicates that the electromagnets were placed far enough away such that the main magnetic field was virtually unaffected. The solid black lines represent the physical limits of the polystyrene phantom as it was positioned with its top surface aligned with the top of the magnet bore. In Figure 4.4(a) the top surface of the phantom is at Z=13.1 cm, while in Figure 4.4(b) and Figure 4.4(c) the solid black lines are simply the sides of the phantom at ±6.5 cm.

4.3.2 Simulating the linac

The optimal parameters, for the electron beam hitting the target, were found to be the following: mean electron beam energy of 5.55 MeV, with an energy FWHM of 8%, and a spatial FWHM of 0.27 cm. Using these parameters, 100% of the simulated points passed the 2%, 2 mm γ acceptance criterion when comparing the beam profiles for the small 5x5 cm^2 field size (Figure 4.5). For the large, 40×40 cm^2 beam profile (Figure 4.6), over 93% of the simulated points passed the γ acceptance criterion. The 10×10 cm^2 and 20×20 cm^2 simulated profiles matched the measurements with over 96% and 98% of the points passing the 2%, 2mm γ criterion respectively.

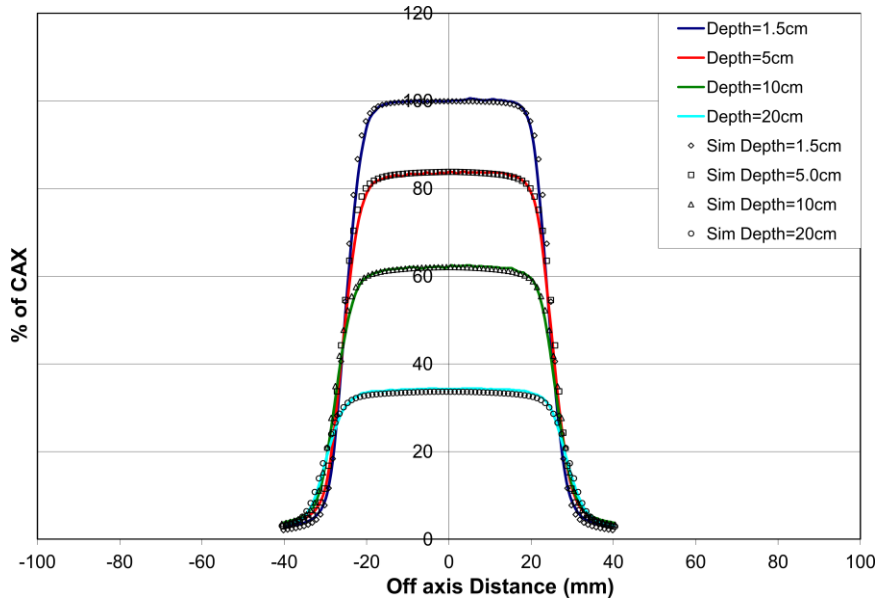

Figure 4.5 Comparison of measured and simulated 5×5 cm^2 beam profiles at 1.5 cm, 5.0 cm, 10.0 cm and 20.0 cm depths. All of the simulated points pass the 2%, 2 mm γ acceptance criterion.

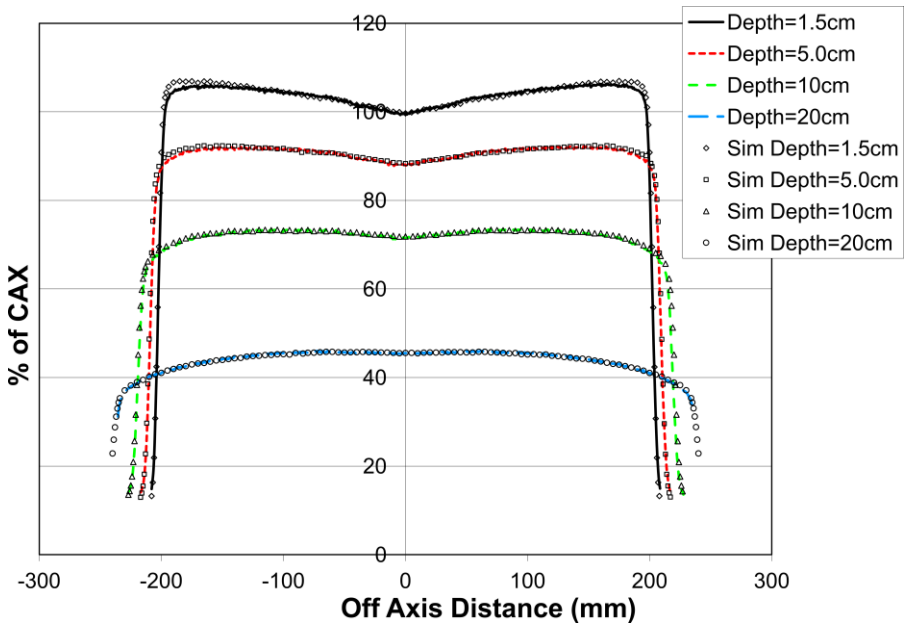

Figure 4.6 Comparison of measured and simulated 40×40 cm^2 beam profiles at 1.5 cm, 5.0 cm, 10.0 cm and 20.0 cm depths. Over 93% of the simulated points pass the 2%, 2mm γ acceptance criterion.

The 40×40 cm^2 cross beam profile at shallow depths is extremely sensitive to the exact shape and dimensions of the flattening filter. The discrepancy noticeable for the 1.5 cm depth in Figure 4.6 is probably due to the Varian Silhouette unit having a slightly updated flattening filter, compared to the information available.

The simulated depth dose profiles are compared to the ion chamber measurements in Figure 4.7. An excellent agreement was obtained using the aforementioned electron beam parameters with over 99% of the simulated points passing the 2%, 2 mm γ criterion.

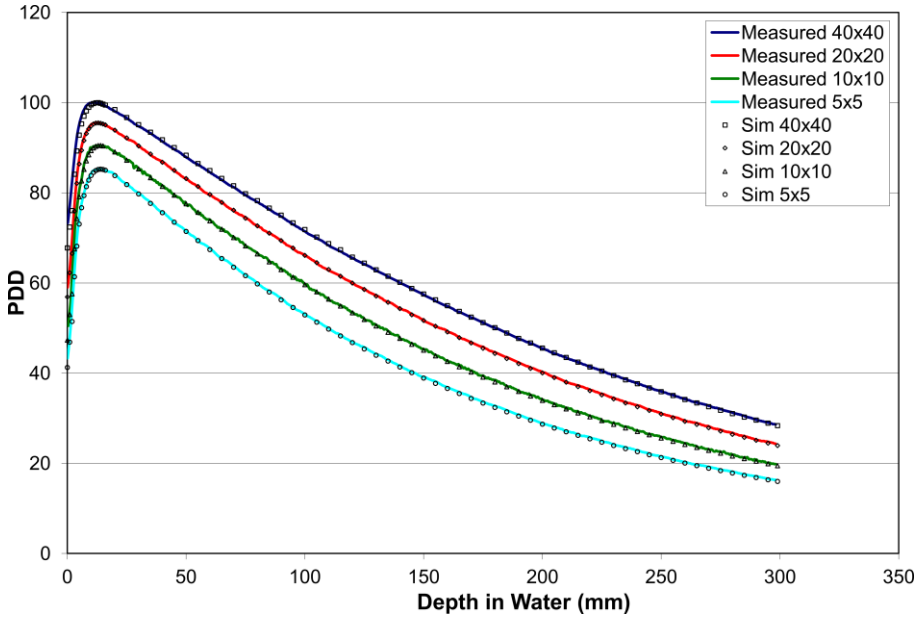

Figure 4.7 Measured and simulated depth dose profiles for the 40×40 cm^2, 20×20 cm^2, 10×10 cm^2 and 5×5 cm^2 field sizes. Over 99% of the points pass the 2%, 2mm γ acceptance criterion.

4.3.3 Measurements and EGSnrc simulations with a magnetic field

The measured (solid lines) and simulated (points) PDDs for the setup with the surface of the phantom coinciding with the top of the magnet bore (Figure 4.3(a)) are compared in Figure

4.8. The uncertainties for the simulated points, both with and without the magnetic field, are smaller than the size of the data markers.

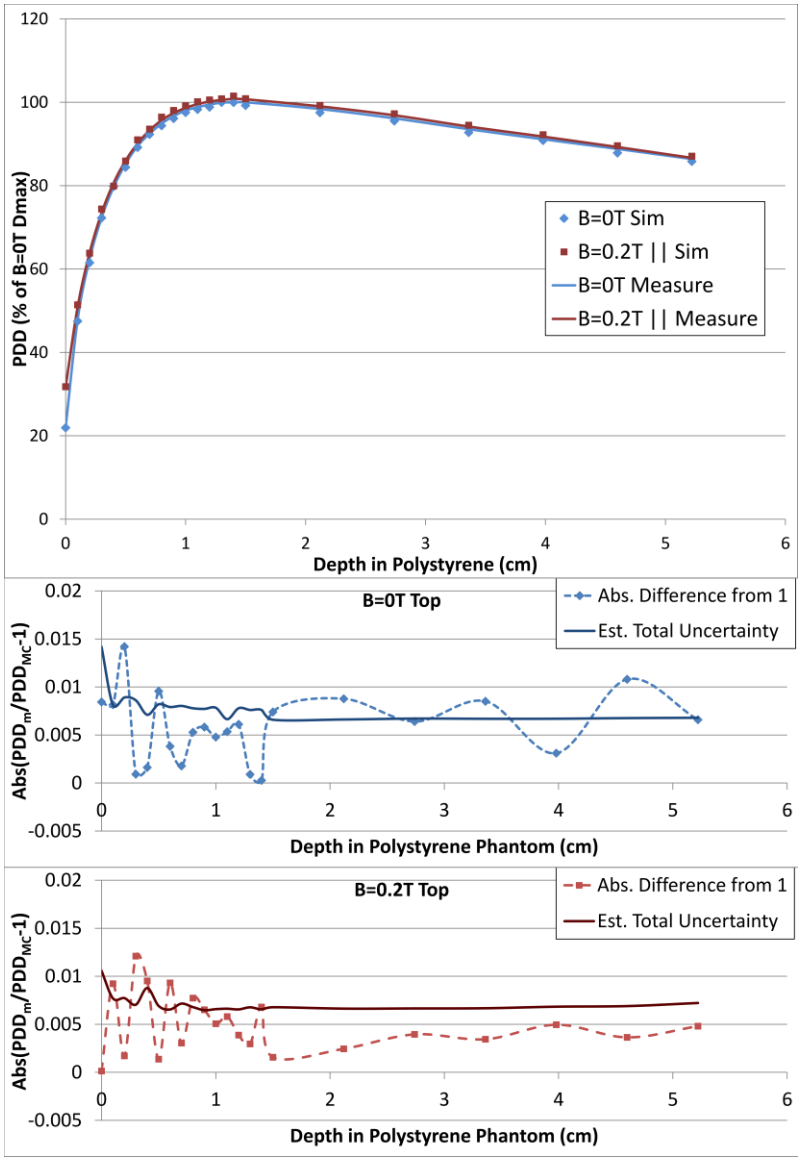

Figure 4.8 Measured and simulated PDD comparison for polystyrene phantom surface coinciding with top of the magnet (see Figure 4.3, a). The absolute difference between the ratio of measurements and simulations, and unity is compared to the estimated total uncertainty for each curve separately.

All the simulated points are within 1% (relative to the maximum dose with no magnetic field, D_{max}) of the measurements. The absolute difference between unity and the ratio of

measured to simulated doses at each point is also compared to the estimate of the total uncertainty in Figure 4.8. For both curves (B = 0T and B = 0.2T), the ratio of measured to simulated doses is within the total uncertainty (below solid line) when compared to unity for most points. The few points, for which absolute deviation from unity is greater than the total uncertainty, have an absolute deviation of < 0.5%.

The 10% surface dose increase caused by the parallel magnetic field, is accurately simulated using DOSXYZnrc. This surface dose increase is mainly due to the parallel fringe magnetic field confining contaminant electrons that originated in the linac head or in the irradiated air column, thus restricting their lateral scatter. Past the first few millimeters of the buildup region, the magnetic field is seen to have very little overall effect and the two depth dose curves are within 1% of each other.

When the polystyrene phantom's surface coincides with the center of the electromagnet, the additional 13 cm of irradiated air column is experiencing a relatively high magnetic field, above 0.13 T. As such, the surface dose increases by 30%, and the whole buildup region dose is increased by the parallel fringe magnetic field further concentrating contaminant electrons towards the center of the beam. Past d_{max}, the two depth dose curves are virtually identical, as most of the contaminant electrons have stopped and deposited their dose. The surface and buildup dose increase is again accurately modeled by DOSXYZnrc as presented in Figure 4.9, and all the simulated points are again within 1% of the measurements. The absolute differences between unity and the ratios of measured to simulated points are compared in the bottom two graphs to the estimated total uncertainty. Again, for most points this difference is within the uncertainty, and it is greater than the uncertainty by at most 0.5% for the remaining few points.

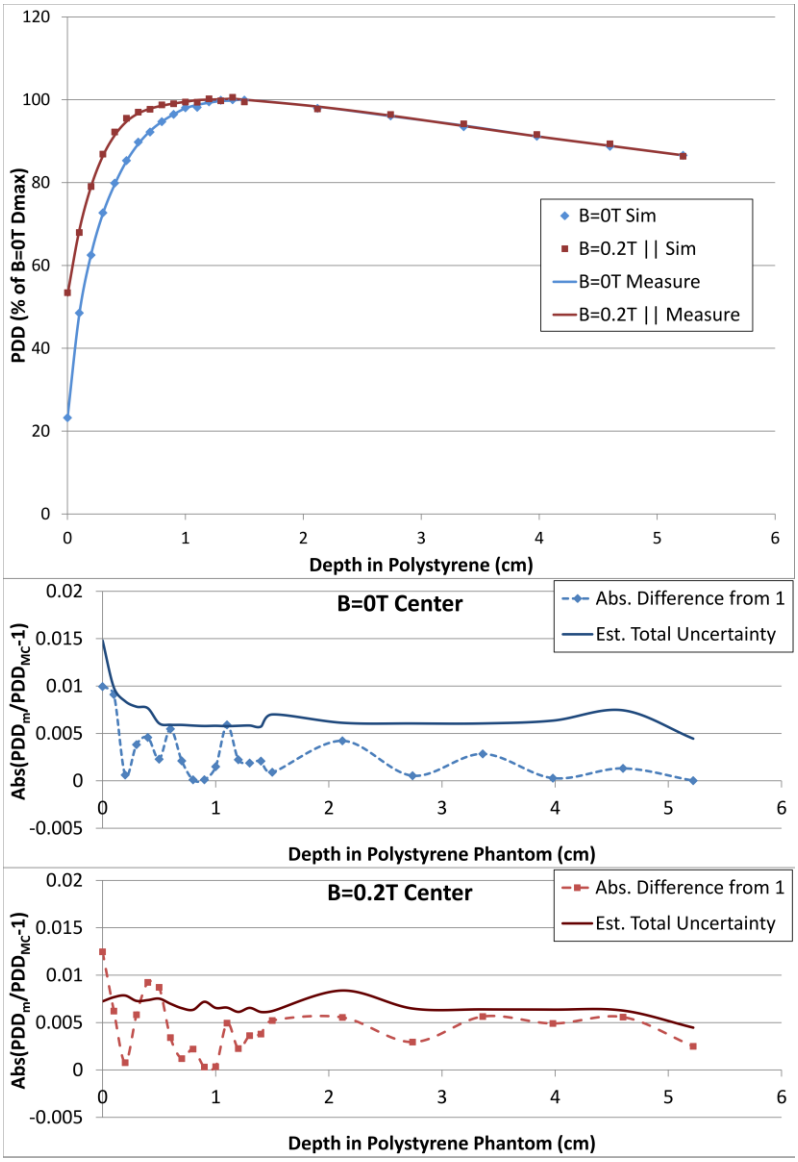

Figure 4.9 Measured and simulated PDD comparison for polystyrene phantom surface coinciding with center of the magnet (Figure 4.3, b). The absolute difference between the ratio of measurements and simulations, and unity is compared to the estimated total uncertainty for each curve separately.

Another effect that contributes to the surface dose increase for both setups is the convergence of the fringe magnetic field lines towards the symmetry axis of the electromagnet's bore. This symmetry axis was aligned with the central axis of the high energy photon beam. Thus, the contaminant electrons, which originate in the area of fringe magnetic field, are spiraling around the converging fringe magnetic field lines and are concentrated towards the

centre of the radiation beam. This is evident when simulating the surface beam profiles with and without the magnetic field for both experimental setups. Figure 4.10 shows the surface dose profiles simulated with the phantom top surface coinciding with the centre of the magnet. These profiles were calculated at the surface of the polystyrene phantom using $0.1 \times 0.1 \times 0.1$ cm^2 voxels. When the realistic parallel magnetic field is present (B=0.2T Real), the contaminant electrons increase the entrance surface dose particularly at the centre of the beam, causing the beam profile to no longer be flat. The dose increases at the beam edges as well, as an increased number of contaminant electrons reach the phantom surface under the influence of the parallel magnetic field.

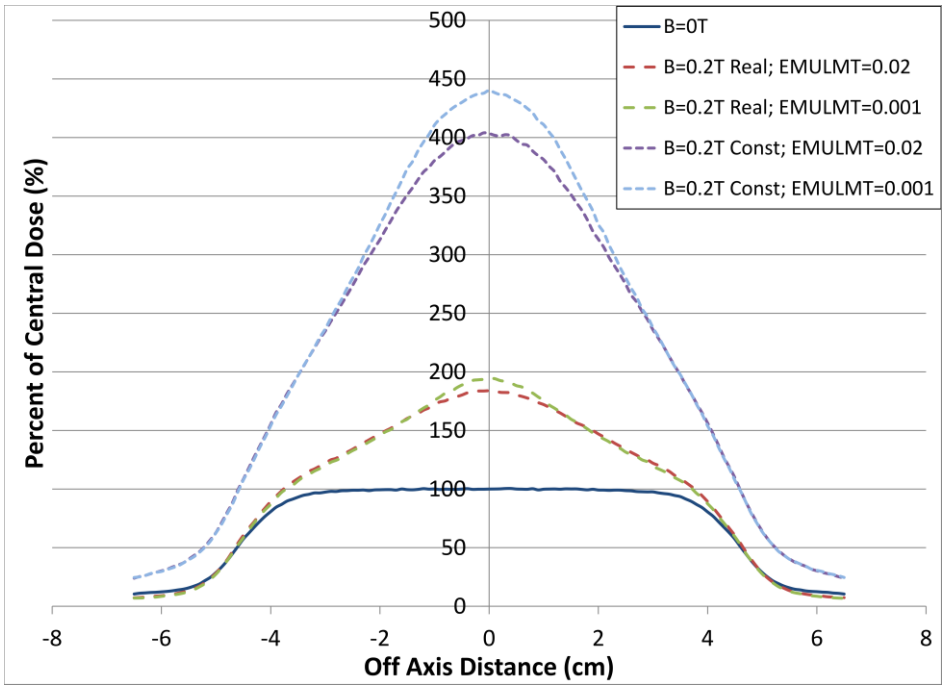

Figure 4.10 Simulated surface dose profile for polystyrene phantom surface coinciding with centre of the magnet: with no magnetic field, with the realistic magnetic field map (B=0.2T Real), and with a constant magnetic field (B=0.2T Const) calculated using both the default EMULMT=0.02, and then using EMULMT=0.001. The data was normalized to the no magnetic field central axis dose.

Figure 4.10 also shows a noticeable difference in the surface dose between the default value for EMULMT (0.02) and the smaller one (0.001) that was used for this study for the realistic magnetic field map (B=0.2 T Real). When using the default value, the step size is large enough to allow the contaminant electrons to have wider circular paths. As such fewer electrons reach the surface of the phantom close to the centre of the beam. When comparing surface dose measurements in the magnetic field with simulations that included the ion chamber air gap and polyethylene window, it was found that using the default EMULMT=0.02 would result in a 3% underestimation of the surface dose for this particular setup. The rest of the depth dose points simulated using EMULMT=0.02 were within 2% of the measurements.

Using exactly the same simulation setup, the surface dose profile was also calculated within a constant 0.207 T magnetic field, parallel to the beam central axis by replacing the experimental magnetic field map used before. Figure 4.10 shows the dose profiles within the constant magnetic field (B=0.2T Const) simulated using both the default EMULMT = 0.02 and the modified EMULMT = 0.001. The spatial extent of the constant magnetic field was the same as the one for the experimental magnetic field map (-50 cm to +50 cm in the x and y directions, and -182 cm to 20 cm in the z direction). Since the magnetic field is constant and parallel to the beam axis everywhere, the electrons from the phase space file are captured by the magnetic field and not allowed to scatter laterally, as soon as they enter the simulation space. Thus the resulting profiles are still peaked along the central axis. Using the modified EMULMT=0.001 again causes the captured electrons to have tighter spirals along the constant magnetic field lines, and thus increases the central dose by ~40% more than when using the default EMULMT =0.02.

The depth dose simulations were all run again using the magnetic field calculated with an iron cylinder in place of the linac head. The PDDs calculated in the presence of the magnetic

field with the iron cylinder in place were subtracted from the PDDs calculated in the presence of the magnetic field without the iron cylinder. The resulting difference is presented in Figure 4.11. For the setup where the surface of the polystyrene phantom coincides with the top of the electromagnet bore (Figure 4.3, a) the presence of the iron cylinder makes very little difference, with random variations <±1%. When the surface of the polystyrene phantom is in the centre of the bore, the depth dose values obtained with the iron cylinder in place tend to be slightly higher than the ones calculated without the iron. Still, the largest difference is <1%. Keeping in mind that the simulated PDD uncertainty for each point is on average 0.6% (with respect to D_{max}), which implies a 0.85% uncertainty for each difference curve presented in Figure 4.11, this shows that the presence of the ferromagnetic linac head can be ignored with minimal errors in the calculation of the depth dose profiles for both the setups investigated in the current study.

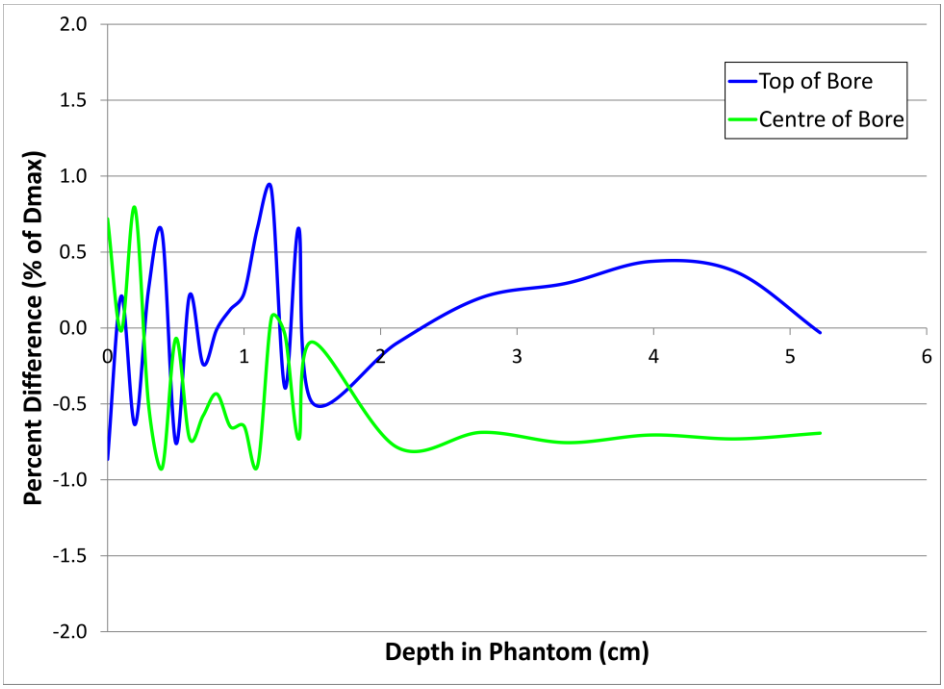

Figure 4.11 Difference between the PDDs simulated using the magnetic field with the iron plate and the magnetic field without the iron plate. 'Top of Bore' refers to the setup presented in Figure 4.3(a) and 'Center of Bore' to the setup in Figure 4.3(b).

4.3.4 Exit dose in parallel magnetic field

An exit dose point measurement was also performed with the polystyrene phantom as shown in Figure 4.3(a) but flipped upside down inside the magnet's bore. The ion chamber was also upside down with its entrance window flush with the exit surface of the phantom. With the magnetic field turned on, the exit dose was measured to be <0.05% (of D_{max} measured on the same day with the phantom right side up) higher than without the magnetic field, which is well within our experimental uncertainty. Since the Markus parallel plate ion chamber was not designed to be used upside down, further measurements with the ion chamber in this configuration were performed. It was found that measurements taken with the entrance window at the same depth but with the ion chamber upside down are between 1.3% (at depths > d_{max}) and 3.9% (depths ≤ d_{max}) lower than measurements taken with the ion chamber in the regular (right side up) orientation.

Simulations were also run with the ion chamber air cavity above the polyethylene entrance window at the bottom of the polystyrene phantom to emulate the upside down measurement setup. The calculated dose without magnetic field matched the measurement to within 1%, while the simulation with the magnetic field present was 1.3% higher than the measurement. Given that the measurements with the parallel plate ion chamber upside down are low, this slightly higher simulated value is to be expected.

4.4 Conclusion

Irradiation in the presence of a magnetic field parallel to the radiation beam's central axis, results in increased surface and buildup region doses. This increase was measured at two locations within the bore of an electromagnet: with the surface of the phantom at the same height

as the top of the bore, and with the surface of the phantom at the center of the magnet bore. Compared to the measurement without a magnetic field, the parallel magnetic field increases the surface dose by 10% (of D_{max}) when the phantom surface is at the same height as the top of the magnet bore, and by 30% when the phantom surface is at the center of the bore. This increase is due to two processes: the Lorentz force confining contaminant electrons to helical paths around the magnetic field lines, and the fringe magnetic field lines converging towards the magnet's axis of symmetry. The overall effect of the magnetic field used in this study is that the contaminant electrons are concentrated towards the centre of the beam which coincides with the electromagnet's symmetry axis.

By using a model of the linac benchmarked using commissioning measurements, and a FEM-generated 3D magnetic field map benchmarked against measurements, simulations of the measurement setup were performed using the EGSnrc Monte Carlo package. Depth dose profiles were scored in DOSXYZnrc with the 3D magnetic field implemented and without a magnetic field. We have shown the ferromagnetic linac head has a minimal impact on the simulated depth doses for this particular setup. The magnetic field is small enough at, and around the linac head (130 cm above the electromagnet center) such that the effects of the large ferromagnetic head can be ignored with minimal errors in the final PDD calculation. This also allows us to use the Sheikh-Bagheri et al. method for tuning the linac head parameters without any further modifications accounting for the presence of the magnetic field. By comparing the simulated PDD profiles with the measured profiles, we have shown that, with a few slight modifications, EGSnrc MC is capable of accurately simulating surface and buildup region dose effects caused by a realistic parallel magnetic field in homogeneous tissue-like phantoms.

4.5 References:

1. B.G. Fallone, B. Murray, S. Rathee, T. Stanescu, S. Steciw, S. Vidakovic, E. Blosser, and D. Tymofichuk, "First MR images obtained during megavoltage photon irradiation from a prototype integrated linac-MR system," Med. Phys. **36**(6), 2084–2088 (2009).

2. B.W. Raaymakers, J.J.W. Lagendijk, J. Overweg, J.G.M. Kok, A.J.E. Raaijmakers, E.M. Kerkhof, R.W. van der Put, I. Meijsing, S.P.M. Crijns, F. Benedosso, M. van Vulpen, C.H.W. de Graaff, J. Allen, and K.J. Brown, "Integrating a 1.5 T MRI scanner with a 6 MV accelerator: proof of concept.," Phys. Med. Biol. **54**(12), N229–N237 (2009).

3. B.M. Oborn, S. Kolling, P.E. Metcalfe, S. Crozier, D.W. Litzenberg, and P.J. Keall, "Electron contamination modeling and reduction in a 1 T open bore inline MRI-linac system.," Med. Phys. **41**(5), 1–15 (2014).

4. C. Kirkby, B. Murray, S. Rathee, and B.G. Fallone, "Lung dosimetry in a linac-MRI radiotherapy unit with a longitudinal magnetic field," Med. Phys. **37**(9), 4722–4732 (2010).

5. A. Keyvanloo, B. Burke, J.S. Aubin, D. Baillie, K. Wachowicz, B. Warkentin, S. Steciw, and B.G. Fallone, "Minimal skin dose increase in longitudinal rotating biplanar linac-MR systems : examination of radiation energy and flattening filter design," Phys. Med. Biol. **61**, 3527–3539 (2016).

6. D.M. Santos, J. St. Aubin, B.G. Fallone, and S. Steciw, "Magnetic shielding investigation for a 6 MV in-line linac within the parallel configuration of a linac-MR system," **39**(February), 788–797 (2012).

7. B.W. Raaymakers, A.J.E. Raaijmakers, A.N.J. Kotte, D. Jette, and J.J.W. Lagendijk, "Integrating a MRI scanner with a 6 MV radiotherapy accelerator: dose deposition in a transverse magnetic field," Phys. Med. Biol. **49**, 4109–4118 (2004).

8. A.J.E. Raaijmakers, B.W. Raaymakers, and J.J.W. Lagendijk, "Integrating a MRI scanner with a 6 MV radiotherapy accelerator: dose increase at tissue-air interfaces in a lateral magnetic field due to returning electrons.," Phys. Med. Biol. **50**(7), 1363–1376 (2005).

9. A.J.E. Raaijmakers, B.W. Raaymakers, and J.J.W. Lagendijk, "Magnetic-field-induced dose effects in MR-guided radiotherapy systems: dependence on the magnetic field strength," Phys. Med. Biol. **53**(4), 909–923 (2008).

10. C. Kirkby, T. Stanescu, S. Rathee, M. Carlone, B. Murray, and B.G. Fallone, "Patient dosimetry for hybrid MRI-radiotherapy systems," Med. Phys. **35**(3), 1019–1027 (2008).

11. B.M. Oborn, P.E. Metcalfe, M.J. Butson, a. B. Rosenfeld, and P.J. Keall, "Electron contamination modeling and skin dose in 6 MV longitudinal field MRIgRT: Impact of the MRI and MRI fringe field," Med. Phys. **39**(2), 874–890 (2012).

12. I.J. Chetty, B. Curran, J.E. Cygler, J.J. Demarco, G. Ezzell, B.A. Faddegon, P.J. Keall, H. Liu, C.C. Ma, D.W.O. Rogers, J. Seuntjens, D. Sheikh-, J. V Siebers, and H. Liu, "Report of the AAPM Task Group No . 105 : Issues associated with clinical implementation of Monte Carlo-based photon and electron external beam treatment planning," Med. Phys. **34**(12), 4818–4853 (2007).

13. B.M. Oborn, P.E. Metcalfe, M.J. Butson, and a B. Rosenfeld, "Monte Carlo characterization of skin doses in 6 MV transverse field MRI-linac systems: effect of field

size, surface orientation, magnetic field strength, and exit bolus.," Med. Phys. **37**(10), 5208–5217 (2010).

14. A.J.E. Raaijmakers, B.W. Raaymakers, and J.J.W. Lagendijk, "Experimental verification of magnetic field dose effects for the MRI-accelerator.," Phys. Med. Biol. **52**(14), 4283–4291 (2007).

15. A. Keyvanloo, B. Burke, B. Warkentin, T. Tadic, S. Rathee, C. Kirkby, D.M. Santos, and B.G. Fallone, "Skin dose in longitudinal and transverse linac-MRIs using Monte Carlo and realistic 3D MRI field models," Med. Phys. **39**(10), 6509–6521 (2012).

16. M. Reynolds, B.G. Fallone, and S. Rathee, "Dose response of selected solid state detectors in applied homogeneous transverse and longitudinal magnetic fields," Med. Phys. **41**(9), 1–12 (2014).

17. M. Reynolds, B.G. Fallone, and S. Rathee, "Dose response of selected ion chambers in applied homogeneous transverse and longitudinal magnetic fields," Med. Phys. **40**(4), 1–7 (2013).

18. V.N. Malkov and D.W.O. Rogers, "Charged particle transport in magnetic fields in EGSnrc," Med. Phys. **43**(7), 4447–4458 (2016).

19. I. Meijsing, B.W. Raaymakers, A.J.E. Raaijmakers, J.G.M. Kok, L. Hogeweg, B. Liu, and J.J.W. Lagendijk, "Dosimetry for the MRI accelerator : the impact of a magnetic field on the response of a Farmer NE2571 ionization chamber," Phys. Med. Biol. **54**, 2993–3002 (2009).

20. S.L. Hackett, B. Van Asselen, J.W.H. Wolthaus, J.G.M. Kok, S.J. Woodings, J.J.W.

Lagendijk, and B.W. Raaymakers, "Consequences of air around an ionization chamber : Are existing solid phantoms suitable for reference dosimetry on an MR-linac?," Med. Phys. **43**(7), 3961–3968 (2016).

21. D.W.O. Rogers, B. Walters, and I. Kawrakow, *BEAMnrc Users Manual NRCC Report PIRS-0509(A)revL* (Ottawa, 2011).

22. B. Walters, I. Kawrakow, and D.W.O. Rogers, *DOSXYZnrc Users Manual NRCC Report PIRS-794revB* (Ottawa, 2011).

23. D. Sheikh-Bagheri and D.W.O. Rogers, "Sensitivity of megavoltage photon beam Monte Carlo simulations to electron beam and other parameters," Med. Phys. **29**(3), 379–390 (2002).

24. D.A. Low, W.B. Harms, S. Mutic, and J.A. Purdy, "A technique for the quantitative evaluation of dose distributions," Med. Phys. **25**(5), 656–661 (1998).

25. H.W. Koch and J.W. Motz, "Bremsstrahlung Cross-Section Formulas and Related Data," Rev. Mod. Phys. **31**(4), 920–955 (1959).

26. A.F. Bielajew, "The effect of strong longitudinal magnetic fields on dose deposition from electron and photon beams.," Med. Phys. **20**(4), 1171–1179 (1993).

27. A.F. Bielajew, "Electron transport in E and B Fields," in *Monte Carlo Transp. Electrons Photons*, edited by T.M. Jenkins, W.R. Nelson, A. Rindi, A.E. Nahum and D.W.O. Rogers (Plenum Press, New York, 1989), pp. 421 – 434.

28. D. Sheikh-Bagheri, D.W.O. Rogers, C.K. Ross, and J. Seuntjens, "Comparison of measured and Monte Carlo calculated dose distributions from the NRC linac," Med.

Phys. **27**(10), 2256–2266 (2000).

29. H. Bouchard, J. De Pooter, A. Bielajew, and S. Duane, "Reference dosimetry in the presence of magnetic fields: Conditions to validate Monte Carlo simulations," Phys. Med. Biol. 60(17), 6639–6654 (2015).

Chapter 5: Experimental Verification of EGSnrc with a Parallel Magnetic Field in a Lung Phantom

A version of this chapter has been submitted for publication as: Andrei Ghila, B.Gino Fallone, Satyapal Rathee ***Technical Note: Experimental verification of EGSnrc calculated depth dose within a parallel magnetic field in a lung phantom,*** *2018.*

5.1 Introduction

Integrating a clinical linear accelerator (linac) with a magnetic resonance imager (MRI) has the potential of delivering radiation to a tumor with increased accuracy[1–3] compared to conventional treatments, by allowing health care professionals to visualize the tumor during irradiation. As discussed in previous chapters, such an integrated linac-MR unit will deliver a modified dose when compared to a conventional radiation treatment whether the main magnetic field is transverse or parallel to the radiation beam's central axis[4–11].

These dose modifications have previously been investigated mainly using Monte Carlo (MC) simulations. The MC packages capable of integrating magnetic field effects into their charged particle transport that have been used so far are: Geant4[3,5,12,13], EGSnrc[7,8,11,14] and PENELOPE[15,16]. While Geant4 dose calculations in the presence of a magnetic field have been previously verified experimentally[13,17] for multiple materials, to date, EGSnrc MC has only been recently experimentally verified in a polystyrene phantom,[10] as shown in the previous chapter. The current chapter aims to extend the experimental verification of EGSnrc with a magnetic field parallel to the radiation beam central axis to lung-like materials as well.

5.2 Materials and Methods:

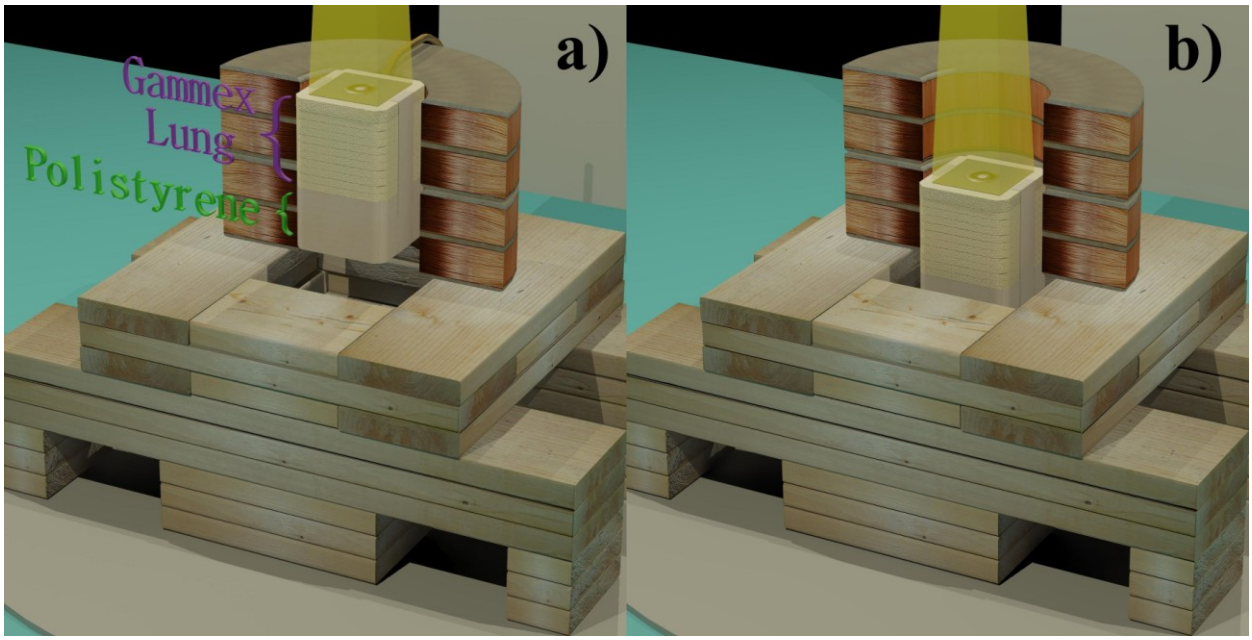

Figure 5.1 The measurement setup with the two GMW electromagnets (shown in cross section) placed on a wooden stand. The Gammex lung phantom with the polystyrene bottom (indicated in the figure) was positioned with its top surface coinciding with the top of the electromagnet (a), then with its top surface coinciding with the centre of the electromagnet (b).

The experimental setup, shown in Figure 5.1, consisted of two GMW electromagnets (3472-70, GMW Associates, San Carlos, CA) stacked, one on top of the other, and an in-house built wooden stand that supported the two electromagnets. This electromagnet configuration provided a magnetic field parallel to the central axis of a Varian Silhouette linac. The maximum magnetic field strength was measured to be 0.207 T at the centre of the common bore. The depth dose measurements were acquired using a specially designed phantom that consisted of 1.0 cm, and 1.5 cm thick sheets of lung material (GAMMEX RMI, Middleton, WI). The two thicknesses of Gammex lung material were cut into 13x13 cm^2 sheets, and were replaced from above to below the ion chamber insert in such a way as to provide a depth dose measurement at every 0.5 cm depth interval. Polystyrene rails attached to 10 cm of polystyrene backscatter held the lung

(17.5 cm total thickness) in place, while allowing for a reproducible placement of the ion chamber insert at each depth.

The ion chamber insert was built using one of the 1.5 cm thick Gammex lung sheets, machined to tightly fit a Markus (PTW, Freiburg, Germany) parallel plate ion chamber (ppic). This ppic was chosen for its small size, and has a thin 0.03 mm polyethylene entrance window, 5.3 mm diameter collecting electrode, and a 2 mm electrode separation with the sensitive volume vented to the atmosphere. The air cavity and entrance window are embedded in a 30.0 mm diameter acrylic body that goes around and below the sensitive air volume, leaving the entrance window flush with the top. The ion chamber and sheet combination were stepped down through the stack of lung material measuring the depth dose from the surface of the phantom to a depth of 10 cm.

The measurements in the Gammex lung phantom were performed with the entire phantom placed at two separate locations within the electromagnets' bore: top surface of the phantom coinciding with the top of the electromagnet (Figure 5.1(a)), and top surface of the phantom coinciding with the centre of the electromagnet bore (Figure 5.1(b)). A 6 MV beam with 5×5 cm^2 field size at the isocenter was used for both setups, which became 8.5×8.5 cm^2 on the surface of the phantom at a source to surface distance (SSD) of 170 cm (Figure 5.1(a) setup), and of 9.2×9.2 cm^2 on the surface of the phantom at an SSD of 183 cm (Figure 5.1(b) setup).

For the Monte Carlo simulations, DOSXYZnrc was modified[10] as described in the previous chapter to read the 3D magnetic field. The standard magnetic field implementation, based on the work by A. F. Bielajew[18,19], already present in the macro package emf_macros, was used but with a shorter particle step size. The particle step size was shortened by reducing the

parameter responsible for controlling the amount of deflection in the electromagnetic field (EMULMT) from the default 0.02 to 0.001. With the reduced step size and using the default condensed history technique, this implementation is expected to pass the Fano cavity test as it is similar to one of the cases investigated by Malkov and Rogers[17]. Shortening the step size in this manner has been shown in the previous chapter to result in magnetic field dose simulations more accurately matching our polystyrene measurements[10]. The phase space file benchmarked in Chapter 4 represented the 6 MV beam of the Varian Silhouette unit and was used as the source in the DOSXYZnrc simulations. COMSOL Multiphysics V4.4 (Burlington, MA) calculated the 3D magnetic field map that was benchmarked against measurements in the previous chapter.

The standard EGSnrc lung material (LUNG521ICRU) was used to simulate the Gammex lung slabs. The simulated phantom was composed of lung (13x13x18 cm^3) followed by 10 cm of polystyrene (between 18 cm and 28 cm depth). However, running the simulations in a phantom composed entirely of lung did not have any noticeable effect on the simulated depth dose between 0 cm (surface) and 10 cm depth. The simulations were run similarly to the ones in polystyrene[10] with an air cavity and polyethylene entrance window ($0.53\times0.53\times0.2$ cm^3 and $0.53\times0.53\times0.003$ cm^3 respectively) approximating the Markus parallel plate chamber dimensions, and scoring the dose to the air cavity. The circular dimensions of the ion chamber components were approximated in the lateral (x and y) directions since DOSXYZnrc can only model rectangular geometry. The chamber dimensions in the depth (z) direction however were modeled exactly. This method of approximating the cylindrical geometry of the ion chamber with a cubical one has yielded good results for the work described in the previous chapter. The air cavity and polyethylene entrance window were stepped down through the simulated lung phantom much the same way as the ion chamber insert was stepped for the measurements.

5.3 Results and Discussion:

Figure 5.2 presents the difference between the measurement and simulation for both setups as a percentage of the no magnetic field maximum dose (D_{max}) for each individual setup. At the surface the simulated dose is lower than the measured one, particularly without the magnetic field, for both experimental setups. However deeper in the phantom, the simulated dose is higher than the measurement by up to 2.5%, especially with a magnetic field present.

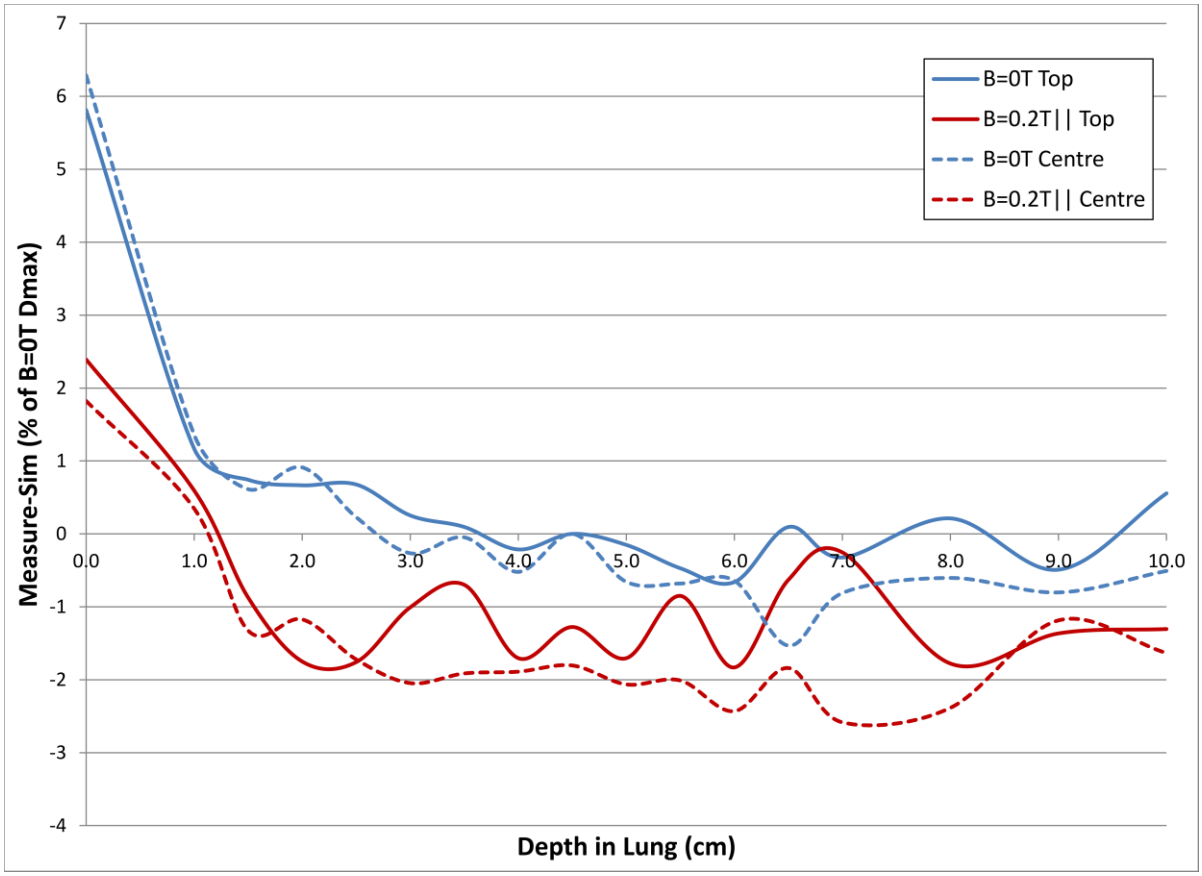

Figure 5.2 Difference between the measured and simulated depth doses in lung when simulations included only the air cavity and entrance window of the ion chamber.

Therefore, when the ion chamber is at the surface, there are fewer electrons traversing the air cavity in the EGSnrc simulation, compared to the measurements, both with and without the

magnetic field. However, at deeper locations within the phantom, more electrons deposit dose in the air cavity for the simulations compared to measurements, particularly when the magnetic field is present. This may be caused by not explicitly simulating the integral acrylic body of the ion chamber. For simulating the depth dose in polystyrene, modeling the air cavity and entrance window was enough to match measurements and simulations[10], since the electron density of polystyrene and acrylic are close to each other. Thus, all our subsequent lung simulations included the acrylic body of the ion chamber as a $2.7\times2.7\times1.4$ cm^3 volume around and below the air cavity. Since acrylic is not a standard material in EGSnrc, the 521icru.pegs4dat file was appended to include the cross sectional data for acrylic[20].

Figure 5.3 shows the comparison between the measured (solid lines) and the simulated (points) depth dose for the setup presented in Figure 5.1(a), where the surface of the lung phantom coincides with the top of the electromagnet. The data markers are larger than the statistical uncertainty for all the simulated points. In the lower half of Figure 5.3, the absolute percent difference (with respect to no magnetic field D_{max}) between measurements and simulations is presented separately for the two depth doses (B = 0 T and B = 0.2 T).

With the acrylic body of the ion chamber included, the EGSnrc Monte Carlo is able to accurately calculate the dose measured in lung material in the presence of a parallel magnetic field with most simulated points falling within 1.5% of the measurements. The largest difference is 1.8% for the depth dose with the magnetic field turned on. Both measurements and simulations show a surface dose increase of ~11% in the lung material due to the parallel magnetic field.

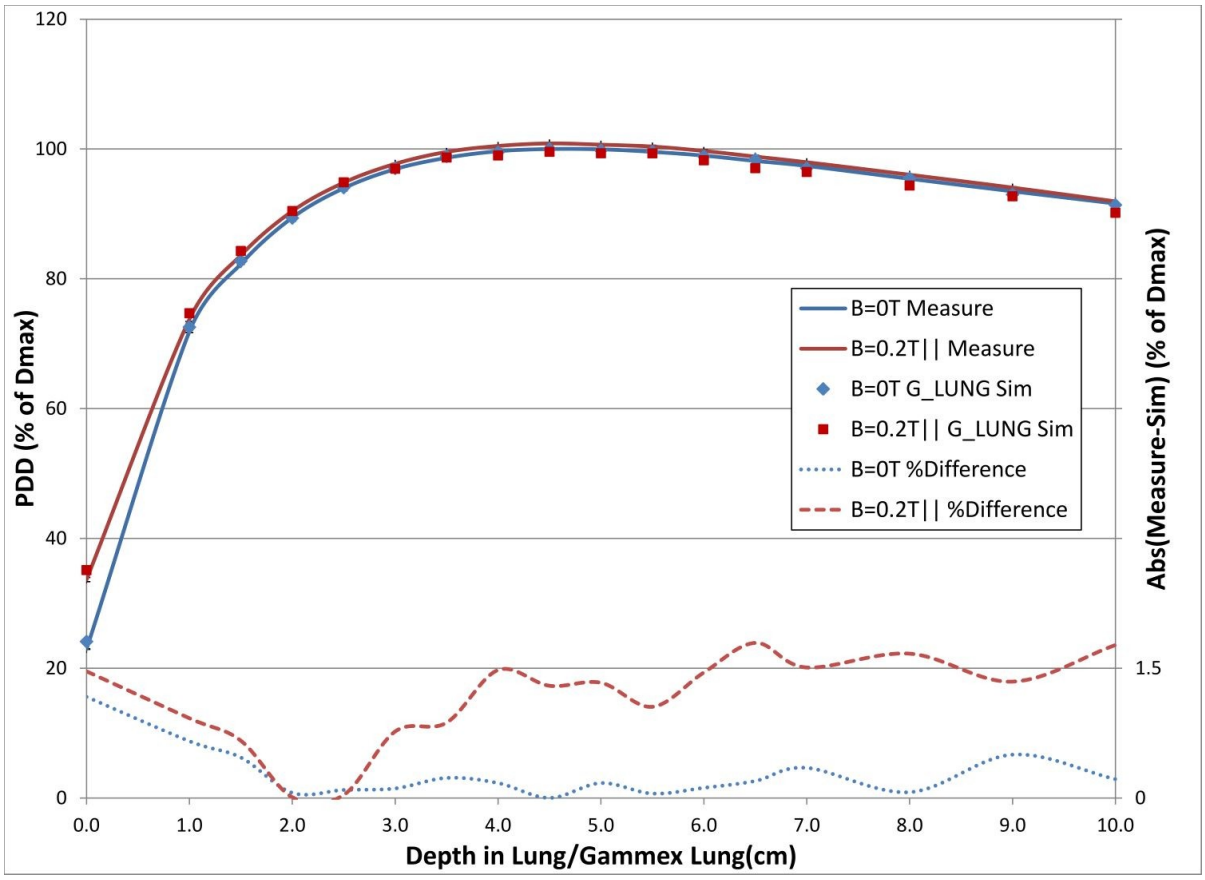

Figure 5.3 Measured and simulated depth dose comparison for Gammex lung phantom surface coinciding with the top of the magnet [see Figure 5.1(a)]. The absolute percent difference (with respect to D_{max}) between measurements and simulations, for both with and without magnetic field, is presented at the bottom of the graph. These simulations included the acrylic body of the ion chamber.

This increase in the surface dose is due in part to contaminant electrons originating in the linac head and in the irradiated air column having their lateral spread confined by the parallel magnetic field. As previously discussed, for our particular setup the fringe magnetic field lines also converge towards the central axis of the electromagnet bore, thus the contaminant electrons are concentrated towards the center of the beam that was aligned with the central axis of the magnet. Past the first centimeter of the buildup region, these contaminant electrons have mostly been absorbed in the lung material and the two depth dose curves, with and without the magnetic

field, are within <2% of each other for both measurements and simulations. There is also no significant difference in the depth of maximum dose, caused by the magnetic field, for this setup.

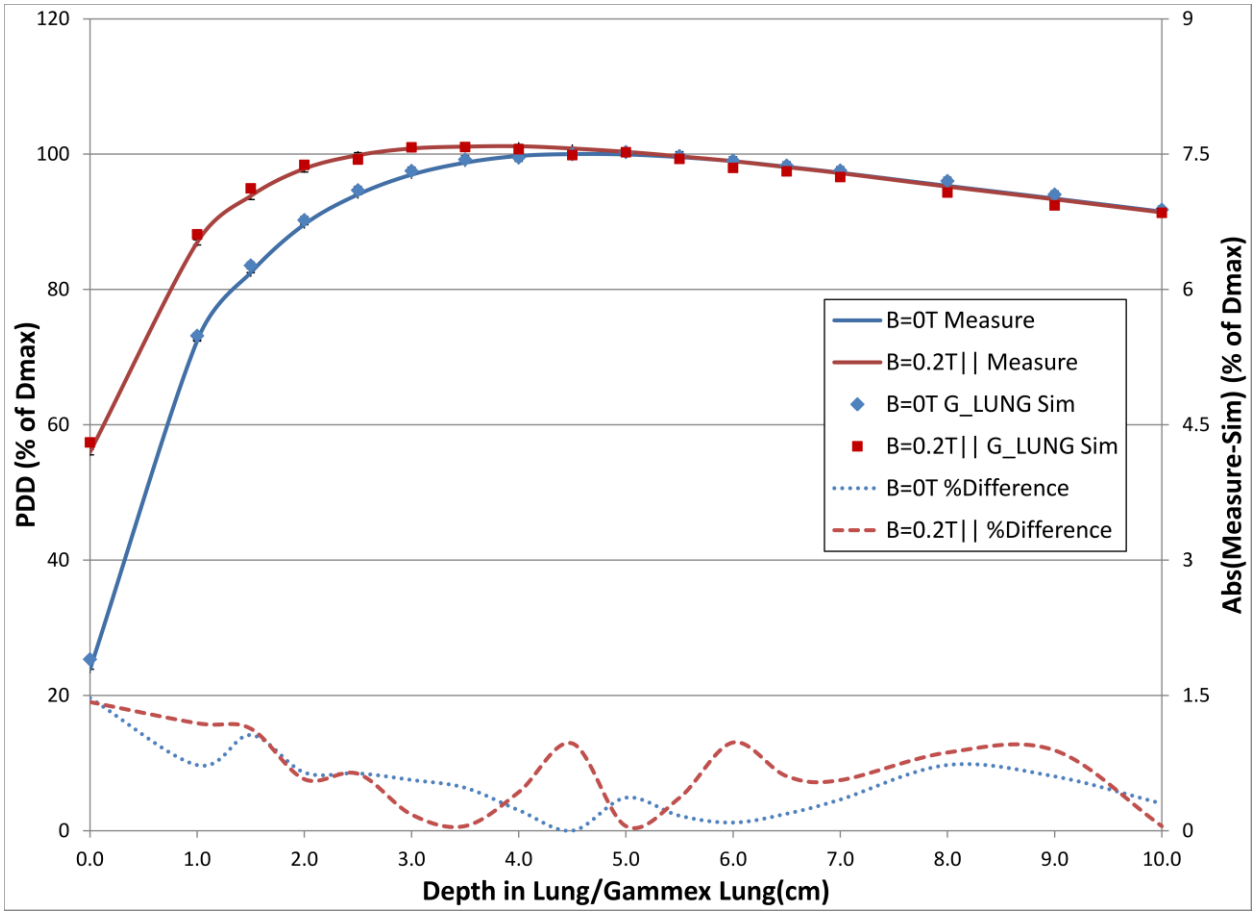

Figure 5.4 Measured and simulated depth dose comparison for Gammex lung phantom surface coinciding with the centre of the magnet [see Figure 5.1(b)]. The absolute percent difference (with respect to D_{max}) between measurements and simulations, for both with and without magnetic field, is presented at the bottom of the graph. These simulations included the acrylic body of the ion chamber.

The measurements and simulations for the setup presented in Figure 5.1(b), where the surface of the lung phantom coincides with the centre of the magnet, are compared in Figure 5.4. As before, the lower half of the graph presents the absolute differences between measurements and simulations for both (with and without magnetic field) depth dose curves. EGSnrc is able to accurately calculate the dose in lung with a parallel magnetic field for this setup as well, with all

the simulated points agreeing with the measurements to within <1.5 %. The highest percent difference between measurements and simulations is at the surface irrespective of magnetic field. Both the measurements and the simulations show a surface dose increase of ~32% (with respect to no magnetic field D_{max}) caused by the presence of the parallel magnetic field.

The higher surface dose increase, compared to the previous setup, is caused by the additional air column being irradiated in relatively high (>0.13 T) magnetic field and by the converging magnetic field lines further concentrating contaminant electrons towards the centre of the beam. For this setup the entire buildup region is affected by the magnetic field, with the two depth dose curves becoming indistinguishable only past the depth of maximum dose. Additionally, for this setup, the magnetic field makes the depth of maximum dose slightly shallower in both the measurements and the simulations.

In a clinical scenario, to get to the lung tissue, the radiation has to pass through denser tissue first. Thus, the lung will most likely be close to or past the depth of maximum dose (d_{max}). To investigate if any magnetic field dose effects would be present at the tissue/lung interface due to a 0.21 T parallel magnetic field, the depth dose was measured in an inhomogeneous phantom. Using the setup from Figure 5.1, a) the phantom was loaded with 3.5 cm of polystyrene followed by 11.5 cm of Gammex lung, and finally 13.0 cm polystyrene backscatter. The central axis dose measured with the Markus ion chamber is plotted in Figure 5.5 both with the electromagnet turned off, and with the electromagnet turned on. These measurements showed no magnetic field dose effects at the polystyrene/lung or lung/polystyrene interfaces. The only difference was the increase in surface and buildup dose in the top polystyrene layer, consistent to the results presented in Chapter 4. Thus in a clinical scenario, where the lung is at a depth beyond d_{max}, no

dose increases like the ones visible in Figure 5.3 and Figure 5.4 are expected at the tissue/lung or lung/tissue interface.

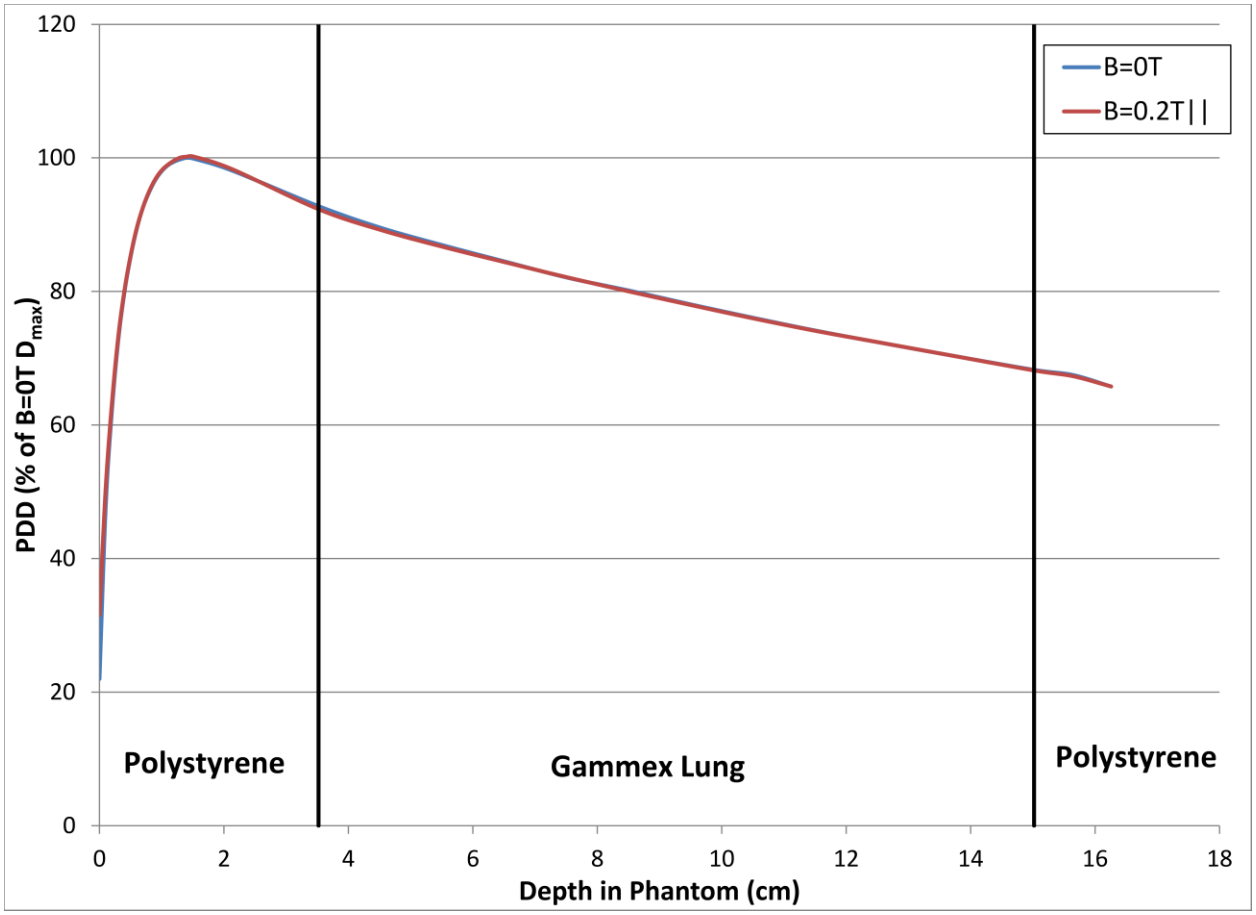

Figure 5.5 Depth dose measurements in an inhomogeneous (polystyrene, Gammex Lung, polystyrene) phantom for a 8.5×8.5 cm^2 field size. Other than the surface dose difference, the magnetic field does not induce any other effects measurable with our setup.

5.4 Conclusion:

The dose in the Gammex lung-like material has been measured in the presence of a magnetic field parallel to the central axis of the radiation beam using a PTW Markus parallel plate ion chamber. The measurements were compared to EGSnrc Monte Carlo simulations performed in regular lung. It was found that the simulations needed to include a rough model of

all the ion chamber components (polyethylene entrance window, air cavity, as well as the acrylic ion chamber body) for a better match with the measurements. EGSnrc was able to accurately calculate the dose in lung in the presence of a realistic parallel magnetic field at two different locations within the electromagnet bore. All the simulated points were within 2% (with respect to no magnetic field D_{max}) of the measurements, with the majority falling within less than 1.5%.

5.5 References:

1. B.G. Fallone, B. Murray, S. Rathee, T. Stanescu, S. Steciw, S. Vidakovic, E. Blosser, and D. Tymofichuk, "First MR images obtained during megavoltage photon irradiation from a prototype integrated linac-MR system," Med. Phys. **36**(6), 2084–2088 (2009).

2. B.W. Raaymakers, J.J.W. Lagendijk, J. Overweg, J.G.M. Kok, A.J.E. Raaijmakers, E.M. Kerkhof, R.W. van der Put, I. Meijsing, S.P.M. Crijns, F. Benedosso, M. van Vulpen, C.H.W. de Graaff, J. Allen, and K.J. Brown, "Integrating a 1.5 T MRI scanner with a 6 MV accelerator: proof of concept.," Phys. Med. Biol. **54**(12), N229–N237 (2009).

3. B.M. Oborn, S. Kolling, P.E. Metcalfe, S. Crozier, D.W. Litzenberg, and P.J. Keall, "Electron contamination modeling and reduction in a 1 T open bore inline MRI-linac system.," Med. Phys. **41**(5), 1–15 (2014).

4. B.W. Raaymakers, A.J.E. Raaijmakers, A.N.J. Kotte, D. Jette, and J.J.W. Lagendijk, "Integrating a MRI scanner with a 6 MV radiotherapy accelerator: dose deposition in a transverse magnetic field," Phys. Med. Biol. **49**, 4109–4118 (2004).

5. A.J.E. Raaijmakers, B.W. Raaymakers, and J.J.W. Lagendijk, "Integrating a MRI scanner with a 6 MV radiotherapy accelerator: dose increase at tissue-air interfaces in a lateral magnetic field due to returning electrons.," Phys. Med. Biol. **50**(7), 1363–1376 (2005).

6. A.J.E. Raaijmakers, B.W. Raaymakers, and J.J.W. Lagendijk, "Magnetic-field-induced dose effects in MR-guided radiotherapy systems: dependence on the magnetic field strength," Phys. Med. Biol. **53**(4), 909–923 (2008).

7. C. Kirkby, T. Stanescu, S. Rathee, M. Carlone, B. Murray, and B.G. Fallone, "Patient

dosimetry for hybrid MRI-radiotherapy systems," Med. Phys. **35**(3), 1019–1027 (2008).

8. A. Keyvanloo, B. Burke, B. Warkentin, T. Tadic, S. Rathee, C. Kirkby, D.M. Santos, and B.G. Fallone, "Skin dose in longitudinal and transverse linac-MRIs using Monte Carlo and realistic 3D MRI field models," Med. Phys. **39**(10), 6509–6521 (2012).

9. B.M. Oborn, P.E. Metcalfe, M.J. Butson, a. B. Rosenfeld, and P.J. Keall, "Electron contamination modeling and skin dose in 6 MV longitudinal field MRIgRT: Impact of the MRI and MRI fringe field," Med. Phys. **39**(2), 874–890 (2012).

10. A. Ghila, S. Steciw, B.G. Fallone, and S. Rathee, "Experimental verification of EGSnrc Monte Carlo calculated depth doses within a realistic parallel magnetic field in a polystyrene phantom," Med. Phys. **44**(9), 4804–4815 (2017).

11. A. Keyvanloo, B. Burke, J.S. Aubin, D. Baillie, K. Wachowicz, B. Warkentin, S. Steciw, and B.G. Fallone, "Minimal skin dose increase in longitudinal rotating biplanar linac-MR systems : examination of radiation energy and flattening filter design," Phys. Med. Biol. **61**, 3527–3539 (2016).

12. B.M. Oborn, P.E. Metcalfe, M.J. Butson, and a B. Rosenfeld, "Monte Carlo characterization of skin doses in 6 MV transverse field MRI-linac systems: effect of field size, surface orientation, magnetic field strength, and exit bolus.," Med. Phys. **37**(10), 5208–5217 (2010).

13. A.J.E. Raaijmakers, B.W. Raaymakers, and J.J.W. Lagendijk, "Experimental verification of magnetic field dose effects for the MRI-accelerator.," Phys. Med. Biol. **52**(14), 4283–4291 (2007).

14. C. Kirkby, B. Murray, S. Rathee, and B.G. Fallone, "Lung dosimetry in a linac-MRI radiotherapy unit with a longitudinal magnetic field," Med. Phys. **37**(9), 4722–4732 (2010).

15. M. Reynolds, B.G. Fallone, and S. Rathee, "Dose response of selected ion chambers in applied homogeneous transverse and longitudinal magnetic fields," Med. Phys. **40**(4), 1–7 (2013).

16. M. Reynolds, B.G. Fallone, and S. Rathee, "Dose response of selected solid state detectors in applied homogeneous transverse and longitudinal magnetic fields," Med. Phys. **41**(9), 1–12 (2014).

17. V.N. Malkov and D.W.O. Rogers, "Charged particle transport in magnetic fields in EGSnrc," Med. Phys. **43**(7), 4447–4458 (2016).

18. A.F. Bielajew, "The effect of strong longitudinal magnetic fields on dose deposition from electron and photon beams.," Med. Phys. **20**(4), 1171–1179 (1993).

19. A.F. Bielajew, "Electron transport in E and B Fields," in *Monte Carlo Transp. Electrons Photons*, edited by T.M. Jenkins, W.R. Nelson, A. Rindi, A.E. Nahum and D.W.O. Rogers (Plenum Press, New York, 1989), pp. 421 – 434.

20. I. Kawrakow, E. Mainegra-Hing, D.W.O. Rogers, F. Tessier, and B.R.B. Walters, *The EGSnrc Code System : Monte Carlo Simulation of Electron and Photon Transport* (NRC Canada, 2011).

Chapter 6: Summary and Conclusions

Cancer is a rather ubiquitous disease expected to affect roughly half the population of Canada within their lifetime. Radiation therapy is one of the main modalities currently used to treat cancer. The goal of radiation therapy is to deliver as much dose as possible to the cancer tumour while at the same time delivering the minimal amount of dose to the surrounding healthy tissue. For this to be possible, a precise localization of the tumour, surrounding structures, and OARs is extremely important. Although, various imaging methods are being routinely used to reduce the PTV geometric margin, which accounts for setup and movement uncertainty, none of them can visualize the treated volume during irradiation. An integrated linac-MR system is capable of achieving real-time tumour visualization during the radiation treatment, however irradiating a patient during MR imaging presents several challenges.

The work presented in this thesis focused on an area where little to no experimental investigation previously existed, namely the surface and buildup dose modifications that arise when irradiating a patient inside an MRI. The RF coils, necessary for MRI image acquisition, would be in the radiation beam path when used in a linac-MR, given current coil designs. We have experimentally investigated and quantified how various RF coil materials will modify the radiation dose of the surface and in the buildup region. Secondly, the magnetic field parallel to the radiation beam central axis also modifies the surface and build up dose. We measured depth doses, in polystyrene (as a substitute for soft tissue) and lung, in the presence of a parallel magnetic field, and verified the accuracy of dose calculated by the EGSnrc Monte Carlo system against these measurements.

To quantify the patients' surface and buildup dose modifications caused by the high energy photon beam passing through the MRI's RF coil, we investigated several standard, off-the-shelf, RF coil materials. A surface RF coil was approximated by layers of polycarbonate, copper tape, and Teflon to emulate the base, conductor and cover respectively. This imitation RF coil was placed at various distances (between 0 cm to 10 cm) away from the surface of polystyrene phantoms. For each distance between the coils and phantom, we measured the surface and buildup doses without magnetic field, with a parallel magnetic field, and with a transverse magnetic field present. The placement of the imitation RF coil in direct contact with the phantom surface increased the surface dose, from ~20% to ~75% of the maximum dose D_{max}, whether the magnetic field was present or not, or whether it was parallel or transverse. The measured dose increased in the entire buildup region with the largest increase being on the surface. Clearly, the imitation RF coil acts as a bolus and increases the effective depth of the phantom's surface. Creating a separation between the coil and the phantom's surface mitigates the dose increase when no magnetic field is present. The surface dose decreased with increasing separation as the electrons created in the imitation RF coil had time to scatter laterally before reaching the phantom. However, the surface dose was still ~40% of D_{max} even for a 10 cm separation. When the experiment was repeated in a transverse magnetic field, the surface dose decreased faster with increasing coil to surface separation. The surface dose was slightly less than 40% for a separation of only 3 cm. The ERE, caused by the transverse magnetic field, turns the electrons produced in the imitation RF coil away from the phantom's surface. For a given transverse magnetic field, and a non-surface RF coil, one can always adequately separate the coil from the phantom's surface such that the RF coil does not increase the surface dose. In a parallel magnetic field, increasing the separation between the coil and the surface of the phantom makes

virtually no difference on the surface dose, up to a separation of 3 cm, with only a slight decrease for a 10 cm separation. In this case, the electrons produced by the high energy photons in the imitation RF coil had their lateral spread confined by the parallel magnetic field. As such, most of the electrons produced in the RF coil materials reached the surface of the phantom and contributed to the surface dose even for a 10 cm coil to surface separation.

The effect of the radiation field size was also briefly investigated with the imitation RF coil in the beam and with no magnetic field. It was found that, for the smaller field sizes, the surface dose decreased faster with increasing surface to coil separation. Given the previous observations, we can infer that for a transverse magnetic field the surface dose will decrease even faster with increasing phantom-coil separation for the smaller field sizes. However, in a parallel magnetic field, the effect of reducing the field size on surface dose will likely be minimal while increasing the phantom-coil separation.

The surface dose was also measured with other typical RF coil materials placed in the path of the beam at various distances from the surface of the phantom. The results followed the same trends observed from the imitation RF coil measurements, irrespective of material. The surface dose decreased with increasing separation when there was no magnetic field present, decreased faster when a transverse magnetic field was present, and did not decrease appreciably when a parallel magnetic field was used. With the coil materials in direct contact with the surface of the phantom, the highest surface dose (~85% of D_{max}) was caused by a sheet of RF coil plastic cover. Typical RF coil foam padding caused the surface dose to increase to ~62%, and even a thin (0.1 mm) sheet of copper, typically used as the conductor in RF coils, brought the surface dose up to ~45%.

Thus, a considerable surface and buildup dose increase can be measured, when irradiating through typical RF coil materials. Even when using the absolute bare minimum amount of materials (0.1 mm copper conductor), the surface dose increase is not negligible. When surface coils are used in a linac-MR, the magnetic field orientation does not seem to influence the surface dose increase caused by irradiating through the coil. One method of addressing this problem would be to design the RF coils with open ports through which the patient could be irradiated without obstruction (radiation windows). Another method would be to redesign and build new RF coils out of thin, radio-transparent materials that would minimally impact the surface dose. Using RF coils with radiation windows would cause the treatment planning to be restricted to certain angles and beam sizes, which would not be ideal. Radio-transparent aluminum coils that will cause a minimal surface dose increase are currently being built and tested as part of a separate investigation.

To experimentally investigate the effects of a parallel magnetic field on the surface and buildup dose we used two GMW magnets, placed on top of each other, capable of producing a peak magnetic field of 0.21 T. Polystyrene and Gammex lung phantoms were built, a clinical unit provided 6 MV photons parallel to the magnetic field, and a Markus parallel plate ion chamber was used to measure the depth dose. Measurements were taken with the phantoms placed at two different locations within the magnet. The first setup had the top surface of the phantom coinciding with the top of magnet's bore, while the second setup had the top surface of the phantom coinciding with the center of magnet's bore. The magnetic field of the electromagnet was measured along three orthogonal axes and the measurements were used to validate a calculated 3D magnetic field map. BEAMnrc was used to simulate the clinical linac, and the simulations were benchmarked against the linac's commissioning measurements. Over

93% of all simulated dose profile points passed a 2%, 2 mm γ acceptance criterion, for radiation field sizes ranging from $5 \times 5\ cm^2$ to $40 \times 40\ cm^2$. The magnetic field map was implemented in DOSXYZnrc and the benchmarked phase space file obtained from BEAMnrc was used as the source. Simulations were run in polystyrene and lung with and without the magnetic field, and the results were compared to the measurements.

When the top surface of the phantom coincided with the top of the magnet's bore, the surface dose with a magnetic field was measured to be 10% (of D_{max} measured without magnetic field) for polystyrene, and 11% for lung higher than without a magnetic field. This dose increase is partly due to the presence of the strong magnetic field that is mostly parallel to the radiation beam's central axis. This parallel magnetic field will confine the lateral spread of the contaminant electrons produced in the linac head and in the irradiated air column. The second phenomenon contributing to the surface dose increase is the convergence of the magnetic field lines towards the center of the electromagnet's bore in our particular setup. Thus, not only are contaminant electrons confined by the magnetic field, but they are also concentrated towards the centre of the magnet's bore which was aligned with the center of the beam and the ion chamber. This is further evidenced by the surface dose increasing by 30% for polystyrene and by 32% for lung, compared to the no magnetic field case, when the phantom was placed with its top surface coinciding with the centre of the electromagnet bore. The additional surface and buildup dose increase is caused by the extra ~13 cm of irradiated air column in relatively high (> 0.13 T) magnetic field, and by the magnetic field concentrating more contaminant electrons towards the sensitive volume of the ion chamber. Only the first couple of millimetres in polystyrene, and the first centimetre in lung were affected by the magnetic field when the phantom surface was placed coinciding with the top of the electromagnet bore. However, for the second setup, the whole buildup region was

affected in both polystyrene and lung, with the depth of maximum dose becoming slightly shallower in lung when the magnetic field was turned on.

The EGSnrc depth dose simulations in polystyrene required the air cavity and entrance window of the parallel plate ion chamber to be modeled at each depth to be able to accurately simulate the dose in the buildup region. The DOSXYZnrc code had to be modified to read in the 3D magnetic field map. Also the parameter responsible for restricting the amount of deflection a particle is allowed to undergo over the course of a step due to a magnetic field (EMULMT) was changed from the default value of 0.02 to 0.001. Although this parameter change caused the code to run slower, it resulted in a closer match between the measured and simulated depth dose data, particularly at the surface. With these EGSnrc code adjustments, the Monte Carlo simulated points were within 1% (with respect to no magnetic field D_{max}) of the measurements in polystyrene for both phantom setups.

The body of the Markus ion chamber was acrylic which is substantially different from lung in terms of electron density. Thus, for the lung Monte Carlo simulations the acrylic body of the ion chamber also had to be simulated in addition to the air cavity and entrance window. Using the same EGSnrc modifications that were used for polystyrene, most (>95%) of the simulated depth dose points were within 1.5% (with respect to no magnetic field D_{max}) of the measurements in the Gammex lung phantom.

Implementation of any 3D magnetic field map in EGSnrc is relatively simple, and adjustment of parameters to more accurately decouple the effects of $\vec{F}_{ret}$, $\vec{F}_{ms}$, and $\vec{F}_{em}$ is easily accesible. In conclusion, EGSnrc is able to accurately calculate depth doses in the presence of a magnetic field, with these adjustments, in both polystyrene and lung. Investigating the accuracy

of the EGSnrc simulated doses with a magnetic field can be further extended to other materials/tissue types, such as bone, fat, etc. Also the code is still to be further experimentally verified at interfaces between substantially different tissue types: lung/bone, soft-tissue/lung, soft tissue/bone, etc.

Chapter 7: Bibliography

1. Canadian Cancer Society, “Cancer Information,” http://www.cancer.ca (2018).
2. Vital statistics: Death database, CANSIM Table 102-0561, http://www5.statcan.gc.ca/cansim/a05?lang=eng&id=1020561#F11 (n.d.).
3. Canadian Cancer Society’s Advisory Committee on Cancer Statistics. Canadian Cancer Statistics 2017 (Toronto, ON: Canadian Cancer Society, 2017).
4. R. Siegel, C. Desantis, K. Virgo, K. Stein, A. Mariotto, T. Smith, D. Cooper, T. Gansler, C. Lerro, S. Fedewa, C. Lin, C. Leach, R.S. Cannady, H. Cho, S. Scoppa, M. Hachey, R. Kirch, A. Jemal, and E. Ward, “Cancer Treatment and Survivorship Statistics , 2012,” CA. Cancer J. Clin. 62, 220–241 (2012).
5. O. Glasser, Wilhelm Conrad Rontgen and the early history of Roentgen Rays (Charles C Thomas, Springfield, Illinois, 1934).
6. J. Bernier, E.J. Hall, and A. Giaccia, “Radiation oncology: A century of achievements,” Nat. Rev. Cancer 4(9), 737–747 (2004).
7. C.A. Perez, L.W. Brady, and J.L. Roti, Principles and Practice of Radiation Oncology, 3rd ed. (Lippincott-Raven, Philadelphia, PA, 1998).
8. S.F. Kry, S. a. Smith, R. Weathers, and M. Stovall, “Skin dose during radiotherapy: A summary and general estimation technique,” J. Appl. Clin. Med. Phys. 13(3), 20–34 (2012).
9. A.J. Olch, L. Gerig, H. Li, I. Mihaylov, and A. Morgan, “Dosimetric effects caused by couch tops and immobilization devices: Report of AAPM Task Group 176,” Med. Phys. 41(6), 1–30 (2014).
10. J. Van Dyk, The Modern Technology of Radiation Oncology (Medical Physics

Publishing, Madison, Wisconsin, 1999).

11. G. Failla, “An Objective Method for the Administration of X-Rays,” Acta radiol. 4, 85–128 (1925).

12. International Commission on Radiation Units and Measurements, ICRU Report 50: Prescribing, Recording, and Reporting Photon Beam Therapy (Bethesda, Maryland, 1993).

13. L.A. Dawson and D.A. Jaffray, “Advances in image-guided radiation therapy,” J. Clin. Oncol. 25(8), 938–946 (2007).

14. J.D. Bourland (ed.), Image-Guided Radiation Therapy (Taylor & Francis Group, Boca Raton, FL, 2012).

15. D. Verellen, M. De Ridder, N. Linthout, K. Tournel, G. Soete, and G. Storme, “Innovations in image-guided radiotherapy,” Nat. Rev. Cancer 7(12), 949–960 (2007).

16. G.X. Ding and P. Munro, “Radiation exposure to patients from image guidance procedures and techniques to reduce the imaging dose,” Radiother. Oncol. 108(1), 91–98 (2013).

17. Y. Li, T. Netherton, P.L. Nitsch, P.A. Balter, S. Gao, A.H. Klopp, and L.E. Court, “Normal tissue doses from MV image-guided radiation therapy (IGRT) using orthogonal MV and MV-CBCT,” J. Appl. Clin. Med. Phys. 19(3), 52–57 (2018).

18. L.A. Dawson and M.B. Sharpe, “Image-guided radiotherapy: rationale, benefits, and limitations,” Lancet Oncol. 7(10), 848–858 (2006).

19. H. Shirato, S. Shimizu, K. Kitamura, T. Nishioka, K. Kagei, S. Hashimoto, H. Aoyama, T. Kunieda, N. Shinohara, H. Dosaka-Akita, and K. Miyasaka, “Four-dimensional treatment planning and fluoroscopic real-time tumor tracking radiotherapy for moving

tumor," Int. J. Radiat. Oncol. Biol. Phys. 48(2), 435–442 (2000).

20. J. Pouliot, A. Bani-Hashemi, Josephine Chen, M. Svatos, F. Ghelmansarai, M. Mitschke, M. Aubin, P. Xia, O. Morin, K. Bucci, M. Roach, P. Hernandez, Z. Zheng, D. Hristov, and L. Verhey, "Low-dose megavoltage cone-beam CT for radiation therapy," Int. J. Radiat. Oncol. Biol. Phys. 61(2), 552–560 (2005).

21. B.A. Groh, J.H. Siewerdsen, D.G. Drake, J.W. Wong, and D.A. Jaffray, "A performance comparison of flat-panel imager-based MV and kV cone-beam CT," Med. Phys. 29(6), 967–975 (2002).

22. E.K. Hansen, D.A. Larson, M. Aubin, J. Chen, M. Descovich, A.M. Gillis, O. Morin, P. Xia, and J. Pouliot, "Image-guided radiotherapy using megavoltage cone-beam computed tomography for treatment of paraspinous tumors in the presence of orthopedic hardware," Int. J. Radiat. Oncol. Biol. Phys. 66(2), 323–326 (2006).

23. D. Ionascu, S.B. Jiang, S. Nishioka, H. Shirato, and R.I. Berbeco, "Internal-external correlation investigations of respiratory induced motion of lung tumors," Med. Phys. 34(10), 3893–3903 (2007).

24. E.M. Haacke, R.W. Brown, M.R. Thompson, and R. Venkatesan, Magnetic Resonance Imaging Physicsl Principles and Sequence Design (Wiley-Liss John Wiley & Sons, Inc., New York, 1999).

25. P. Metcalfe, G.P. Liney, L. Holloway, A. Walker, M. Barton, G.P. Delaney, S. Vinod, and W. Tomé, "The Potential for an Enhanced Role for MRI in Radiation-Therapy Treatment Planning," Technol. Cancer Res. Treat. 12(5), 429–446 (2013).

26. B.G. Fallone, B. Murray, S. Rathee, T. Stanescu, S. Steciw, S. Vidakovic, E. Blosser, and D. Tymofichuk, "First MR images obtained during megavoltage photon irradiation from

a prototype integrated linac-MR system," Med. Phys. 36(6), 2084–2088 (2009).

27. B.W. Raaymakers, J.J.W. Lagendijk, J. Overweg, J.G.M. Kok, A.J.E. Raaijmakers, E.M. Kerkhof, R.W. van der Put, I. Meijsing, S.P.M. Crijns, F. Benedosso, M. van Vulpen, C.H.W. de Graaff, J. Allen, and K.J. Brown, "Integrating a 1.5 T MRI scanner with a 6 MV accelerator: proof of concept.," Phys. Med. Biol. 54(12), N229–N237 (2009).

28. J.F. Dempsey, D. Benoit, J.R. Fitzsimmons, A. Haghighat, J.G. Li, D. a. Low, S. Mutic, J.R. Palta, H.E. Romeijn, and G.E. Sjoden, "A Device for Realtime 3D Image-Guided IMRT," Int. J. Radiat. Oncol. 63(2), S202 (2005).

29. M. Lamey, J. Yun, B. Burke, S. Rathee, and B.G. Fallone, "Radio frequency noise from an MLC: A feasibility study of the use of an MLC for linac-MR systems," Phys. Med. Biol. 55(4), 981–994 (2010).

30. M. Lamey, B. Burke, E. Blosser, S. Rathee, N. De Zanche, and B.G. Fallone, "Radio frequency shielding for a linac-MRI system," Phys. Med. Biol. 55(4), 995–1006 (2010).

31. B. Burke, B.G. Fallone, and S. Rathee, "Radiation induced currents in MRI RF coils: Application to linac/MRI integration," Phys. Med. Biol. 55(3), 735–746 (2010).

32. B. Burke, A. Ghila, B.G. Fallone, and S. Rathee, "Radiation induced current in the RF coils of integrated linac-MR systems: The effect of buildup and magnetic field," Med. Phys. 39(8), 5004–5014 (2012).

33. E. Yip, J. Yun, K. Wachowicz, A. Heikal, Z. Gabos, S. Rathee, and B.G. Fallone, "Prior data assisted compressed sensing: A novel MR imaging strategy for real time tracking of lung tumours," Med. Phys. 41(8), 1–12 (2014).

34. J. Yun, E. Yip, Z. Gabos, K. Wachowicz, S. Rathee, and B.G. Fallone, "Neural-network based autocontouring algorithm for intrafractional lung-tumor tracking using Linac-MR,"

Med. Phys. 42(5), 2296–2310 (2015).

35. B. Dietz, E. Yip, J. Yun, B.G. Fallone, and K. Wachowicz, “Real-time dynamic MR image reconstruction using compressed sensing and principal component analysis (CS-PCA): Demonstration in lung tumor tracking,” Med. Phys. 44(8), 3978–3989 (2017).

36. A.J. Olch, L. Gerig, H. Li, I. Mihaylov, and A. Morgan, “Dosimetric effects caused by couch tops and immobilization devices: Report of AAPM Task Group 176,” Med. Phys. 41(6), 1–30 (2014).

37. A.J.E. Raaijmakers, B.W. Raaymakers, and J.J.W. Lagendijk, “Integrating a MRI scanner with a 6 MV radiotherapy accelerator: dose increase at tissue-air interfaces in a lateral magnetic field due to returning electrons.,” Phys. Med. Biol. 50(7), 1363–1376 (2005).

38. A. Keyvanloo, B. Burke, J.S. Aubin, D. Baillie, K. Wachowicz, B. Warkentin, S. Steciw, and B.G. Fallone, “Minimal skin dose increase in longitudinal rotating biplanar linac-MR systems : examination of radiation energy and flattening filter design,” Phys. Med. Biol. 61, 3527–3539 (2016).

39. A.J.E. Raaijmakers, B.W. Raaymakers, and J.J.W. Lagendijk, “Magnetic-field-induced dose effects in MR-guided radiotherapy systems: dependence on the magnetic field strength,” Phys. Med. Biol. 53(4), 909–923 (2008).

40. B.W. Raaymakers, A.J.E. Raaijmakers, A.N.J. Kotte, D. Jette, and J.J.W. Lagendijk, “Integrating a MRI scanner with a 6 MV radiotherapy accelerator: dose deposition in a transverse magnetic field,” Phys. Med. Biol. 49, 4109–4118 (2004).

41. A J E Raaijmakers, B Hardemark, B W Raaymakers, C P J Raaijmakers and J J W Lagendijk, “Dose optimization for the MRI-accelerator: IMRT in the presence of a magnetic field” Phys. Med. Biol. 52, 7045 – 7054 (2007).

42. B.M. Oborn, P.E. Metcalfe, M.J. Butson, a. B. Rosenfeld, and P.J. Keall, "Electron contamination modeling and skin dose in 6 MV longitudinal field MRIgRT: Impact of the MRI and MRI fringe field," Med. Phys. 39(2), 874–890 (2012).

43. C. Kirkby, B. Murray, S. Rathee, and B.G. Fallone, "Lung dosimetry in a linac-MRI radiotherapy unit with a longitudinal magnetic field," Med. Phys. 37(9), 4722–4732 (2010).

44. B.M. Oborn, S. Kolling, P.E. Metcalfe, S. Crozier, D.W. Litzenberg, and P.J. Keall, "Electron contamination modeling and reduction in a 1 T open bore inline MRI-linac system.," Med. Phys. 41(5), 1–15 (2014).

45. A. Keyvanloo, B. Burke, B. Warkentin, T. Tadic, S. Rathee, C. Kirkby, D.M. Santos, and B.G. Fallone, "Skin dose in longitudinal and transverse linac-MRIs using Monte Carlo and realistic 3D MRI field models," Med. Phys. 39(10), 6509–6521 (2012).

46. B.M. Oborn, P.E. Metcalfe, M.J. Butson, and a B. Rosenfeld, "Monte Carlo characterization of skin doses in 6 MV transverse field MRI-linac systems: effect of field size, surface orientation, magnetic field strength, and exit bolus.," Med. Phys. 37(10), 5208–5217 (2010).

47. A.J.E. Raaijmakers, B.W. Raaymakers, and J.J.W. Lagendijk, "Experimental verification of magnetic field dose effects for the MRI-accelerator.," Phys. Med. Biol. 52(14), 4283–4291 (2007).

48. C. Kirkby, T. Stanescu, S. Rathee, M. Carlone, B. Murray, and B.G. Fallone, "Patient dosimetry for hybrid MRI-radiotherapy systems," Med. Phys. 35(3), 1019–1027 (2008).

49. M. Reynolds, B.G. Fallone, and S. Rathee, "Dose response of selected ion chambers in applied homogeneous transverse and longitudinal magnetic fields," Med. Phys. 40(4), 1–

7 (2013).

50. M. Reynolds, B.G. Fallone, and S. Rathee, “Dose response of selected solid state detectors in applied homogeneous transverse and longitudinal magnetic fields,” Med. Phys. 41(9), 1–12 (2014).

51. V.N. Malkov and D.W.O. Rogers, “Charged particle transport in magnetic fields in EGSnrc,” Med. Phys. 43(7), 4447–4458 (2016).

52. A. Ghila, B.G. Fallone, and S. Rathee, “Influence of standard RF coil materials on surface and buildup dose from a 6 MV photon beam in magnetic field,” Med. Phys. 43(11), 5808–5816 (2016).

53. A. Ghila, S. Steciw, B.G. Fallone, and S. Rathee, “Experimental verification of EGSnrc Monte Carlo calculated depth doses within a realistic parallel magnetic field in a polystyrene phantom,” Med. Phys. 44(9), 4804–4815 (2017).

54. H.E. Johns and J.R. Cunningham, The Physics of Radiology, Fourth Edi (Charles C Thomas, Springfield, Illinois, 1983).

55. F.H. Attix, Introduction to Radiological Physics and Radiation Dosimetry (Wiley-Interscience John Wiley & Sons, New York, 1986).

56. M.J. Berger, J.H. Hubbell, S.M. Seltzer, J. Chang, J.S. Coursey, R. Sukumar, D.S. Zucker, and K. Olsen, https://www.nist.gov/pml/xcom-photon-cross-sections-database, (n.d.).

57. P. Mayles, A. Nahum, and J. Rosenwald, Handbook of Radiotherapy Physics: Theory and Practice (Taylor & Francis Group, New York, 2007).

58. F.M. Khan, The Physics of Radiation Therapy, Second Edi (Williams & Wilkins,

Baltimore, 1994).

59. C.R. Blackwell, B.M. Coursey, K.P. Gall, J.M. Galvin, W.L. Mclaughlin, A.S. Meigooni, and C.G. Soares, “Radiochromic Film Dosimetry: Recommendation of AAPM Radiation Therapy Committe Task Group 55,” Med. Phys. 25(11), 2093–2115 (1998).

60. A. Micke, D.F. Lewis, X. Yu, A. Micke, D.F. Lewis, and X. Yu, “Multichannel film dosimetry with nonuniformity correction,” Med. Phys. 38(5), 2523–2534 (2011).

61. H. Morrison, G. Menon, and R.S. Sloboda, “Radiochromic film calibration for low-energy seed brachytherapy dose measurement,” Med. Phys. 41(7), 1–11 (2014).

62. E.Y. León Marroquin, J.A. Herrera González, M.A. Camacho López, J.E. Villarreal Barajas, and O.A. García-Garduño, “Evaluation of the uncertainty in an EBT3 film dosimetry system utilizing net optical density,” J. Appl. Clin. Med. Phys. 17(5), 466–481 (2016).

63. D.J. Griffiths, Introduction to Electrodynamics, Third Eddi (Prentice-Hall, Upper Saddle River, NJ, 1999).

64. J. Jackson, Classical Electrodynamics, Third Edit (Wiley, New York, 1999).

65. F. James, “Monte Carlo theory and practice,” Rep. Prog. Phys. 43, 1147–1189 (1980).

66. G Comte de Buffon, “Essai d’arithm´etique morale,” Suppl´ement ` a l’Histoire Nat. 4, (1777).

67. M.H. Kalos and P.A. Whitlock, Monte Carlo Methods, Second (Wiley, New York, 2008).

68. F. Salvat, M. Fern, and S. J, PENELOPE , a code system for Monte Carlo simulation of electron and photon transport (2006).

69. R. Morin, Monte Carlo Simulation in the Radiological Sciences (CRC Press Inc., 1988).

70. I. Kawrakow, E. Mainegra-Hing, D.W.O. Rogers, F. Tessier, and B.R.B. Walters, *The EGSnrc Code System : Monte Carlo Simulation of Electron and Photon Transport* (NRC Canada, 2011).

71. T.M. Jenkins, W.R. Nelson, and A. Rindi (eds.), Monte Carlo Transport of Electrons and Photons (Plenum Press, New York, 1988).

72. E.W. Larsen, "A theoretical derivation of the condensed history algorithm," Ann. Nucl. Energy 19(10), 701–714 (1992).

73. A.F. Bielajew, "Electron transport in E and B Fields," in Monte Carlo Transp. Electrons Photons, edited by T.M. Jenkins, W.R. Nelson, A. Rindi, A.E. Nahum and D.W.O. Rogers (Plenum Press, New York, 1989), pp. 421 – 434.

74. H.A. Bethe, "Theory of passage of swift corpuscular rays through matter," Ann. Phys. 397(3), 325–400 (1930).

75. H.A. Bethe, "Braking Formula for Electrons of Relativistic Speed," Zeitschrift fur Phys. 76, 293–299 (1932).

76. F. Bloch, "Bremsvermogen von Atomen mit mehreren Elektronen .," Zeitschrift fur Phys. Phys. 81(5–6), 363–376 (1933).

77. G. Moliére, "Theorie der Streuung schneller geladener Teilchen I. Einzelstreuung am abgeschirmten Coulomb-Feld," Zeitschrift für Naturforsch. A 2(3), 133–145 (1947).

78. G. Moliére, "Theorie der Streuung schneller geladener Teilchen II Mehrfach- und

Vielfachstreuung," Zeitschrift für Naturforsch. A 3(2), 78–97 (1948).

79. A.J.E. Raaijmakers, B.W. Raaymakers, S. Van der Meer, and J.J.W. Lagendijk, "Integrating a MRI scanner with a 6 MV radiotherapy accelerator: impact of the surface orientation on the entrance and exit dose due to the transverse magnetic field," Phys. Med. Biol. **52**(7), 929–939 (2007).

80. B.M. Oborn, P.E. Metcalfe, M.J. Butson, a. B. Rosenfeld, and P.J. Keall, "Electron contamination modeling and skin dose in 6 MV longitudinal field MRIgRT: Impact of the MRI and MRI fringe field," Med. Phys. **39**(2), 874–890 (2012).

81. B. Nilsson and a Brahme, "Absorbed dose from secondary electrons in high energy photon beams.," Phys. Med. Biol. **24**(5), 901–12 (1979).

82. A.J.E. Raaijmakers, B. Hårdemark, B.W. Raaymakers, C.P.J. Raaijmakers, and J.J.W. Lagendijk, "Dose optimization for the MRI-accelerator: IMRT in the presence of a magnetic field.," Phys. Med. Biol. **52**(23), 7045–7054 (2007).

83. D.W. Litzenberg, B. a Fraass, D.L. McShan, T.W. O'Donnell, D. a Roberts, F.D. Becchetti, a F. Bielajew, and J.M. Moran, "An apparatus for applying strong longitudinal magnetic fields to clinical photon and electron beams.," Phys. Med. Biol. **46**(5), N105–N115 (2001).

84. S.J. Hoogcarspel, S.P.M. Crijns, J.J.W. Lagendijk, M. van Vulpen, and B.W. Raaymakers, "The feasibility of using a conventional flexible RF coil for an online MR-guided radiotherapy treatment.," Phys. Med. Biol. **58**(6), 1925–1932 (2013).

85. B.J. Gerbi and F.M. Khan, "Measurement of dose in the buildup region using fixed-

separation plane-parallel ionization chambers," Med. Phys. **17**(1), 17–26 (1990).

86. S.L. Hackett, B. Van Asselen, J.W.H. Wolthaus, J.G.M. Kok, S.J. Woodings, J.J.W. Lagendijk, and B.W. Raaymakers, "Consequences of air around an ionization chamber : Are existing solid phantoms suitable for reference dosimetry on an MR-linac?," Med. Phys. **43**(7), 3961–3968 (2016).

87. Y. Chen, A.F. Bielajew, D.W. Litzenberg, J.M. Moran, and F.D. Becchetti, "Magnetic confinement of electron and photon radiotherapy dose: a Monte Carlo simulation with a nonuniform longitudinal magnetic field.," Med. Phys. **32**(12), 3810–3818 (2005).

76. D.M. Santos, J. St. Aubin, B.G. Fallone, and S. Steciw, "Magnetic shielding investigation for a 6 MV in-line linac within the parallel configuration of a linac-MR system," **39**(February), 788–797 (2012).

77. B.W. Raaymakers, A.J.E. Raaijmakers, A.N.J. Kotte, D. Jette, and J.J.W. Lagendijk, "Integrating a MRI scanner with a 6 MV radiotherapy accelerator: dose deposition in a transverse magnetic field," Phys. Med. Biol. **49**, 4109–4118 (2004).

78. A.J.E. Raaijmakers, B.W. Raaymakers, and J.J.W. Lagendijk, "Magnetic-field-induced dose effects in MR-guided radiotherapy systems: dependence on the magnetic field strength," Phys. Med. Biol. **53**(4), 909–923 (2008).

79. I.J. Chetty, B. Curran, J.E. Cygler, J.J. Demarco, G. Ezzell, B.A. Faddegon, P.J. Keall, H. Liu, C.C. Ma, D.W.O. Rogers, J. Seuntjens, D. Sheikh-, J. V Siebers, and H. Liu, "Report of the AAPM Task Group No . 105 : Issues associated with clinical implementation of Monte Carlo-based photon and electron external beam treatment planning," Med. Phys.

34(12), 4818–4853 (2007).

80. I. Meijsing, B.W. Raaymakers, A.J.E. Raaijmakers, J.G.M. Kok, L. Hogeweg, B. Liu, and J.J.W. Lagendijk, "Dosimetry for the MRI accelerator : the impact of a magnetic field on the response of a Farmer NE2571 ionization chamber," Phys. Med. Biol. **54**, 2993–3002 (2009).

81. D.W.O. Rogers, B. Walters, and I. Kawrakow, *BEAMnrc Users Manual NRCC Report PIRS-0509(A)revL* (Ottawa, 2011).

82. B. Walters, I. Kawrakow, and D.W.O. Rogers, *DOSXYZnrc Users Manual NRCC Report PIRS-794revB* (Ottawa, 2011).

83. D. Sheikh-Bagheri and D.W.O. Rogers, "Sensitivity of megavoltage photon beam Monte Carlo simulations to electron beam and other parameters," Med. Phys. **29**(3), 379–390 (2002).

84. D.A. Low, W.B. Harms, S. Mutic, and J.A. Purdy, "A technique for the quantitative evaluation of dose distributions," Med. Phys. **25**(5), 656–661 (1998).

85. H.W. Koch and J.W. Motz, "Bremsstrahlung Cross-Section Formulas and Related Data," Rev. Mod. Phys. **31**(4), 920–955 (1959).

86. A.F. Bielajew, "The effect of strong longitudinal magnetic fields on dose deposition from electron and photon beams.," Med. Phys. **20**(4), 1171–1179 (1993).

87. D. Sheikh-Bagheri, D.W.O. Rogers, C.K. Ross, and J. Seuntjens, "Comparison of measured and Monte Carlo calculated dose distributions from the NRC linac," Med. Phys. **27**(10), 2256–2266 (2000).